Dissecting neural circuits for vision in non-human primates using fMRI-guided electrophysiology and optogenetics

Thesis by

Shay Ohayon

In Partial Fulfillment of the Requirements for the degree

of

Doctor of Philosophy

CALIFORNIA INSTITUTE OF TECHNOLOGY

Pasadena, California

2014

(Defended 15th May 2014)

This work is dedicated to my parents

The distance between your dreams and reality is called action.

- *Unknown*

Acknowledgements

There are many people without whom this thesis would not exist. First and foremost, I would like to acknowledge my PhD advisor, Doris Tsao, for giving me the opportunity to perform research in her lab and the freedom to pursue my own research ideas. She provided continuous guidance and support throughout the years and trusted me in leading experiments and procedures from day one ("OK, now you drill…" will forever be remembered as the ultimate show of confidence to a young graduate student with zero surgical experience).

Nicole Schweers, our lab manager, for always lending an ear and taking care of my animals as if they were her own children.

I would like to thank Prof. Pietro Perona for a joyful collaboration throughout my years at Caltech.

Many thanks also go to all the past members of the Tsao lab. Winrich Freiwald who was a close collaborator throughout the years and provided many important advices on electrophysiology. Sebastian Moeller, for many fruitful discussions and teaching me how to perform electrical microstimulation and fMRI data analysis. Piercesare Grimaldi, who I owe everything I know about histology and immunohistochemistry.

I was extremely lucky to spend three weeks in Stanford where I was trained in the Karl Deisseroth lab by Ilka Diester, who provided continuing support and help to my ongoing optogenetics experiments.

Last and not least, I would like to thank my wife, who left much behind in order to join me in my adventure of pursuing a PhD.

Abstract

The visual system is a remarkable platform that evolved to solve difficult computational problems such as detection, recognition, and classification of objects. Of great interest is the face-processing network, a sub-system buried deep in the temporal lobe, dedicated for analyzing specific type of objects (faces). In this thesis, I focus on the problem of face detection by the face-processing network. Insights obtained from years of developing computer-vision algorithms to solve this task have suggested that it may be efficiently and effectively solved by detection and integration of local contrast features. Does the brain use a similar strategy? To answer this question, I embark on a journey that takes me through the development and optimization of dedicated tools for targeting and perturbing deep brain structures. Data collected using MR-guided electrophysiology in early face-processing regions was found to have strong selectivity for contrast features, similar to ones used by artificial systems. While individual cells were tuned for only a small subset of features, the population as a whole encoded the full spectrum of features that are predictive to the presence of a face in an image. Together with additional evidence, my results suggest a possible computational mechanism for face detection in early face processing regions. To move from correlation to causation, I focus on adopting an emergent technology for perturbing brain activity using light: optogenetics. While this technique has the potential to overcome problems associated with the de-facto way of brain stimulation (electrical micro-stimulation), many open questions remain about its applicability and effectiveness for perturbing the non-human primate (NHP) brain. In a set of experiments, I use viral vectors to deliver genetically encoded optogenetic constructs to the frontal eye field and face-selective regions in NHP and examine their effects side-by-side with electrical micro-stimulation to assess their effectiveness in perturbing neural activity as well as behavior. Results suggest that cells are robustly and strongly modulated upon light delivery and that such perturbation can modulate and even initiate motor behavior, thus, paving the way for future explorations that may apply these tools to study connectivity and information flow in the face processing network.

Table of Contents

Preface

This thesis covers three seemingly independent topics, yet all are tightly connected. The first chapter addresses the guidance of electrodes to deep brain structures that have been previously identified with fMRI. The second chapter explores the possibility that cells selective for faces in the macaque brain may employ similar algorithms for face detection that have been found effective in computer vision applications. The third chapter explores possibilities of applying optogenetic tools for manipulating behavior in the awake behaving monkey. How are all three topics connected? Our over-reaching goal is to obtain a better understanding of face-processing (and eventually, general object recognition) in the brain. Regions involved in such visual processing are buried deep down in the temporal cortex and can vary in location from one individual to another. Regions involved with face processing can be identified with fMRI and guiding electrodes to such deep structures can be done according to anatomical MRI scans. The first chapter in this thesis, therefore, addresses the associated problems with targeting such deep structures, and describes a set of novel solutions to tackle them. Neural recordings performed in these deep face-selective structures are then described in the second chapter. The third chapter provides information about a newly developed technique (optogenetics) which has a great potential to be applied in face-selective regions to obtain better understanding of connectivity and causality. However, before this technique can be applied, it needs careful testing and characterization to fully understand its strengths and limitations when applied to NHPs. The third chapter addresses some of the basic issues of applying this technology and compares it to the de-facto way of

perturbing behavior with electrical microstimulation. The last piece of the story – the application of optogenetic tools in face-selective regions in the brain – is yet to be completed. The fourth chapter, therefore, discuss future directions and preliminary data on applying optogenetic tools to study connectivity and causality in the face patch system.

Introduction

“May you live in interesting times…”

- *Old Chinese curse*

"*May you live in interesting times"*, says an old Chinese curse. In science, however, this should actually be considered a blessing. It is a very exciting and interesting time to be doing neuroscience research, especially visual neuroscience. So many breakthroughs and technological developments are revolutionizing the field every month, it is difficult just to keep track of them. Enormous efforts by large scale initiatives and institutes are underway to unravel the elementary pieces composing brain circuits and their connectivity. Where does this thesis fit in the grand scheme of things?

My personal interest is the visual system and understanding how it solves difficult problems such as object detection, recognition, and classification. In my thesis, I describe my first baby steps entering into the field of neuroscience by focusing on the first problem (object detection) in a sub-system that specializes in specific type of objects (faces). One of my early realization was that addressing scientific questions requires having the right set of tools for the job. Specifically, tools that allow you to perform reliable, accurate, consistent measurements and perturbations in your circuit of interest. Unfortunately, such tools are not always at your disposal, or require optimizations to custom-tailor them for your own needs. In my case, the ability to carry out experiments critically depended on having tools to reliably and consistently target brain structures that are buried deep in the brain of non-human primates (~30 mm below the cortical surface), and that have been previously localized using fMRI. This engineering problem, as it turned out, has never been adequately addressed. My journey, therefore, takes me first through the development of a custom tailored solution that properly addresses the associated problems of deep brain targeting in NHPs (described in

Chapter 1, and summarized in (Ohayon and Tsao 2012)). The next step in my journey is to apply the technique I developed and to address questions related to face detection. Interestingly, face detection has been investigated by the computer-vision community for many years. Insights obtained from automated systems capable of solving this task under certain condition suggest that the problem may be solved efficiently and effectively by detecting simple contrast features. In Chapter 2, I ask whether the brain may be employing a similar heuristic by studying and characterizing single cell responses to various stimuli containing different contrast features. My results (described in Chapter 2, and summarized in (Ohayon, Freiwald et al. 2012) show that face-selective cells are strongly modulated by local contrast and that the right combination of them can lead to very strong firing rate, while a wrong combination can reduce firing rate to base line activity, suggesting local contrast cues are an important feature extracted from the retinal image and used to drive face-selective cells. Linking these single cell properties to behavior, however, remains challenging since we do not have a way to selectively perturb their activity and move from correlation to causation. The next step in my journey, therefore, leads me to optimize a technique for perturbing brain activity. Optogenetics has emerged as a new technology for perturbing brain activity with capabilities that far exceed the de-facto way of brain perturbation (electrical micro-stimulation). Yet, this technique is still in its infancy and applying it to NHPs requires careful characterization and understanding of its advantageous and limitations. To study how this technique may be applied to NHPs, I take a small detour and apply it in a region called the Frontal Eye Field (FEF). A region that is better suited for studying and monitoring direct effects of stimulation on behavior. My results (described in Chapter 3 and summarized in

(Ohayon, Grimaldi et al. 2013)) provide evidence that optogenetics can be used to modulate both cells and behavior in the awake behaving monkey. However, I also find that it is far less effective in driving motor responses compared to electrical micro-stimulation (a result that requires future investigation and better understanding why electrical micro-stimulation is so effective in driving motor responses). Finally, after gaining some insight and experience in applying the technique in FEF, I come back to the face-patch system and apply optogenetics there to investigate functional connectivity in-vivo. Chapter 4 concludes with preliminary unpublished work describing my attempts to apply optogenetics in the face patch. The reminder of this introductory chapter gives the uninformed reader background about inferotemporal cortex and the sub-system I have been investigating (face-patch system), and about the emerging technology for perturbing brain circuits using light (optogenetics).

Inferotemporal Cortex and Face Processing

The body of literature on inferotemporal (IT) cortex is vast, and has grown considerably and consistently over the years. This short background comes to highlight the main discoveries and breakthroughs. It should give the uninformed reader background about what is known to-date and help him/her to place my own body of work into the larger context of studying IT. Readers who are familiar with IT may jump directly to the sub-section "Face selectivity in IT" for a more focused overview of face processing in IT.

Why IT?

Following the major discoveries by Hubel and Wiesel at the mid and late 60s (Hubel & Wiesel, 1968), researchers wondered where visual information flows after primary visual

cortex (V1). Several lines of evidence suggested that IT is a site where additional visual processing may take place and perhaps even the storage place for long term visual memories. Early work by Mishkin and colleagues suggested (via lesions and fiber degeneration analysis) that IT receives projections from earlier visual areas (Kuypers & Szwarcbart, 1965). Bilateral sectioning in IT were known to produce the Klüver-Bucy syndrome that involved visual discrimination deficits (Charles G. Gross, 1973; Holmes & Gross, 1984). IT was proposed to be the last cortical region in the ventral visual pathway that is purely visual (Mishkin, Ungerleider, & Macko, 1983). Early electrophysiological studies by Gross and colleagues (C G Gross, Rocha-Miranda, & Bender, 1972) demonstrated that IT cells respond to visual, but not auditory stimuli. Gross also noticed the unique selectivity IT cells have: despite a very large receptive fields (RFs, 10 degrees or more) cells are more excited by complex shapes rather than by slits, bars, or spots of lights (standard probes used in V1), regardless of their exact position in the RF. Therefore, converging evidence from anatomical studies, lesion studies and electrophysiology, pointed at IT as being an important stage in the visual pathway that involves object processing.

Overall Structure of IT

IT was initially subdivided based on cytoarchitecture into two large sub-regions: TEO (posterior) and TE (anterior). van Essen and colleagues (Maunsell & van Essen, 1983), who developed notions of hierarchical organization of the cortex proposed a finer sub division which was based on projection patterns observed after anterograde tracer injections. Projection patterns terminating exclusively in layer IV (and originate from supragranular layers I-II) were defined as “feed forward”, while connections terminating in both superficial

and deep layers, but not layer IV were defined as “feedback”. In the seminal work of van-Essen (Felleman & Van Essen, 1991), 32 visual areas were identified, based on connectivity, Nissel stain, topographic (orderly mapping of the visual field, or lack of it) and lesion studies. IT was divided according to those criteria into three sub-regions: PIT (posterior), CIT (central) and AIT (anterior), with hierarchy PIT->CIT->AIT. The posterior/central division was made because PIT still contained some topographic organization (which CIT lacked) and based on laminar organization of projections back to V4. The AIT/CIT division was made because CIT has weaker connections to V4. Further divisions were made along the dorsal and ventral direction (i.e. PITd and PITv). The dorsal/ventral division was mainly based on different projection patterns from V4. In addition, the dorsal part was found to be strongly connected with the amygdala, while the ventral part was found to be strongly connected with hippocampus. Additional retrograde tracer experiments revealed that anterior dorsal TE (AITd) receives strong connection from the upper bank of superior temporal sulcus (STS) while anterior ventral TE (AITv) receives connection from the lower bank and fundus of STS (K S Saleem, Suzuki, Tanaka, & Hashikawa, 2000). It is important to remember that strong feedback connections are present: AIT-> CIT, AIT-> PIT, and even sparsely to V1, V2 and V4 (Suzuki, Saleem, & Tanaka, 2000). Overall, the observed connectivity patterns in IT are still classified in very general vague terms: local (e.g. projecting within TEO), or far (e.g. projecting from TEO to TE) (Ichinohe, Borra, & Rockland, 2012).

Micro-structure in IT

A large effort in the early ‘90s took place to establish micro-organizational principles within IT. Gochin (Gochin, Miller, Gross, & Gerstein, 1991) first reported that neurons recorded on

the same electrode are more likely to share stimulus selectivity and have higher cross-correlation, compared to pairs recorded on two independent electrodes, suggesting nearby cells respond similarly. Tanaka and colleagues continued this line of work (K. Tanaka, Saito, Yoshiro, & Moriya, 1991) and develop ideas about columnar organization in IT (K. Tanaka et al., 1991). Fujita and Tanka (Ichiro Fujita, Tanaka, Ito, & Cheng, 1992) proposed that each column is dedicated to the processing a specific visual feature and that within a column cells are tuned to various aspects of that feature. Tanaka (Keiji Tanaka, 2003) later speculated on the functional nature of columns in TE and proposed that they may encode single features and activity within a column could be used to disregard subtle changes to achieve invariance, or that the different selectivity within a column can be used as a differential amplifier to represent a variety of similar features. The two approaches are thought to work in parallel and help to achieve both generalization (categorization) and identification.

Anatomical studies by Fujita (I. Fujita & Fujita, 1996), demonstrated that cells close to an injection site in TE (and TEO) send projections to multiple locations which terminate in small clusters with diameters of around 500um (roughly the expected size of a column), providing anatomical support to the columnar organization hypothesis. Inter-columnar connectivity was observed at layers II-III and projected to other columns at layers I-III. Similar observations were also made by Saleem (Kadharbatcha S. Saleem, Tanaka, & Rockland, 1993) by injecting anterior tracers to TEO and observing two to five patches (columns) in TE.

Although feature representation via cortical columns in IT was well established, new data in recent years has challenged this view. For example, Tamura (Tamura, Kaneko, & Fujita,

2005) found that only a small fraction (22%) of nearby cell pairs (recorded using a multi-contact probe) have positive signal correlation and Sato (Sato, Uchida, & Tanifuji, 2009) concluded that single cells in a column may have unique properties that are not shared by the column, suggesting only parts of IT have "strong" columnar organization that corresponds to a large clustering of cells with similar properties. Rules governing organization outside such clusters remain unknown.

Imaging methods shed more light on the global structure of IT

Intrinsic optical imaging (differences in oxygenated to deoxygenated hemoglobin caused by oxygen uptake by activated regions) paved the way for simultaneously monitoring large regions of the intact IT. Pioneering work by Wang (K. Tanaka, 1996; G. Wang, Tanifuji, & Tanaka, 1998) and later by Tsunoda (Tsunoda, Yamane, Nishizaki, & Tanifuji, 2001) revealed that a single "critical feature" can activate one to seven discrete locations in TE (hypothesized to be columns). Different critical features evoked overlapping columns, suggesting columns represent different, but related features.

The introduction of functional magnetic resonance imaging (fMRI) allowed for the first time to acquire functional data from the entire brain. Pioneering work in humans by Kanwisher (Kanwisher, McDermott et al. 1997) proposed that dedicated modules exist in the brain to analyze specific domains, such as faces. A view that was received with strong criticism (Haxby et al., 2001) since decoding of presented categories was possible even when regions responding maximally to that category were excluded from analysis, suggesting categorical representations is widely distributed and overlapping.

The hypothesis that a limited number of areas might be specialized for representing specific categories of stimuli, such as faces, was first tested in monkeys using fMRI by Tsao (Tsao, Freiwald, Knutsen, Mandeville, & Tootell, 2003). Tsao found discrete regions in IT that were more activated when monkeys observed faces compared to other objects. Data collected in subsequent studies with improved signal to noise ratio using iron based contrast agents (Leite, Tsao et al. 2002) suggested at least six such regions exist, spread across anterior-posterior in the STS (Moeller, Freiwald et al. 2008).

Are there additional modules in IT that are dedicated for a specific category other than faces? What are the grand organizational principles in IT beyond modules dedicated for face processing? These question were addressed by several studies that attempted not only to localize such regions with fMRI, but also look at neural responses in these regions and outside of them (Bell, Malecek et al. 2011). Kiani and colleagues (Kiani, Esteky et al. 2007) (Kriegeskorte, Mur et al. 2008) found that IT responses are similar across humans and monkeys and form category clusters that may correspond to semantic classes, such as animate and inanimate objects (with additional sub-categories, such as faces, birds, etc.). Yet, subsequent studies failed to reproduce similar result (Popivanov, Jastorff et al. 2012), (Baldassi, Alemi-Neissi et al. 2013)) and suggest a simpler account is just shape similarity rather than semantic smembership. Another interesting theory was recently put forth by Konkle and Oliva, suggesting that real-world size may be another principle by which the cortex is organized (Konkle and Oliva 2012).

Another dedicated module in IT was recently reported by Conway and colleagues (Conway, Moeller et al. 2007; Lafer-Sousa and Conway 2013), which may correspond to regions

previously studied by Komatsu and colleagues (Yasuda, Banno, & Komatsu, 2010) (Banno, Ichinohe, Rockland, & Komatsu, 2011). Conway reported the existence of several discrete regions along the STS (from PITd to AITd) that are strongly activated by colors (equiluminant color vs. achromatic stripes) and may form a color-processing network, similar to the face-processing network. It is tempting to speculate that such dedicated modules might be more involved in processing objects that are uniquely defined by their colors, rather than specific module for analysis of colors, which is already taken place in earlier visual areas.

Face processing in IT

Ideas about face-selective neurons can be traced back to the early '80s. Bruce and colleagues (Bruce, Desimone, & Gross, 1981) were the first to notice the strong stimulus specificity of cells in IT have and presented face stimuli to cells in regions above the superior temporal sulcus (STP). Many of the recent published work on face-processing can be traced ideas initially tested by Perrett (Perrett, Rolls, & Caan, 1982). Perrett first reported a set of cells in fundus of STS that selectively respond to faces. These cells preferred faces over other geometrical shapes, looming stimuli, and hands, and responded equally well to humans or monkeys' faces. Perrett also reported that cells preferred a specific view direction (i.e., frontal and not profiles) and that the response is reduced when only parts of the face are presented. Scrambling the position of these features led to a significant response reduction suggesting relative position of features was encoded despite the large RF. Desimone (Desimone, Albright et al. 1984) was the first to propose a way to reduce a complex stimulus to its "critical features". Desimone also found cells that were tuned for profile faces and also

provided evidence that the boundary of objects may not be the critical feature, as cells failed to respond to a profile face when the boundary was kept, but internal features were scrambled. Rolls and Baylis (E. Rolls & Baylis, 1986) tested the effects of retinal size and contrast and concluded that face-selective cells are invariant to contrast and size. A result that was later contradicted by experiments by Ito (Minami Ito, Fujita, Tamura, & Tanaka, 1994).

Advanced data analysis techniques (e.g., Multi-Dimensional Scaling), introduced by Young and Yamane (Young & Yamane, 1992) were applied to study population responses of face-selective cells in both TE and STP. Their results suggested the population code was sparse (a result that was replicated later by (E. T. Rolls & Tovee, 1995)) and that face-selective cells in TE cluster in a configuration that can be explained by physical metric differences extracted from faces, while face-selective cells in STP cells cluster in a configuration might be related to familiarity or social relevant attributes (A result that has not been replicated, but which led to notion that different face-selective regions may have different role in face processing). This was an important step, since it laid down the foundations that different regions in IT may be processing different aspects of faces. Another interesting study by Sugase (Sugase, Yamane, Ueno, & Kawano, 1999) found using information theory measures, that global information (human face/ monkey face/shape) is conveyed earlier in time compared to fine information (expression / identity) that arrives 50 ms later.

Although many studies reported the existence of face-selective cells, there wasn't an established way to find them (but see (Wang, Tanifuji et al. 1998)), and no clear ideas about

their organization across IT. This changed in 2003, when Tsao (Tsao, Freiwald et al. 2003), found that face-selective regions can be identified with fMRI. Using MR-guided electrophysiology, Tsao and Freiwald (Tsao, Freiwald et al. 2006) sampled a large number of cells in regions that were more activated in fMRI when monkeys observed faces compared to other objects. Remarkably, almost the entire population of recorded cells in these fMRI-identified regions were found to be face-selective, suggesting it was dedicated for face processing. Subsequent study by Moeller (Moeller, Freiwald et al. 2008) identified six face-selective regions (PL, ,ML,MF, AL,AF and AM) across IT. Using combined electrical micro-stimulation and fMRI, Moeller and Tsao proposed that these regions form a tightly connected network (see (Logothetis, Augath et al. 2010) for a later in-depth analysis of the effects of micro-stimulation on BOLD).

The discovery that at least six discrete regions are dedicated for face processing raised questions about the nature of representation in each of these regions. Leopold (Leopold, Bondar et al. 2006) first suggested that identity may be represented using norm-based. He found that firing rate of cells typically increased when caricature version of faces were modified along one or more identity axes. Freiwald and colleagues (Freiwald, Tsao, & Livingstone, 2009) revisited early ideas by Perrett about part selectivity and measured responses to faces decomposed to their individual parts (and combinations of such parts), and to caricature drawings that were parameterized, allowing to modify individual components of the face (e.g., inter ocular distance, hair length, etc.). Freiwald's results clearly demonstrated that cells were tuned for the presence of a specific set of facial parts. Furthermore, cells tuning curves for feature value were ramp-like (e.g., firing rate increased

when interocular distance was increased), giving further support for Leopold's model. This work was important since it challenged the prevailing view that face-selective cells require all facial features to be present (see Tanaka 2003). Additional support for this was recently obtained by Issa and DiCarlo (Issa and DiCarlo 2012) who targeted the most posterior face-selective region (PL) and found that the most critical factor in driving responses was the presence of a single dark eye.

Ideas regarding increased selectivity (for specific individual) and invariance (firing regardless of facial view) have their roots in many computational models and electrophysiology studies ((Poggio and Edelman 1990) (Logothetis, Pauls et al. 1994, Logothetis, Pauls et al. 1995, Logothetis and Sheinberg 1996) (Zoccolan, Kouh et al. 2007) (Rust and Dicarlo 2010, Pagan, Urban et al. 2013) (DiCarlo, Zoccolan et al. 2012)). Eifuku and colleagues (Eifuku, De Souza et al. 2004) first reported differences between two face-selective regions in IT. They found that face-selective regions in the STS (probably MF/ML) spanned a face-space that represented facial views, while more anterior regions (probably AL/AM) spanned a face-space that represented facial identity. With the introduction of the face-patch system, Freiwald and Tsao (Freiwald and Tsao 2010) proposed that two main transformations occur along the anterior-posterior direction: while early face-selective regions are face-view specific (MF,ML), intermediate region has mirror symmetry (AL), and the most anterior region (AM) is fully face-view invariant. At the same time, posterior regions are identity insensitive, and respond to many individuals, while anterior face patches respond only to very few individuals.

Perturbation of IT activity

The majority of our knowledge about IT has largely been obtained through correlational studies: activity of cells was recorded and later correlated to visual stimulus and/or behavior. With a few exceptions, the causal role of IT in object recognition and learning was largely inferred via non-reversible lesion studies ((Gross 1973, Gross 1994) (Buffalo, Ramus et al. 1999)). The few notable exceptions include attempts to cool down IT to reduce activity, injection of pharmacological agents and electrical microstimulation. Horel (Horel, Pytko-Joiner et al. 1987) first reported that cooling various regions of IT results in reduction of performance in a face discrimination task. Wang (Y. Wang, Fujita, & Murayama, 2000) demonstrated that focal Bicuculline injections (GABA receptor antagonist, temporarily reducing activity of inhibitory cells), changed selectivity of TE neurons to only some of the presented stimuli, suggesting GABA (or inhibitory cells) play a critical role in generating stimulus selectivity. Afraz (Afraz, Kiani, & Esteky, 2006) used electrical microstimulation and found that a short pulse lagging 50-150 ms after stimulus presentation can significantly alter performance in a face detection task, and that stimulation is more effective in regions that are face-selective.

Up until 2005, these three techniques (pharmacological, thermal and electrical) were the only reversible methods for manipulating brain activity. The first two methods suffer from poor temporal resolution and cannot be used to assess changes on a trial-by-trial basis. While the third (electrical micro-stimulation) has good temporal control, it lacks proper spatial specificity since electrical currents flow along axons and can lead to activation of other regions through fibers of passage. Therefore, there wasn't a good solution for perturbing

activity with both high spatial and temporal resolution. In 2005, this changed with the introduction of a novel technique: optogenetics (described below).

Optogenetics

The term "optogenetics" was coined in 2006 by Deisseroth (Deisseroth, Feng et al. 2006) and was described as an approach for "genetic targeting of specific neurons or proteins with optical technology for imaging or control of the targets within intact living neural circuits". The exact interpretation was modified several times along the way (Dugue, Akemann et al. 2012), but for our purposes here, we will mainly focus on optogenetics applications for perturbing brain circuits. The field, and number of publications, has grown exponentially since the initial publication of Boyden (Boyden, Zhang et al. 2005). Several review papers summarize many aspects of optogenetics, its history and applications (Yizhar, Fenno et al. 2011), (Lin 2012), (Chow, Han et al. 2012), (Han 2012), (Mattis, Tye et al. 2012), (Boyden 2011). The goal of this introductory chapter is not to survey the latest developments, but rather to give a broad overview of the technology. Applying Optogenetics to NHPs has only been attempted so far in a handful of studies and surprisingly, led to no behavioral changes in most early studies. Hence, one motivation for me to apply this technique was to further investigate why no behavioral changes are observed, despite strong neural modulations. The read is referred to the introduction section of Chapter 3 for more comprehensive discussion on this topic.

Origins

The origins of optogenetics can be traced back to the '70s, where Bacteriorhodopsin was first studied in a single cell organism called *Halobacterium halobium* (Oesterhelt and Stoeckenius 1973), which belongs to a larger family called *haloarchea*. To extract energy and information from light *haloarchea* uses four retinal proteins in their cell membrane: Bacteriorhodopsin (BR), Halorhodopsin (HR) and two sensory rhodopsins (SRI and SRII) (Haupts, Tittor et al. 1999). In its original form, BR converts green light (500-650nm) to electrochemical proton gradient, which is used for ATP production. These proteins are involved in motility and photo-orientation, and also allow to maintain iso-osmolarity (concentrations of specific ions) during cell growth. Both Bacteriorhodopsin and Halorhodopsin became a model for studying membrane proteins in general, and transporters in particular. All retinal proteins fold into seven transmembrane helix topology with short interconnecting loops. Absorption of a photon by BR initiates a catalytic cycle that leads to transport of a proton out of the cell**.** In 2002-2003, Nagel and colleagues (Nagel, Ollig et al. 2002) (Nagel, Szellas et al. 2003) first identified two light sensitive channels in a species of alga called *Chlamydomonas reinhardtii.* They called them Channelrhodopsin (ChR1 and ChR2) to highlight this unusual property. ChR1 is a proton pump, while ChR2 is a-specific ion channel. In 2005, three groups sequentially established ChR2 as a tool for genetically targeted optical remote control of neurons, neural circuits and behavior. Karl Deisseroth's lab demonstrated that ChR2 could be deployed to control mammalian neurons *in vitro*, achieving temporal precision on the order of milliseconds (Boyden, Zhang et al. 2005).

This was a major discovery since all opsins require retinal as the light-sensing co-factor, and it was unclear whether central mammalian nerve cells would contain sufficient retinal levels. Subsequent studies by Hegemann's group (Li, Gutierrez et al. 2005) and Nagel (Nagel, Brauner et al. 2005) also confirmed the ability of ChR2 to control the activity of vertebrate neurons.

Optimizations and expansion of the optogenetic toolbox

The wild-type ChR2 protein has a small single-channel conductance and is optimally excitable at wavelength of ~470 nm. It also has relatively long recovery time, limiting the maximal firing rate that can be induced in neurons to 20–40 Hz. Genetic engineering techniques (point mutations and chimeras) were subsequently applied to improve various aspects. Increase channel conductance was tackled by many groups. Nagel (Nagel, Brauner et al. 2005) was the first to point-mutate ChR2 to create the "H134R" variant that offered firing rates up to ~60 Hz. Many mutations have been published since, including "ChETA" /"E123T" (Gunaydin, Yizhar et al. 2010), "ChIEF" (Lin, Lin et al. 2009), and more recently "Chronos" (Klapoetke, Murata et al. 2014).

Attempts to shift the wave-length was pioneered by Zhang (Zhang, Prigge et al. 2008), leading to developments of red-shifted channelrhodopsin "VChR1" (~545nm). The goal of building red-shifted opsins is to provide tools that could be used to manipulate two independent populations with different wave-lengths, or to allow the simultaneous monitoring and modulations of the same populations using voltage or calcium based fluorescence indicators. More recently, red-shifted variants, such as "C1V1" (Mattis, Tye

et al. 2012) and Chrimson (Klapoetke, Murata et al. 2014), pushing the wavelength peak to ~590 nm, and allowing high currents even at (non-optimal) wavelengths of 660 nm.

Another line of work focused on creating inhibitory actuators. Among the first was halorhodopsin, or "eNpHR" (Gradinaru, Thompson et al. 2008), a inward chloride pump that was capable of completely silencing neurons in-vivo. Similarly, "Arch", a proton-pump that also silenced cells was developed by Chow and Han (Chow, Han et al. 2010).

Expression and Delivery

So far, I have not discussed how foreign opsins are introduced into the brain. In genetically tractable animals, such as mouse, drosophila or C.elegance, various approaches are available: germline trangensis (knock-ins, knock-outs or random insertions of the gene of interest), DNA electroporation and combinatorial expression strategies or intersection methods, such as GAL-UAS or Cre-Lox (see (Urban and Rossier 2012) for a nice overview). In genetic non-tractable animals, such as non-human primates, the most common delivery technique is using viral-vectors. Common virus families include retrovirus, Adeovirus, Adeno-associated virus (AAV), Herpes simplex virus (HSV) and canine adeno virus (CAV). These families differ in their structure (enveloped/non-enveloped), genetic material they carry (RNA, single/double stranded DNA), packaging capacity, speed and duration of expression, random integration of site-specific, type of infected cells, tropism and available titers. The two most commonly used today are LentiVirus and AAVs have been the most successful delivery methods to-date. Lenti, due to its relative high capacity and easy of production (which can be made in-house), and AAVs, due to their high titer and different serotype enabling different expression patterns.

Cell-type specificity can be determined to some extent by virus tropism, but generally, viruses infect very broad range of cells. For a more specific expression various *cis*-regulatory elements are used. For a gene to produce a protein, it requires a promoter – or a short section of DNA in front of the gene that functions to recruit transcription proteins (RNA polymeras). To assist promoters, there are also several regulatory elements called transcription factors (TF). TFs, such as enhancers/suppressors that can be located both proximal or at very distal parts to the gene. Such TFs allow modulation of the level of transcription based on various environmental or developmental factors. Due to the limited packaging capacity of viruses, only a handful of promoters are available to target specific cell types. The commonly used neuron-specific promoters are Synapsin (or hSyn), Thy-1 and CAG. CamKII (Calmodulin-dependent protein kinase II) is a promoter that expresses mainly in excitatory neurons, yet some reports indicate that expression in inhibitory cells are observed, depending on the exact viral delivery method (Lenti/AAV). GFAP (glial fabrillary acidic protein) expresses in glia and astrocytes. Unfortunately, a comprehensive database with details about expression patterns with various promoters and viruses is still missing, although, some positive steps have been made to characterize some constructs and viral delivery parameters affecting expression (Diester, Kaufman et al. 2011) (Lerchner, Corgiat et al. 2014).

Another important aspect of opsin-expression is to make sure it does not affect normal operation of cells (i.e., does not change resting voltage potential or impacts its health). For example, initial expression of some opsins (e.g., eNpHR) was shown to cause aggregates in the cytoplasm due to poor membrane trafficking, leading to abnormal behavior and cell

depth. However, introduction of various trafficking motifs enabled better expression (e.g., developments of eNpHR3.0 (Gradinaru, Zhang et al. 2010)).

Chapter 1: MR-Guided Electrophysiology

Adventure is just bad planning…

Roald Amundsen

Introduction

Neural recordings have been traditionally guided by atlas based stereotactic planning. However, most atlases are based on a single animal (Paxinos, Huang et al. 2000, Saleem 2006, Paxinos and Watson 2007, Saleem and Logothetis 2007), which introduces the problem of inter-subject variability. Furthermore, precise localization and alignment of internal features, such as Bregma and Lambda, on the same plane can be very challenging due to variability in suture appearance. Any deviation from the Bregma-Lambda or Ear Bar Zero (EBZ) plane will introduce significant deviations in deep brain targeting. Another associated problem with atlas based targeting is the risk of hitting a blood vessel. Many region of interests (ROIs) are located directly below major blood vessels, ruling out vertical penetration due to the risk of intracerebral hemorrhage.

With the increased availability of functional localizers it is now possible to pinpoint, with exquisite sub-millimeter precision, brain regions representing visual, auditory, somatosensory information or those participating in higher cognitive functions, such as decision making and language (Sereno, Dale et al. 1995, Tootell, Reppas et al. 1995, Tsao, Vanduffel et al. 2003, Kayser, Petkov et al. 2007, Moeller, Freiwald et al. 2008). While fMRI can report activity on a global scale, its temporal and spatial characteristics cannot replace data obtain with electrophysiology, and fMRI activity is only an indirect reflection of underlying activity (Logothetis 2008, Sirotin and Das 2009). Thus, electrophysiological characterization of neural activity in fMRI-identified brain regions is critically needed.

Targeting structures which have been identified in MRI for electrophysiological recording is challenging due to the inherent difference in coordinate systems. While a specific region of interest can be easily and precisely defined in MR space in voxel coordinates, recordings are guided according to stereotactic coordinates. The problem, therefore, is to find a way to register these two systems and to translate a given position and orientation in MR space to a set of parameters that configure the stereotactic arm manipulator to target the intended ROI (Fig. 1).

A traditional solution to the registration problem is to identify in the MR scan a set of features that can be used to determine how the brain would be oriented once the animal is positioned in the stereotactic frame (Paxinos, Huang et al. 2000, Saleem and Logothetis 2007). Physically, stereotactic coordinates are defined by the line passing through the ear canals (AP0) and the horizontal plane passing through the interaural line and the infraorbital ridge. These skeletal features, however, are difficult to localize precisely in anatomical scans: (1) The ear canals are especially vulnerable to magnetic susceptibility artifacts, which can cause spatial mislocalization of the interaural line. (2) The eye orbitals are impossible to see with standard anatomical sequences, leading to use of alignment of the anterior and posterior commissures as an alternate definition of the horizontal plane. Significant mismatch can occur between this definition and the physical definition, leading to a large error during actual stereotactic surgeries.

Here, we propose a novel framework that solves the general registration problem between the MR coordinate frame and the stereotactic frame during the surgical procedure (Fig. 2). The method relies on a machine vision algorithm that finds the optimal transformation between the two coordinate frames by registering a small number of artificial external markers. The framework allows positioning a recording chamber, according to pre-surgery planning, and is not limited to vertical penetrations. Since the registration problem is solved in real time, the stereotactic frame can be physically detached from the animal (ear bars are not inserted to the ear canals). This "floating frame" approach permits implantation of chambers while the animal is simply head fixed in the primate chair, greatly reducing discomfort and complications involved in full stereotactic surgery.

We designed general purpose pre-surgery planning software ("Planner") that can be used with various stereotactic frames and manipulators (available for download from http://www.tsaolab.caltech.edu/) and hence is of usage not only for primate research, but also for smaller animals. The software enables visualization of anatomical and functional scans and allows the user to position virtual chambers, cannulae, grids and electrodes that can assist in precise planning of electrodes' trajectories. The software greatly assists in targeting recording sites by automatically scanning the search space of grid parameters (rotation, tilt angle, hole in grid) and reporting optimal parameters that minimize the distance to a predefined target.

Another novel feature of our software is the ability to automatically identify blood vessels in MR scans and to suggest safe chamber placements and electrode trajectories which avoid passing through them. Such solutions typically require the usage of all degrees of freedom

of the stereotactic manipulator. To obtain the values required to position the stereotactic manipulator in such a way we model the stereotactic manipulator as a robotic arm and use an inverse kinematic algorithm to recover the exact parameters needed (Fig. 2). This approach is generic and the system can solve the problem for any stereotactic manipulator, as long as the user can supply a 3D description of its joints.

We envision that this system will be a valuable tool for electrophysiologists and will facilitate recordings in new brain areas, as well as other types of experiments requiring precise stereotactic targeting, e.g., injection of viral vectors or pharmacological compounds to MR-defined targets. Here, we provide experimental validation from monkeys and rats, as well as computer simulations that give the expected chamber placement error in terms of positional and angular uncertainties.

Methods

Animals and Surgery

Three male rhesus macaques, weighing 6-8 kg were used in the experiments. Surgical procedures followed standard anesthetic, aseptic, and postoperative treatment protocols. The head-post was implanted in two surgical procedures separated by several weeks recovery time. First, the monkey was anesthetized (Ketamin / Dexdomitor, 8mg/kg / 0.02mg/kg), then intubated and switched to a maintenance regime of oxygen (1L/min), and isoflurane (0.5-3 %). The monkey's head was positioned in a stereotaxic frame, and the skull was exposed and cleaned (peroxide 30% and saline). After drilling and thread cutting, ceramic screws were inserted and covered with several layers of acrylic cement, as was all of the exposed skull area. Anesthesia was ended and the monkey was given a period of six weeks or longer to

recover. In a brief second surgery, an MR-compatible head-post was attached to the initial implant using acrylic cement. Several small holes were drilled in the existing implant and served as external markers (roughly 1-2mm in diameter).

For chamber implantation in the primate chair, the monkey was head fixed by securing the head post to the primate chair. The stereotactic frame was rigidly attached to the chair using a custom designed adapter, and mounted in reverse (see Supplementary Fig 3). Marker positions were read out using the stereotactic manipulator. A light sedation (Dexdormitor, 2mg/kg) was given and a small region of the existing acrylic implant was drilled away. The chamber was then mounted along the stereotactic manipulator pole and secured with fresh acrylic.

The rat experiments were conducted on a euthanized animal. The animal was mounted in a Kopf 900A stereotactic frame and the skull was exposed. Several holes were drilled and nylon screws were inserted. The skull was then covered with acrylic and a small plastic piece with five markers was attached. Animal was then scanned and a virtual cannula position was selected at random. The planning software was used to find the manipulator coordinates and a MR-compatible cannula (C313GT, Plastics1) was implanted and filled with MR-visible contrast agent.

All procedures conformed to local and US National Institutes of Health guidelines, including the *US National Institutes of Health Guide for Care and Use of Laboratory Animals*.

MR Scans

Macaques were scanned in a Siemens 3T Tim Trio. Anatomical scans were acquired with an MPRAGE sequence using the following parameters: TR = 2300 ms, TE = 3.37 ms, FOV = 128, slice thickness: 0.5 mm, in-slice resolution: 0.5mm. Functional scans were acquired with an AC88 gradient insert using EPI sequence with the following parameters: TR = 2000 ms, TE = 16 ms, FOV = 100, slice thickness: 1 mm, in-slice resolution: 1 mm.

Rat anatomical scans were obtained in a Siemens 3T Tim Trio with an AC88 gradient insert using following parameters: TR = 2100 ms, TE = 3.47 ms, TI = 1100 ms, FOV = 60, slice thickness: 0.3 mm, in-slice resolution: 0.23 mm.

Results

Framework overview

External markers

The registration framework assumes that one can position MR-visible external markers that are rigidly attached to the animal skull. Such features can be easily prepared in animals that have an acrylic implant, by drilling several small holes in the existing implant and filling them with MR-visible contrast agent such as gadolinium or Vaseline. For animals with only a head post, it is possible to construct a small rigid body attachment with small capsules containing the contrast agent. Markers should be drilled vertically and not perpendicular to

the skull surface as it is easier to readout their values in the former case. There is no constraint on marker placement and they can be set at random positions above the skull, as long as they provide a good coverage of the entire implant (i.e., not clustered at one corner). The minimal number of markers that is needed is three, but it is generally advised to have more (7-10) to obtain better registration accuracy.

Planning chamber placement

Our pre-surgery planning software allows the user to place a virtual recording chamber in an arbitrary position and orientation (pose) relative to the animal. For a given pose, virtual grids can be inserted to the virtual chamber to guide virtual electrodes into the brain. Various grid designs are available (including tilted grids). For a given grid-hole the user can visualize exactly the expected electrode trajectory and the distance from the desired target site (Fig. 3).

Stereotactic manipulator modeling

The stereotactic arm manipulator is modeled using the Denavit-Hartenberg (DH) representation[11], which is a standard representation used in the robotics field to describe a manipulator composed of multiple joints. The manipulator is considered to be a chain, composed of rigid links connected at their ends by rotating or prismatic joints. Each link is associated with a scalar value that controls how much the link is extended or rotated.

The main difference between standard stereotactic surgeries and the approach we propose is the following. In our scheme, the user first specifies a target in MR coordinates (coordinate system 1). This is then translated to absolute stereotactic coordinates (X, Y, Z, coordinate system 2).

The origin of coordinate system 2 is defined to be on one of the frame rails, just above the mark AP0, and the three axes are defined such that they align with the AP, ML and DV directions.

Finally, these coordinates are translated to parameters that directly control the stereotactic manipulator joints (AP, ML, DV, and any additional rotational angles allowed by the manipulator). In standard stereotactic surgeries the frame is used to position a manipulator arm relative to standard landmarks such as AP0 or Bregma. Thus, parameters controlling the stereotactic manipulator need to be explicitly specified.

To convert parameters of the stereotactic manipulator arm to absolute coordinates (X, Y, Z, coordinate system 2) we use the forward kinematic algorithm adopted from the robotics field. The forward kinematic problem is to find the position and orientation of the manipulator tip (or end-effector) in coordinate frame 2, given parameters controlling the arm. The forward kinematic problem can be easily solved by applying a series of rigid body transformations which are defined by the model describing the manipulator link lengths and relative rotations (see appendix 3 for an example of a stereotactic manipulator model described in a DH representation).

Obtaining marker positions in the two coordinate systems

To solve the registration problem between the MR coordinate system and the stereotactic frame coordinate system, two sets of measurements are collected. The first set of measurements is obtained from the MR scan by clicking on the center of each marker (Fig. 2, step 4). The second set is obtained during the surgical procedure by positioning the manipulator tip at each of the markers and reading out the manipulator arm values. To keep things simple, the manipulator is only moved along the three cardinal directions without any rotation, and only ML, DV, and AP are read out. Those values are then translated to absolute stereotactic coordinates by applying the forward kinematic model.

The procedure of obtaining the stereotactic coordinates can either take place while the animal is anesthetized and connected to the stereotactic frame, or in alternative approach which we call the "floating frame". The floating frame approach is a method for placing a chamber while the animal is in the primate chair. The stereotactic frame is rigidly attached to the chair, but not to the animal (Fig. 2, Step 5, right panel, Supplementary Fig. 3). This allows moving the manipulator and reading out the coordinates of external markers while the animal is head-fixed in the primate chair, thus reducing complications associated with placing the animal in the stereotactic frame and insertion of ear bars to the ear canals.

Solving the registration problem

We denote by $P_i = [x_i, y_i, z_i]$ the coordinates of marker i in MR space and by $P_i' = [x_i', y_i', z_i']$ the coordinates of the same marker in the absolute stereotactic coordinate system. The optimal rigid body transformation T, which maps between P and P', such that $P = TP'$ is obtained by solving the absolute orientation problem[10] (see appendix 1).

Once the mapping between a point in MR space and stereotactic space is found, the planned virtual chamber position and orientation are converted from MR coordinates to absolute stereotactic coordinates. Let us denote by C the 4x4 matrix representing the chamber in MR space. That is, it represents both the position of the tip and its orientation relative to scanned volume origin. The chamber in stereotactic space (C') can easily be found via the inverse transformation: $C' = T^{-1}C$.

The remaining problem is to find the set of manipulator link parameters that aligns the tip both in position and orientation with C'. For that, the inverse kinematic problem is solved iteratively using psedo-inverse of the manipulator Jacobian[15] (see appendix 2). Note that this problem is ill posed. Many solutions exist such that the manipulator tip is aligned with the planned chamber. For example, one can translate the manipulator slightly along the AP direction and apply a counter rotation in the horizontal plane, which would bring the tip exactly to the same place. To circumvent this issue the user can constrain the manipulator by fixing some of its parameters. The software can display the virtual manipulator as well as the animal and the stereotactic frame which greatly assist in visualizing how the arm should be positioned relative to the animal (Fig. 3B).

Experimental validation

To test the proposed framework we have targeted several deep brain structures in three monkeys and one rat. Monkey M1 was implanted with a chamber to target face-selective regions in IT cortex (regions ML and PL (Tsao, Freiwald et al. 2006)). Monkey M2 implanted with a chamber to target place-selective regions in the occipital temporal sulcus and parahippocampal cortex. Monkey M3 was implanted with two chambers to target FEF and ML. For the rat experiment, two random locations were selected for cannula placement.

Quantifying misalignment errors

Misalignments between a planned virtual chamber and the implanted chamber were quantified by scanning the animal after the surgery. For monkeys, chambers were filled with gadolinium and a zero degree grid with several thin tungsten rods placed inside plastic guide tubes was inserted. This allowed clear visualization of the chamber axis (Fig. 3C, small inset). For the rat experiment, the cannula was filled with gadolinium which also allowed clear visualization of the direction (Fig. 4). The second scan was registered to the first scan that was used for planning. A second virtual chamber was then placed and aligned with the actual implanted chamber.

The angular error was quantified as the angle between the implanted chamber axis and the planned chamber axis. The positional error was quantified as the minimal distance between

the two axes since positional errors along the chamber axis do not directly affect the projected region below.

The positional and angular errors are summarized in Table 1. We found that in the majority of procedures performed, the implanted chamber was within 1 mm and 1 deg from the planned position. The largest error was observed in the rat experiment and is attributed either to a mechanical instability of our stereotactic frame (Kopf 900A) or to the low number of markers used in this experiment. Mechanical instability was observed when values were read out from this manipulator; a large deviation was observed (> 1mm) when the arm was repositioned at the same marker.

Error analysis

Many factors determine chamber placement accuracy. The most important ones are the number of artificial markers and the errors in reading out their values, either from the MRI or from the stereotactic manipulator. Other factors that can contribute are errors in 3D modeling of stereotactic manipulator or mechanical instability. Below we describe computer simulations addressing these issues to determine the expected error given uncertainty about the model or read out values.

Marker dependent errors

Errors in determining the exact location of markers in the MR scan or in reading out their values from the stereotactic manipulator will lead to an error in the estimated rigid body transformation (T) between the MR coordinate system and the stereotactic frame coordinate system. Errors in determining marker locations in the MR scan mainly depend on the scanner resolution and on the diameter of drilled markers. These two parameters set a lower bound on how accurately the user can localize the markers in the scan. Our experiments took place

with a scanning resolution of 0.5 mm and an average markers' diameter of 1 mm. Improved resolution and smaller diameter markers may provide better accuracy, but come with the cost of collecting more scans to compensate for the reduced SNR.

Errors in pointing markers location using the stereotactic arm depend on the type of manipulator. In our experiments we used a Kopf 1460 manipulator lacking a digital readout, limiting the accuracy of reading out values to about 0.1 mm.

To test the effects of inaccuracies in reading out markers positions' from the MRI scan we randomly generated markers positions (P) in a volume that approximates a monkey implant (45x45x20 mm) and randomly generated a rigid body transformation (T) to simulate the stereotactic frame placement with respect to those markers. Random Gaussian noise with a standard deviation σ was added to the marker positions $Pn=P+N(0, \sigma)$ to simulate the uncertainty in reading out markers position. Marker position in the second coordinate frame were then computed by $P'=TxP$ (i.e., assuming no errors in readout using the stereotactic manipulator). The registration algorithm was used to recover T from P' and Pn.

Noise levels were varied between [0, 2] mm to simulate different possible scanning resolutions and the number of markers was varied between [3, 10]. 1000 Simulations were run for a given configuration. The positional and angular errors of the simulation are summarized in Fig. 5 a,b. We found the number of artificial markers to critically determine the accuracy of the registration. For example, given a fixed uncertainty of 0.5 mm, the

positional error can be reduced from 1 mm using three markers to about 0.3 mm with 10 markers (Figure 5a).

To simulate a more realistic scenario, we repeated the simulations, but added noise ($\sigma = 0.1$ mm) to *P'* to simulate errors in reading out values with the stereotactic manipulator. Overall, results were very similar (Fig. 5 c,d), indicating accuracies were mainly governed by MRI localization errors.

Marker placement on the implant can also affect accuracy. If markers are packed too closely to each other this can lead to larger errors in estimating the correct rigid body transformation. Simulation with markers that were packed in a smaller region (15x15x10 mm) indicated that the main term that is affected is orientation (Supplementary Fig 1 a, b).

Stereotactic manipulator dependent errors

Another possible source of error is inaccurate Denavit-Hartenberg description of the manipulator. For example, the manipulator arm could have a slight tilt along a certain direction or the user-given constants describing the length of a joint might be inaccurate. We simulated both of these scenarios while varying the number of markers and their placement (Supplementary Fig. 2a,b). Our simulations indicate that angular error in the DH description can lead to both positional and angular errors in chamber placement (Supplementary Fig. 2a), while errors in a joint length can only affect chamber position (Supplementary Fig. 2b). Overall, these analyses stress the importance of having a mechanically stable stereotactic manipulator that is well calibrated.

Correction for surgical placement errors

As described above, small accumulated errors in chamber placement cannot be avoided. The implanted chamber will not align perfectly with the virtual planned chamber due to factors described above. Positional errors less than 1 mm and angular errors less than 1 deg are expected. Errors in chamber placement are also amplified when one is trying to target a deep brain region as a slight angular error will throw the electrode off the desired trajectory. Generally, a target located *d* mm below the chamber and an angular error of α can lead to an expected error of $d \times \sin(\alpha)$ mm to the target. For example, a 1 deg angular error in chamber placement and a target located 50 mm below the chamber would induce an absolute error (closest point between the target and a line passing along the chamber axis) of 0.87 mm.

These errors can be minimized in post-surgery planning by correcting the position/orientation of the virtual chamber to the implanted one. Identification of such errors is possible by filling the chamber with MR contrast agent, placing a zero degree grid and several tungsten rods that serve as markers and can indicate the chamber accurate position and orientation (see Figure 3C. inset). Once properly identified, the optimal trajectory can be recomputed. In practice, this typically results in a shift of one grid hole from the original one.

Blood vessel avoidance

A major concern in targeting deep brain structures for electrophysiology is the presence of blood vessels along the penetration trajectory. Electrodes passing through blood vessels can

lead to lesions or seizures induced by internal hemorrhage. Our approach to reduce this risk is to find safe chamber placements in which electrode trajectories do not pass through blood vessels.

The planning software can automatically identify blood vessels in T1-weighted scans using an image-based blood vessel enhancement filter (Frangi 1998). Manual editing is possible and missed blood vessels can be added if image quality is poor. A typical output of the automatic detection is presented in Fig. 6a. Notice that most major blood vessels have been automatically identified. The software can also display the detected blood vessels in any viewing plane. For example, a coronal view is shown in Fig. 6b and detected blood vessels are highlighted in cyan.

Once the user has selected the desired ROIs to be targeted, the software can cast rays from the target outward and project the blood vessels pattern on the brain outer surface or skull. Consider for example the scenario presented in Fig. 6b, where two ROIs have been identified using fMRI (denoted as red blobs in the two hemispheres). The projected pattern for the left ROI is shown in Fig. 6c and the projected pattern for the right ROI is shown in Fig. 6d. A red region on the surface indicates that a ray has intersected a blood vessel and is therefore is considered an unsafe position for targeting the ROI. In Fig. 6c,d, yellow regions are considered safe (no blood vessel intersection). Notice that the two patterns differ depending on the position of the ROI.

The scenario in Fig. 6 shows exactly how dangerous a vertical penetration can be for targeting the ROI in the left hemisphere since a major blood vessel in the Superior Temporal Sulcus (Fig. 6b, highlighted in cyan) lies directly above the ROI. By considering the projected blood pattern one can easily find a safe region for chamber placement to target this ROI. An example for such safe placement is shown in Fig. 6e. This placement is further verified by displaying slices aligned with this electrode trajectory (Fig. 6f). Notice that the penetration still passes through the Superior Temporal Sulcus, but not through the blood vessel. Notice that this chamber placement is not vertical along the stereotactic coordinate, yet can easily be placed using the framework proposed in this paper.

Discussion

We have presented a robust framework that allows precise MR-guided placement of chambers, electrodes, catheters, and other devices to target brain regions that have been identified in MRI. We accomplish this by registering a set of external markers that are easily identified in the MR scan to a set of measurements obtained during the surgery. Our method goes beyond the traditional approach of placing chambers vertically or tangentially to the surface of the skull, and can be used to position chambers pointing in arbitrary directions. We verified our technique by implanting chambers in monkeys and rats, and have obtained some theoretical bounds on expected accuracy using computer simulations.

There are many advantages to the proposed framework over existing techniques (Van Essen 2002, Jing, Wenchao et al. 2010, Sperka and Ditterich 2011). It is generic and can be used to

target any brain structure with any type of stereotactic manipulator. It uses the existing de-facto platform for performing surgeries and does not require expensive equipment such as real-time camera based tracking or MR-compatible stereotactic frames. It allows more flexibility in the planning stage and greatly assists during the surgery by reporting exactly which parameters to set the manipulator to reach the desired target. The external markers do not require any type of precise calibration and can be drilled into an existing implant or constructed from cheap material and attached to the head post.

Our technique of solving the registration problem makes no assumptions on how the animal is positioned in the stereotactic frame. In fact, if the animal already has a head-post, there is no need for the animal to be physically attached to the stereotactic frame at all. The only requirement is for the stereotactic manipulator arm to be rigidly attached to something relative to the skull. Chamber implantation procedures in our lab took place while the animal was head-fixed in the primate chair, while the frame was rigidly attached to the chair (see Supplementary Fig. 3). This approach greatly reduces complications arising from standard stereotactic surgery.

The proposed planning software automatically identifies blood vessels and assists in finding optimal placement for a chamber to target a desired ROI. The ability to place a chamber along any desired direction can also be used to target multiple different sites from the same chamber. In addition, the software can indicate whether a desired ROI is reachable within the configural space of the stereotactic manipulator.

One drawback of our approach is that it uses the stereotactic device to extract absolute metric information. Stereotactic manipulators are usually designed to infer relative metric information relative to some internal features, such as bregma point. Our method to extract absolute coordinates from the stereotactic frame relies on the ability to have an accurate model describing the manipulator. However, in most cases, such a model is unavailable. The exact lengths of manipulator joints and the exact position of the rotation axes are unknown and need either to be approximated or obtained from the manufacturer. As shown in the error analysis section, inaccuracies in proper description of these parameters can lead to significant errors in the final chamber placement.

Another drawback of the technique is that targeting chambers with arbitrary direction requires precise angular positioning of the manipulator. While most manipulators have a highly precise system for translating the manipulator along the DV, ML and AP dimensions, they typically lack a proper way to have similar precision for rotating the manipulator along those dimensions. In addition, to the best of our knowledge, there are no digital readout for the rotational components of stereotactic manipulators and in most cases, available tick marks are spaced at a resolution of 2 or 5 degrees. We hope future stereotactic manipulators designs will not suffer from this limitation.

Our planning software (*Planner*) is publicly available for research purposes and can be downloaded at http://tsaolab.caltech.edu. The web site contains instruction manuals and

video tutorials on how to install and use the software. We have found our planning software to be an extremely valuable tool assisting MR guided electrophysiology.

Appendices

Appendix 1: Solving the absolute orientation problem

A detailed derivation is available in Horn's original paper [10]. Here, we give a brief summary. Let the set of measurements of features in coordinate system A and B be given by $\tilde{P}_A^i = \begin{bmatrix} \tilde{x}_A^i & \tilde{y}_A^i & \tilde{z}_A^i \end{bmatrix}, \tilde{P}_B^i = \begin{bmatrix} \tilde{x}_B^i & \tilde{y}_B^i & \tilde{z}_B^i \end{bmatrix}$. The goal is to find the best rigid body transformation in least square sense, that is: $\arg\min_{t,R} \sum \left\| \tilde{P}_A^i - [R \mid t] \tilde{P}_B^i \right\|^2$.

The first step is to subtract the center of mass from each point cluster: $P_A^i = \tilde{P}_A^i - \overline{P}_A, P_B^i = \tilde{P}_B^i - \overline{P}_B$. Next, we define the following two algebraic operators which are derived from quaternion theory:

$$[T]_L = \begin{bmatrix} T_1 & -T_2 & -T_3 & -T_4 \\ T_2 & T_1 & T_4 & -T_3 \\ T_3 & -T_4 & T_1 & T_2 \\ T_4 & T_3 & -T_2 & T_1 \end{bmatrix}, [T]_R = \begin{bmatrix} T_1 & -T_2 & -T_3 & -T_4 \\ T_2 & T_1 & -T_4 & T_3 \\ T_3 & T_4 & T_1 & -T_2 \\ T_4 & -T_3 & -T_2 & T_1 \end{bmatrix}.$$

We construct the following symmetric matrix : $M = \sum_{i=1}^{N} \left[0, x_A^i, y_A^i, z_A^i \right]_L^T \left[0, x_B^i, y_B^i, z_B^i \right]_R$, and compute its eigen-vectors. The largest eigen-vector of M, e_4, is used to construct $Q = \left[e_4 \right]_L^T \left[e_4 \right]_R^T$. Finally, the optimal rotation is given by $R = Q_{2:4,2:4}$, and the optimal translation is given by $t = \overline{P}_B - R\overline{P}_A$.

Appendix 2: Solving the inverse kinematics problem using iterative manipulator Jacobian

The forward kinematic model computes the position and orientation of an end effector by applying a series of rigid body transformation defined according to the arm model. The inverse problem is to find the joint parameters that will position the end effector in a desired position and orientation. The forward model is denoted by function $f : q \rightarrow [R,T]$ which takes as input the set of joint parameters q and converts them to the position T (1x3) and rotation R (3x3) of the end effector. The distance between a given configuration and the goal configuration can be defined according to the following metric:

$$\Delta(q_1, q_2) = \left[T_x^1 - T_x^2, T_y^1 - T_y^2, T_z^1 - T_z^2, \frac{1}{2} R_x^1 x R_x^2 + R_y^1 x R_y^2 + R_z^1 x R_z^2 \right],$$

where $[R^1 T^1]$ denotes the current configuration and $[R^2 T^2]$ the goal configuration and $R_x^1 x R_x^2$ represents the cross product between the x-direction of R^1 and the x-direction of R^2.

The iterative procedure can be summarized as follows:

Initialization: set q_1 to zero (or a random initial solution)

Iteration:

$$\Delta e = \Delta(q_i, q_{goal})$$
$$\Delta q = J^{\dagger} \Delta e$$
$$q_{i+1} = q_i + \Delta q$$

Where J is the manipulator Jacobian $J = \frac{\partial \mathbf{e}}{\partial \mathbf{q}}$.

Appendix 3: DH Representation for Kopf 1460 manipulator

We represent the stereotactic frame using Denavit-Hartenberg parameters that allow a minimal representation of the model. Any frame and manipulator can be represented using such representation. Below are the parameters for Kopf 1430 frame with 1460 manipulator mounted on the left rail:

Joint	Alpha (angle about common normal, from old z axis to new z axis)	A/r (length of the common normal)	Theta (angle about previous z, from old x to new x)	D (offset along previous z to the common normal)	Prismatic / Rotatory	offset
#1	$\pi/2$	0	$\pi/2$	0	P	0
#2	$\pi/2$	0	0	C1	R	$\pi/2$
#3	$-\pi/2$	0	0	0	R	0
#4	0	C4	0	0	R	π
#5	$\pi/2$	0	0	0	P	C2
#6	$\pi/2$	0	0	0	P	-C3
#7	0	0	0	0	P	C1+C2
#8	0	0	0	0	R	$\pi/2$

Joint #1 specifies the AP position. Joint #2 represents rotation about DV axis. Joint #3 represents rotation about AP axis. Joint #4 represents the 90 degrees discrete rotation of the manipulator. Joint #5 represents the DV position. Joint #6 represents the ML position. Joint #7 represents the length of the last tool tip. Joint #8 represents the rotation of the tip.

The three constants measured from our manipulator were defined as follows:

C1 = 5.395

C2 = 19-C1;

C3 = 12.27;

C4 = 0.15;

Figures

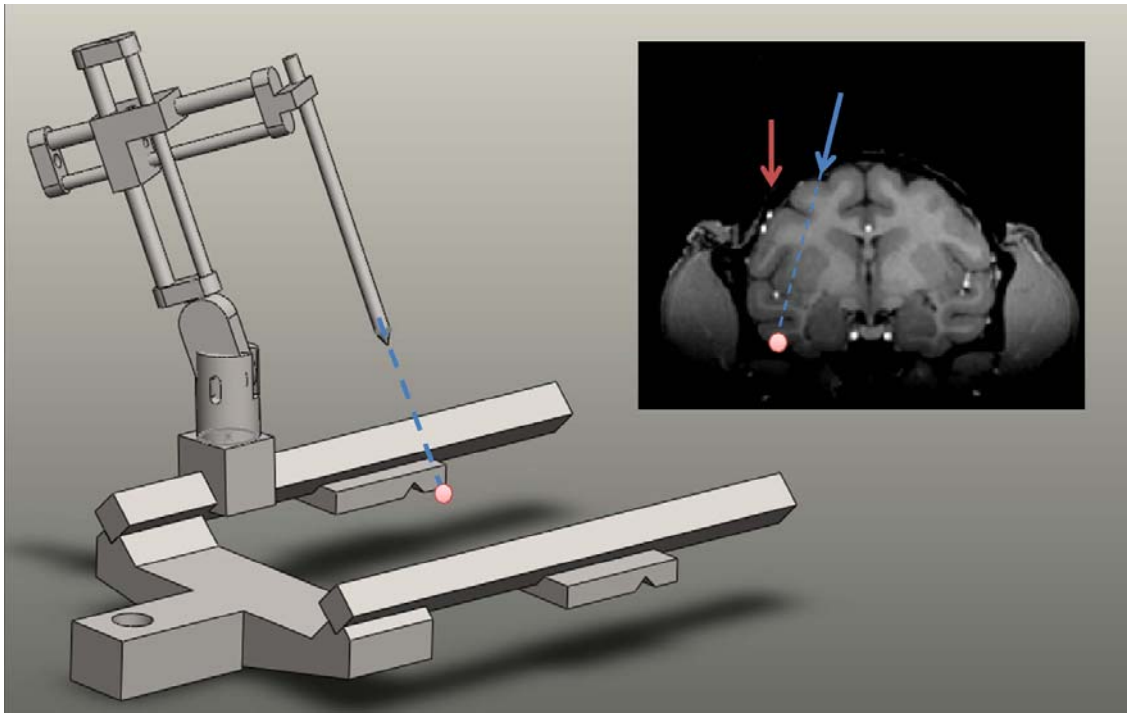

Figure 1: A target in an MR scan (pink dot) is selected according to anatomical or functional considerations. The problem is to position the stereotactic manipulator such that the tip aligns with the desired trajectory. Notice that blood vessels above the target site (small white dots) pose a problem for simple vertical penetration (red line), while a non-vertical trajectory can safely reach the target (blue line).

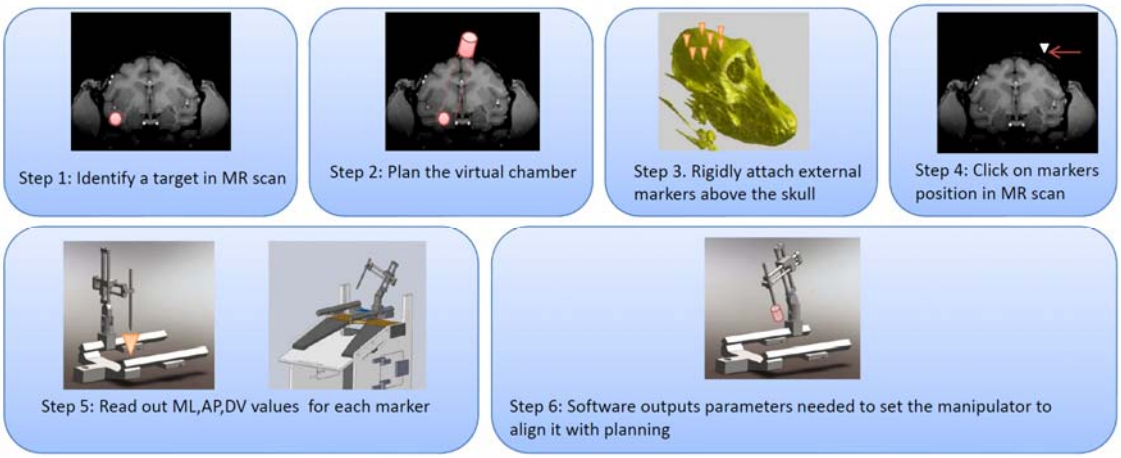

Figure 2: Framework overview. A brain region is selected for targeting and a virtual chamber is placed. Several external markers are rigidly attached to the skull by drilling into an existing implant or securing a small attachment to the head post (not shown). Marker positions in the MR image is identified. During the surgical procedure the position of the markers is read out using the stereotactic manipulator. This can be done even if the stereotactic frame is not physically attached to the animal, but instead to the primate chair. The software solves the targeting problem given the read out values and outputs the set of parameters that are needed to align the manipulator with the planned virtual chamber position.

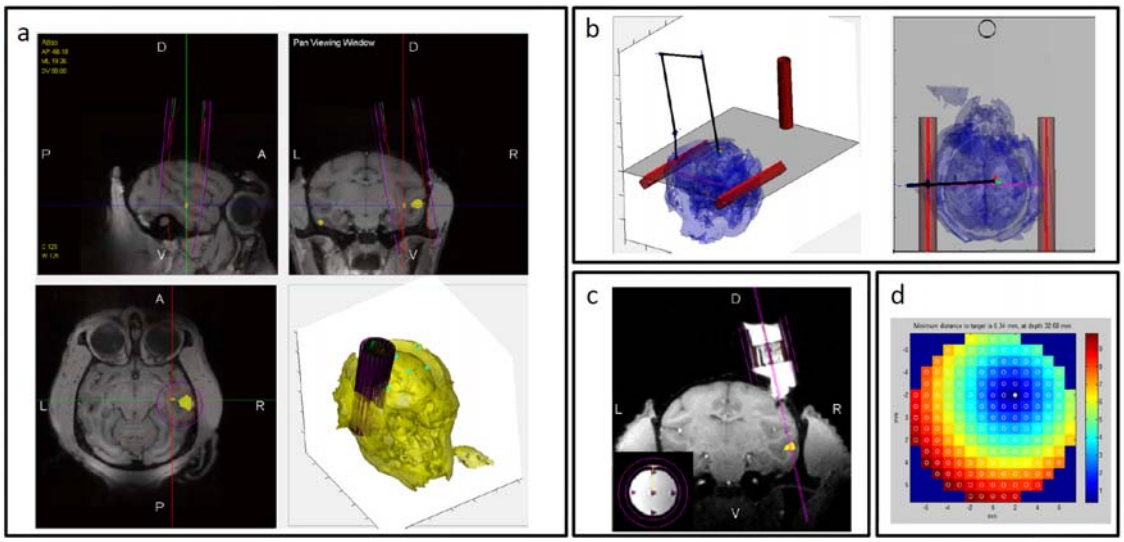

Figure 3: Snapshots from the planning software. (a) Functional activation map (yellow) is overlaid on top of a structural scan. A virtual chamber is placed (magenta). (b) The stereotactic surgical assistant tool displays the position of the virtual manipulator to reach the desired virtual chamber position. The animal position in the frame is found automatically by registering the markers to their imaged positions. (c) Visualization of the implanted chamber (animal M2) and a virtual electrode to target the desired site. Small inset shows precision of virtual electrodes that align perfectly with five tungsten rods used to fine-calibrate grid rotation. (d) Top view of a zero degree grid. White circles indicate grid-hole positions. Color map indicates the distance of each hole to a predefined target in the volume. The software automatically finds the closest hole in the grid to the target and represent it with a filled white circle.

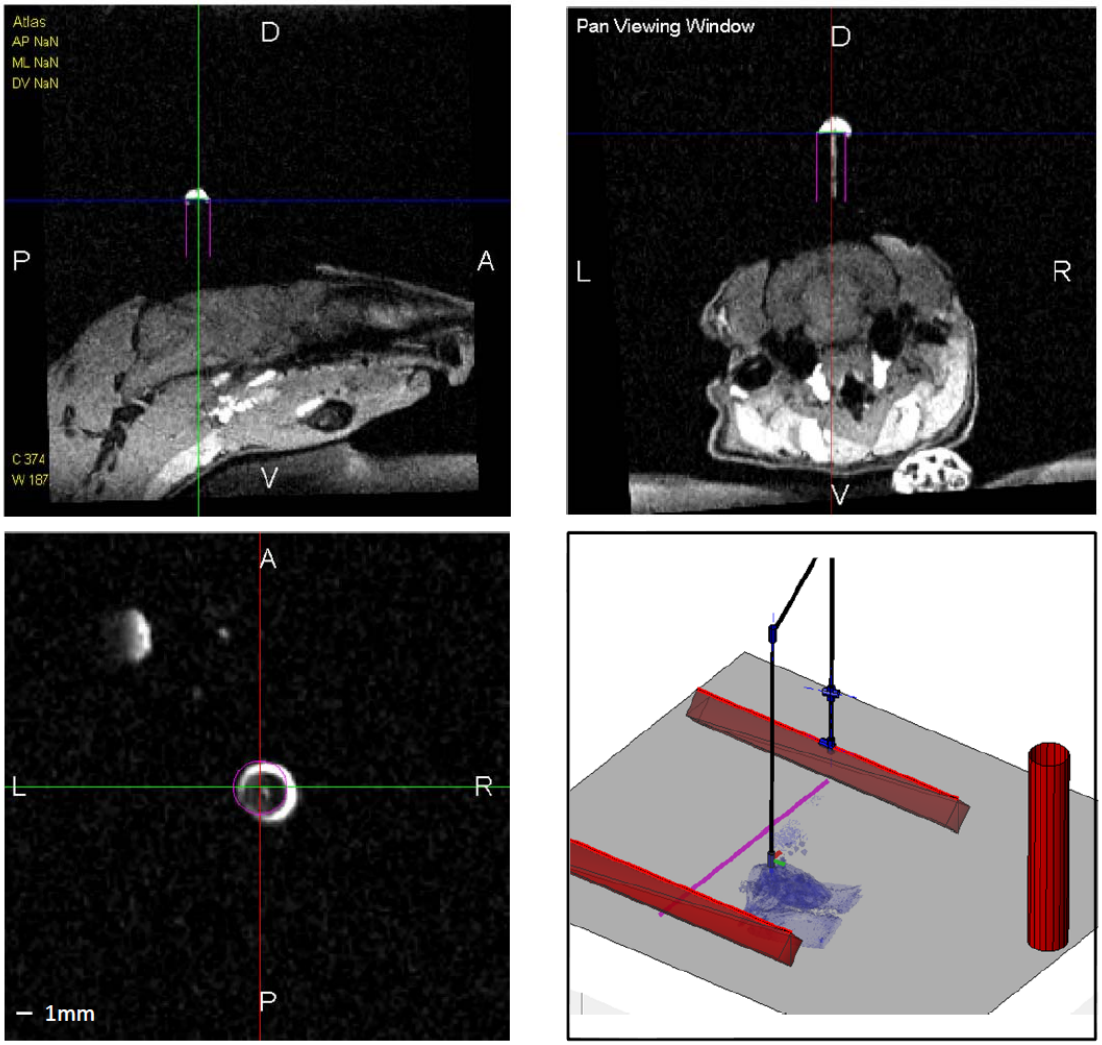

Figure 4:MR-Guidded cannula placement in a rat. Snapshots from the planning software demonstrating the planned cannula position (magenta) and the implanted position (white contrast agent).

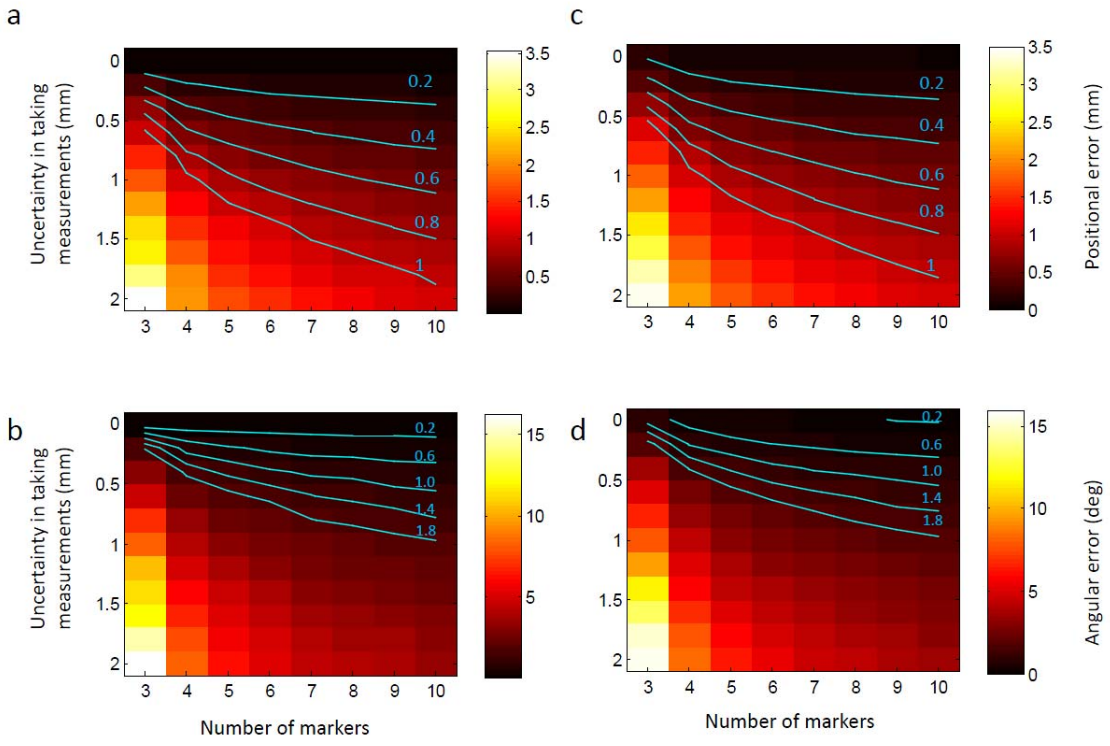

Figure 5. Predicted positional and angular errors of implanting recording chambers**.** (a,b) Predicted positional (a) and angular (b) error as a function of the number of external markers and the uncertainty in annotating markers in the MRI scan. (c,d) Predicted errors when noise is present in both MRI marker positions and read out coordinates from the stereotactic manipulator. Iso-error contours are highlighted in cyan.

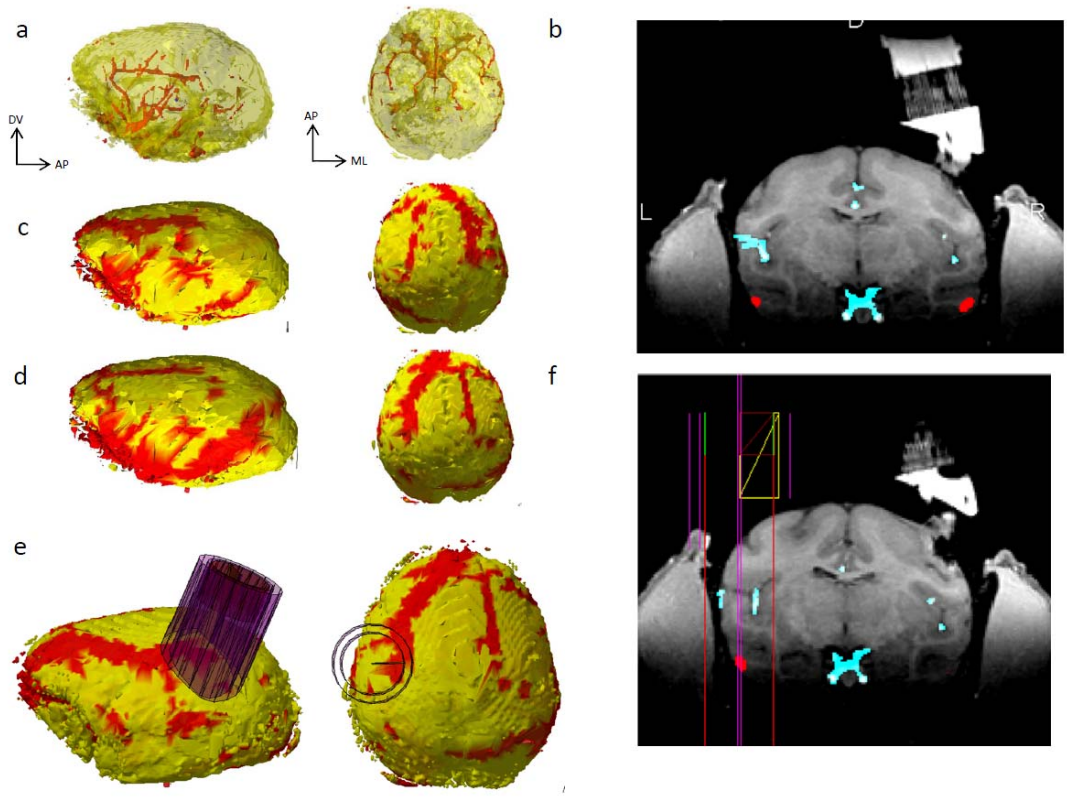

Figure 6. Blood Vessel Avoidance**.** (a) Output of the automatic blood detection algorithm in a T1-weighted scan. (b) Coronal view (AP +16) showing two ROIs selected for targeting (denoted as red blobs) and detected blood vessels (highlighted in cyan). Notice that the slice is aligned to stereotactic coordinates and that a major blood vessel in the Superior Temporal Sulcus is present directly above the ROI in the left hemisphere. (c,d) Projected blood patterns on the brain surface. 3D maps were generated by casting rays from the ROI (left, right) and highlighting in red rays that cross through blood vessels. (e) Safe chamber placement selected for targeting the left ROI. (f) View aligned to chamber coordinates. Notice that the electrode track (highlighted in magenta) hits the ROI, but does not pass through any blood vessels.

Tables

Table 1.

Subject	Number of markers	Positional error (mm)	Angular error (deg)
Monkey M1	7	0.07	1.61
Monkey M2	8	0.7	0.44
Monkey M3 (Chamber 1)	9	0.83	0.89
Monkey M3 (Chamber 2)	9	0.71	0.98
Rat R1 (Cannula 1)	5	0.6	3.31
Rat R1 (Cannula 2)	5	0.25	0.88

Chapter 2: Local contrast features and their importance for face detection

Introduction

Neurons in inferior temporal (IT) cortex of the macaque brain respond selectively to complex shapes (Schwartz, Desimone et al. 1984, Fujita, Tanaka et al. 1992, Logothetis and Sheinberg 1996, Tanaka 1996, Tsunoda, Yamane et al. 2001, Tanaka 2003). Previous studies have proposed that the key element in shape representation is contours and that this representation may be encoded by local curvature and orientation across the population of V4 cells which project to IT (Pasupathy and Connor 2002, Brincat and Connor 2004). However, contours are only one source of information available in the retinal image.

Another rich source of information about object shape is contrast. Humans can detect and recognize objects in extremely degraded images consisting of only a few pixels (Harmon and Julesz 1973, Sinha, Balas et al. 2006, Heinrich and Bach 2010). Thus high frequency information and fine feature details may not be necessary for object detection. What types of features are available in the low frequency range? One possibility is features based on coarse-level contrast cues. Contrast features have been proposed as an intermediate feature representation in computer vision systems (Papageorgiou, Oren et al. 1998) and are ubiquitous in state-of-the art object recognition systems, in particular, for face detection (Viola and Jones 2001, Lienhart and Maydt 2002).

If contrast is an important component of object representation in IT cortex, one would expect cells to be strongly modulated by contrast manipulations such as global contrast reversal. Indeed, when Tanaka et al. (Tanaka, Saito et al. 1991, Ito, Fujita et al. 1994) presented simple geometrical shapes such as stars or ellipses with different protrusions to IT cells and manipulated the contrast by global contrast reversal or outlining (removing contrast from

filled regions and retaining only edges), many cells (> 95%) showed dramatic reductions in firing rate, suggesting that cells in IT carry information about contrast polarity (Fujita, Tanaka et al. 1992, Ito, Fujita et al. 1994, Tanaka 1996, Tanaka 2003). While characterizing cell responses to contrast reversal reveals whether contrast is important, this approach does not address the more fundamental question of how contrast sensitivity might contribute to the form selectivity of a given neuron. Moreover, other studies report that IT cells do not change their firing rates with contrast reversal (Rolls and Baylis 1986, Baylis and Driver 2001), leading to the conclusion that a hallmark of object representation in IT cortex lies in its ability to generalize over global contrast reversal. Thus, the importance of contrast in shape encoding in IT has remained elusive.

Here, we ask whether contrast features serve as a fundamental building block for object selectivity in macaque IT cortex. This question has been difficult to answer in previous studies since cells were picked at random from IT cortex. The variance of cells' shape preferences in such random sampling was large and prohibited a systematic study involving local manipulations of parts and their contrasts. Here, we take advantage of the known shape selectivity in macaque face-selective regions. These regions have a high concentration of cells firing stronger to faces compared to other objects (Tsao, Freiwald et al. 2006). The known shape selectivity enabled us to focus on the individual parts constituting the face and to investigate the role of contrast by systematically manipulating contrast across parts while preserving effective contours.

If contrast plays a role in shape coding we would expect it to have an effect at early stages of face processing. By using functional magnetic resonance imaging (fMRI) with a face

localizer stimulus, we targeted our recordings to the middle face patches. There are several indications that the middle face patches likely represent an early stage of face processing. First, cells in the middle face patches are still view-specific, unlike those in more anterior face-selective regions (Freiwald and Tsao 2010). Second, some cells in the middle face patches still fire to object stimuli sharing rudimentary features with faces, such as apples and clocks (Tsao, Freiwald et al. 2006).

While face-selective cells have been shown to be tuned for fine structural details (Freiwald, Tsao et al. 2009), their selectivity for coarse-level features has not been investigated. Many coarse-level contrast feature combinations are possible. However, only a few can be considered predictive of the presence of a specific object in an image. The predictive features can be found by an exhaustive search (Viola and Jones 2001, Lienhart and Maydt 2002), or by other considerations, such as consistency across presentations with different lighting conditions (i.e., invariance to illumination changes). Indeed, a simple computational model for face detection based on illumination-invariant contrast features was proposed by Sinha (Sinha 2002). In Sinha's model, a face is detected in a given image if 11 conditions are met. Each condition evaluates a local contrast feature (luminance difference across two regions of the face, e.g., nose and left eye) and tests whether contrast polarity is along the direction predicted from illumination invariance considerations. Here, we tested whether face-selective cells are tuned for contrast features useful for face detection. We measured responses to an artificial parameterized stimulus set, as well as to large sets of real face and non-face images with varying contrast characteristics to elucidate the role of contrast in object representation.

Methods

Experimental Procedures

All procedures conformed to local and US National Institutes of Health guidelines, including the US National Institutes of Health Guide for Care and Use of Laboratory Animals.

Face Patch Localization

Two male rhesus macaques were trained to maintain fixation on a small spot for juice reward. Monkeys were scanned in a 3T TIM (Siemens) magnet while passively viewing images on a screen. MION contrast agent was injected to improve signal to noise ratio. Six face selective regions were identified in each hemisphere in both monkeys. Additional details are available in (Tsao, Freiwald et al. 2006, Freiwald and Tsao 2010, Ohayon and Tsao 2012). We targeted middle face patches that are located on the lip of the superior temporal sulcus and in the fundus (Figure S1).

Visual Stimuli and Behavioral Task

Monkeys were head fixed and passively viewed the screen in a dark room. Stimuli were presented on a CRT monitor (DELL P1130). Screen size covered 21.6 x 28.8 visual degrees and stimulus size spanned 7 degrees. The fixation spot size was 0.25 degrees in diameter. Images were presented in random order using custom software. Eye position was monitored using an infrared eye tracking system (ISCAN). Juice reward was delivered every 2-4 seconds if fixation was properly maintained. We presented in rapid succession (5 images / s)

a set of 16 real face images, 80 images of objects from non-face categories (fruits, bodies, gadgets, hands, scrambled images) and 432 images of a parameterized face. Each image was presented 3-5 times to obtain reliable firing rate statistics.

Parameterized face stimuli generation

The parameterized face stimuli were generated by manual segmentation of an average face. Each part was given a unique intensity level ranging between dark (0.91 cd/m^2) and bright (47 cd/m^2). We generated our stimuli using an iterative search algorithm that aimed to cover all possible pair-wise combinations of part intensities with the minimal number of permutations. That is, our data set contained at least one exemplar for every possible part-pair (55), and every possible intensity level (11x11). We used a greedy approach: starting with a single random permutation, we added the next permutation that contained the needed intensity values (if more than one was found, a random decision was made). In this way, we were able to reduce the number of possible combinations from 6655 (55x11x11) to 432. Each condition used for the analysis (intensity in Part A > intensity in Part B) aggregated on average 214 ± 8 stimuli. The stimulus set did not contain an intensity bias toward any of the parts. A 1-way ANOVA revealed that the mean intensity in each part did not significantly deviate from all other parts ($P > 0.5$).

Neural Recording

Tungsten electrodes (18-20 Mohm at 1 kHz, FHC) were back loaded into metal guide tubes. Guide tubes length was set to reach approximately 3-5 mm below the dura surface. The

electrode was advanced slowly with a manual advancer (Narishige Scientific Instrument). Neural signals were amplified and extracellular action potentials were isolated using the box method in an on-line spike sorting system (Plexon). Spikes were sampled at 40 kHz. All spike data was re-sorted with off-line spike sorting clustering algorithms (Plexon). Only well-isolated units were considered for further analysis.

Data analysis

Data analysis was performed using custom scripts written in C and MATLAB (MathWorks). A trial was considered to be the time interval from one stimulus onset to the next (200 ms). We discarded all trials in which the maximal deviation from the fixation spot was larger than 3 degrees. PSTHs were smoothed with a Gaussian kernel ($\sigma = 15\,\text{ms}$). Unless otherwise stated, stimulus response was computed by averaging the interval [50, 250] ms relative to stimulus onset and subtracting the preceding baseline activity, which was estimated in the interval [0, 50] ms.

We estimated cells ability to discriminate face images from non-face images using d'. d' was computed by $d' = \sqrt{2} Z^{-1}\left(AUC\right)$,where *AUC* is the area under the ROC curve and Z^{-1} is the normal inverse cumulative distribution function (AUC was ensured to be above 0.5 to capture units that were inhibited by faces as well). d' is more sensitive than our previously used face selectivity index (FSI) (Tsao, Freiwald et al. 2006), since it takes into account the response variance. Different measures of face selectivity yielded similar numbers of face-selective cells: 267/280 using the Area Under Curve (AUC) measure from signal detection

theory (Figure S2A, AUC > 0.5, permutation test, $p<0.05$), and 298/342 using the Face Selective Index (FSI) measure (Figure S2B, FSI > 0.3). Similar results were obtained when cells were selected according to d', AUC, or FSI.

Unless otherwise stated, population average response was computed by normalizing each cell to the maximal response elicited by any of the probed stimuli.

Polarity consistency index

Given a contrast polarity feature across two parts (A,B), we counted how many cells fired significantly stronger ($P < 10^{-5}$, Mann-Whitney U-test) for the condition A>B vs. the condition A<B, and normalized the number to be between zero and one: $Index = \left| \frac{\#(A>B) - \#(A<B)}{\#(A>B) + \#(A<B)} \right|$. An index of one corresponds to all cells preferring the same polarity direction and an index of zero corresponds to half of the population preferring A>B and the other half preferring A<B.

Determining geometrical feature significance

For each cell and feature dimension we computed time-resolved post-stimulus tuning profiles, (such as the ones shown in Figure 8C) over three feature update cycles (300 ms) and 11 feature values. Profiles were smoothed with a 1D Gaussian (5 ms) along the time axis. To determine significance we used an entropy-related measure called heterogeneity (Freiwald et al., 2009). Heterogeneity is derived from the Shanon-Weaver diversity index and is defined

as $H = 1 - \frac{-\sum_{i=1}^{k} p_i \log(p_i)}{\log(k)}$, where k is the number of bins in the distribution (11 in our case) and p_i is the relative number of entries in each bin. If all p_i values are identical, heterogeneity is 0, and if all values are zero except for one, heterogeneity is 1. Computed heterogeneity values were compared against a distribution of 5,016 surrogate heterogeneity values obtained from shift predictors. Shift predictors were generated by shifting the spike train relative to the stimulus sequence in multiples of the stimulus duration (100 ms). This procedure preserved firing rate modulations by feature updates, but destroyed any systematic relationship between feature values and spiking. From the surrogate heterogeneity distributions, we determined significance using Efron's percentile method; for an actual heterogeneity value to be considered significant, we required it to exceed 99.9% (5,011) of the surrogate values. A feature was considered significant if heterogeneity was above the surrogate value for continuous 15 ms. For additional information please refer to (Freiwald, Tsao et al. 2009).

Results

Face-selective cells respond differently to different contrast combinations

We identified the locations of six face patches in the temporal lobes of three macaque monkeys with fMRI by presenting an independent face localizer stimulus set and contrasting responses to real faces with those to non-face objects (Tsao, Vanduffel et al. 2003, Moeller, Freiwald et al. 2008, Tsao, Moeller et al. 2008). We then targeted the middle face patches

for electrophysiological recordings (Ohayon and Tsao 2012), (see Experimental Procedures, Figure S1); We recorded 342 well-isolated single units (171 in Monkey H, 129 in Monkey R, and 42 in Monkey J) while presenting images in rapid succession (5 images / s). Images were flashed for 100 ms (ON period), and were followed by a gray screen for another 100 ms (OFF period). Monkeys passively viewed the screen and were rewarded with juice every 2-4 s during fixation.

We presented 16 real face images and 80 non-face object images to assess face selectivity (Tsao, Freiwald et al. 2006). We quantified how well each cell discriminated face images from non-face images using the d' measure (see Experimental Procedures) and considered cells to be face selective if d' > 0.5. Under this criterion, 280/342 cells (137 in monkey H and 108 in monkey R and 35 in monkey J), were found to be face selective across the population (Figure 1, see Experimental Procedures). Similar results were obtained with other face selectivity metrics (Figures S2A-S2B).

Motivated by coarse contrast features that are ubiquitously used in state-of-art face detection systems (Figure 2A, (Viola and Jones 2001)), we designed a simple 11 part stimulus (Figure 2B) to assess selectivity for luminance contrasts in the face. In brief, we decomposed the picture of an average face to 11 parts (Figure 2B), and assigned each part a unique intensity value ranging between dark and bright. By selecting different permutations of intensities we could generate different stimuli. We randomly selected 432 permutations to cover all possible pair-wise combinations of parts and intensities (see Experimental Procedures).

We first tested whether cells selective for real face images would respond to our artificial parameterized stimulus. Cells typically showed large variance of response magnitudes to the

different parameterized stimuli. The example cell in Figure 2C fired vigorously for only a subset of the parameterized faces. The subset that was effective drove the cell to levels that were comparable to those to real faces, while other parameterized stimuli were less effective in driving the cell, leading to firing rates that were comparable to those to objects. A similar trend was observed across the population (Figure 2D). Parameterized face stimuli elicited responses ranging between nothing to strong firing (Figure 2D, right column). Thus different luminance combinations can either be effective or ineffective drivers for cells.

To test the extent to which a parameterized face could drive cells we computed the maximal response across all 432 parameterized face stimuli and compared it to the maximal response evoked by a real face (Figure S2C). In about half of the cells (145/280) the maximal evoked response by a parameterized face was stronger than the maximal evoked response by a real face. Furthermore, the minimal evoked response across the 432 parameterized face stimuli was smaller than the maximal evoked response by objects. Thus, middle face patch neurons can be driven by highly simplified stimuli lacking many of the fine structural features of a real face such as texture and fine contours. On average, we found 60±76 parameterized stimuli per cell that elicited firing rates greater than the mean firing rate to real faces, indicating that the observed ratio of maximal responses was not due to a single stimulus. Thus some of the artificial stimuli seem to be good proxies for real faces.

Cells are tuned for contrast polarity features

Cells responded to the parameterized stimulus set with large variability. But are there any rules governing whether a given stimulus elicits a strong response or not? If so, what are these rules, and do they apply to all cells? We hypothesized that relative intensity, i.e.,

contrast, across parts and its polarity are the governing principles underlying the observed responses. To test this hypothesis, we analyzed firing rate as a function of the pair-wise contrast polarity among the 11 face parts. For each cell, we considered all 55 possible part pairs (pair table, Supplementary Table 1). For a given part pair (A-B), we compared the responses to stimuli with intensity of part A greater than part B with responses to the reversed contrast polarity, irrespective of the luminance values assumed by the remaining nine face parts. If contrast polarity plays a role in determining the observed variability, cells should show significant differences in firing rates for the condition A>B vs. the condition A<B.

We found that middle face patch neurons are indeed sensitive to the contrast between face parts and its polarity. This is illustrated by an example cell in Figure 3A (same cell that is shown in Figure 2C), whose firing rate was significantly modulated by 29 of 55 contrast pairs ($P < 10^{-5}$, Mann-Whitney U-test). Not only were these firing rate differences significant, they were also sizeable. For example, the example cell fired about twice as strongly when the intensity in the left eye region was lower than that of the nose region (30 Hz, vs. 15 Hz, Figure 3A), irrespective of all other 9 face parts.

The same pattern of results was observed across the population. Out of the 280 face-selective cells, 138 (62/135 in Monkey H, 57/108 in Monkey R and 19/35 in Monkey J) were significantly tuned for at least one contrast polarity pair ($P < 10^{-5}$, Mann Whitney U-test). Those cells sensitive to contrast polarity features were influenced by 8.13 ± 7.17 features (Figure S3). Different cells were tuned for different contrast polarity features. The tuning for contrast polarity features can be summarized in a tuning matrix indicating for each part-pair whether it was significant, and if so, which polarity evoked the stronger response. The tuning

matrix of monkey R (Figure 3B) illustrates the diversity, but also consistency, of significant tuning in the population. Similar tuning matrices were observed for monkey H (Figure 3C) and monkey J (Figure 3D). Thus, about 50% of face-selective cells encode some aspect of contrast polarity across face parts.

Is there a common principle behind the observed tuning to contrast polarity? Computational models, as well as psychophysics observations (Viola and Jones 2001, Sinha 2002, Sinha, Balas et al. 2006) have suggested that if a certain feature is useful in predicting the presence of an object in an image, its contrast polarity should be consistent across different image presentations, and should generalize over different illumination conditions, and small changes in viewpoint. To test this, we conducted illumination invariance measurements for human and macaque faces (Figures S4A-S4D) and confirmed that a subset of contrast polarity features such as eye-forehead can predict the presence of a face in an image since polarity is consistent and eyes tend to be darker than the forehead in the majority of images tested. Thus, some contrast polarity features can serve as good indicators to the presence of a face under various light configurations.

To test whether middle face patch neurons coded contrast polarity consistently, we plotted the number of cells that significantly preferred A>B along the positive axis and the number of cells that significantly preferred A<B along the negative axis (Figure 4A). Notice that for a proposed part pair, each cell can either vote along the positive direction or along the negative direction (but not both), depending on which direction elicited the higher significant firing rate. The histogram of cells tuned for specific contrast pairs in Figure 4A demonstrates very strong consistency across the population for preferred polarity direction. For example,

while 95 (42 in monkey H, 41 in monkey R, 11 in monkey J) cells preferred the left eye to be darker than the nose (pair index 11), just a single cell was found that preferred the opposite polarity. The same result was found across other pairs: if a contrast polarity direction was preferred by one cell, it was also preferred by almost all other cells that were selective for the contrast of the part combination. We quantified this by measuring the polarity consistency index (see Experimental Procedures). A consistency index of value one indicates that all cells agree on their contrast polarity preference while a consistency index of zero indicates that half of the cells preferred one polarity direction and the other half, the opposite polarity direction. Pooling data from all three monkeys, we found the consistency index to be 0.93±0.15 (discarding features for which less than two tuned cells were found). Furthermore, polarity histograms from each individual monkey show that preferred polarities were highly consistent across the three animals (Figure 4B). Thus face-selective cells are not encoding a random set of contrast polarities across face parts, but instead have a highly consistent preference for polarity depending on the part pair.

Do the preferred contrast polarities agree with predicted features that are useful for face detection? To test this we plotted the polarities proposed by the Sinha model (Sinha 2002) as well as two other predictions from our illumination invariance measurements (Figure 4A). Overall, we found that many of the predicted contrast polarity features were represented across the population. Importantly, almost no cells were found to be tuned to a polarity opposite to the prediction (Figure S4E).

While cells were highly consistent in their contrast polarity preference for any given part pair, they varied widely as to which pairs they were selective for. Some contrast pairs were

more prominently represented than others. The most common contrast pair was Nose > Left Eye, for which almost 70% of the cells were tuned, followed closely by Nose > Right Eye (Figure 4C). Although the most common features involved the eye region, many other regions were represented as well. A graphical representation of the tuning for several random cells is shown in Figure 4D. Green lines represent a significant part pair which does not include the eye region while yellow lines denote pairs including the eye region. Notice that for some of these cells, the significant feature included non-neighboring parts as well (e.g., top right corner, forehead – chin). Cells encoded on average 4.6 features involving eyes (out of a possible 19) and 3.3 features that did do not include the eye region (out of a possible 36). This suggests that cells are encoding a holistic representation which includes multiple face parts, but not necessarily the entire face.

Contrast polarity information arises from low spatial frequencies

The parts constituting the parameterized face stimulus consisted of large regions (Figure 2B), suggesting that selectivity for contrast polarity between these parts is based on low spatial frequency information. However, it is also possible that contrast information was extracted just from the borders between face parts, and could thus be based on high frequency information.

To test to what extent low and high frequency information contribute to the contrast selectivity we conducted two further experiments in which we presented two variants of the parameterized stimulus (Figures S5C and S5E). The first variant retained the contrast relationships from the original experiment, but only along the contours (Figure S5C). The

second variant was a heavily smoothed version of the original parameterized face. If high frequency information is critical, we would expect to see the same modulation for the first, but not the second variant.

We recorded from 18 additional face-selective units in monkey R and presented both the original parameterized face and the first variant. The cells showed similar patterns of tuning for the original parameterized face (Figure S5B), but almost no significant tuning was found for the first variant (Figure S5D). To further validate that high frequency information is not the critical factor, we recorded 34 additional face-selective units in monkey R while presenting the second, heavily smoothed variant of the parameterized face (Figure S5E). In this case, we found similar tuning for contrast polarity as for the original parameterized face stimulus (Figure S5F).

To further evaluate the contribution of contours compared to contrast we generated a third parameterized face stimulus variant in which we varied the luminance level of all parts simultaneously, resulting in 11 different stimuli (Figure 5A). These stimuli lacked the contrast differences across parts, but maintained the same contours that were present in the normal parameterized face stimuli. The third variant stimuli were presented along with the main experiment stimuli (real faces, normal parameterized stimulus and non-face objects) to further characterize the same 280 face-selective units (from the analysis in Figures 2-4). To assess the contribution of contrast, we considered a contrast relationship to be "correct" if its polarity agreed with the Sinha model (Sinha 2002) (see Figure S4E for list of correct part pairs). We found that the stimuli that contained contours, but no contrast relationships elicited a response that was comparable to stimuli with only a few correct features, yet still

significantly higher (almost three fold in magnitude) than the response to non-face objects (Figure 5B).

Thus both contours and correct contrast contribute to the overall firing rate of cells and sensitivity to contrast polarity features arises from low spatial frequency information across large regions of the face.

Contrast is necessary but not sufficient to elicit strong responses

Our results obtained from simplified face stimuli suggest that correct contrast is necessary to yield strong responses from face-selective cells. Do these results extend to real faces? And is correct contrast even sufficient, i.e., does correct contrast, when it occurs outside a face, trigger large responses, too? To investigate these issues we generated an image set using the CBCL library (Heisele, Poggio et al. 2000) containing 207 real faces (registered and normalized in size) and 204 non-face images randomly sampled from natural images lacking faces. Face images lacked external contours such as the hair (Figure 6A).

To determine the number of correct contrast features in each of these images we manually outlined the parts on the average face (Figure 6A). Since all images were registered, the template matched all faces. The same template was then overlaid on each of the non-face images and the number of correct contrast features was computed in a similar way (i.e., by averaging the intensity level in each region, see Figure 6A). In this way we could build an image set of faces and non-faces with varying numbers of correct contrast polarity features (Figure 6B). Although individual samples of 12 correct features in non-face images did not resemble a face, their average did (Figure 6B, last column).

We reasoned that if face-selective cells use a simple averaging scheme over fixed regions similar to proposed computational models (Viola and Jones 2001, Lienhart and Maydt 2002, Sinha 2002), they would respond strongly to non-face stimuli with correct contrast relationships.

We recorded the responses of 25 face-selective units in monkey H and 41 in Monkey R. The response of one cell as a function of the number of correct polarity features is presented in Figure 6C. When presented with pictures of faces, the cell increased its firing rate as the number of correct features increased. However, no significant change in firing rate was observed to non-face images, regardless of the number of correct polarity features (Figure 6D). We found similar behavior across the population (Figure 6E). The number of correct contrast polarity features was found to be a significant factor modulating firing rate for face images (one way ANOVA, $P < 0.0001$), but not for non-face images (one way ANOVA, $P > 0.8$). Thus contrast features, though necessary, are not sufficient to drive face-selective cells. The presence of higher spatial frequency structures can additionally modulate the responses of the cells, and interfere with the effects of coarse contrast structure.

Global contrast inversion

Our results so far demonstrate that contrast can serve as a critical factor in driving face-selective cells. From this finding one would predict that global contrast inversion of the entire image should elicit low firing rates. To test this prediction and directly relate our results to previous studies on effects of global contrast inversion in IT cortex (Rolls and Baylis 1986, Ito, Fujita et al. 1994, Baylis and Driver 2001), we presented global contrast-inverted images of faces and their normal contrast counterparts and recorded from 20 additional face-selective

cells from monkey H and monkey R (Figure 7A, black traces). The response to faces was indeed strongly reduced by global contrast inversion (Figure 7A, $P < 0.01$, t-test). Thus the prediction that global contrast inversion, by flipping all local feature polarities, would induce a low-firing rate for faces was verified. Surprisingly, responses to inverted contrast cropped objects were significantly larger compared to normal contrast cropped objects (Figure 7A, $P < 0.01$, t-test). One possible explanation is that face-selective cells receive inhibition from cells coding non-face objects, and the latter also exploit contrast-sensitive features in generating shape selectivity.

The role of external features in face detection

Behaviorally, it has been found that external features such as hair can boost performance in a face detection task (Torralba and Sinha 2001). Up to now, all the experiments demonstrating the importance of contrast features for generating face-selective responses were performed using stimuli lacking external features (i.e., hair, ears, head outline). We next asked what the effect of global contrast inversion is for faces possessing external features. To our surprise, we found that the population average response to globally contrast-inverted faces possessing external features was almost as high as the average response to normal contrast faces ($P > 0.2$, t-test, Figure 7B). A significant increase in response latency was also observed ($P < 0.001$, t-test); the average latency (time to peak) for normal contrast faces was 106±29 ms, and 160±60 ms for contrast inverted faces. This result suggests that detection of external features provides an additional, contrast-independent mechanism for face detection, which can supplement contrast-sensitive mechanisms. In addition, we again noticed that images of globally contrast-inverted non-face objects elicited slightly higher responses

compared to normal contrast objects ($P < 0.01$, t-test, Figure 7B); this was true for all object categories (hands, bodies, fruits, and gadgets), but not for scrambled patterns ($P > 0.05$, t-test, Figures S6A and S6B).

It seems plausible that the component which elicited the high firing rate in the inverted contrast uncropped faces was hair. To test this, we constructed artificial stimuli which were exactly like the original, but with black hair added (Figure 7C). This allowed us to directly test the effect of adding hair on responses to stimuli with correct and incorrect contrast features (16 images per condition), and observe whether responses to hair can override responses to incorrect internal contrast features. We recorded 35 additional face-selective cells in monkey H; the average population response is shown in Figure 7C. When hair was added to incorrect contrast faces (magenta line), the response was delayed and almost as high as that to correct contrast faces without hair (Figure 7C, green line, $P > 0.3$, t-test, Figure 7D). This shows that a specific external feature, hair, can drive face-selective cells via a longer latency mechanism even when incorrect contrast is present in internal features.

Cell selectivity for the presence of a part depends on its luminance

Why do non-face images containing correct contrast relationships nevertheless elicit no response (Figures 6C-E)? What is the additional element present in a face that is lacking in these non-face images? One simple hypothesis is that the non-face images lack the correct contours, i.e., the presence of the correct face parts. A recent study examined in detail the coding of face parts in the middle face patches, and demonstrated that cells in this region are tuned for both the presence and geometry of different subsets of face parts (Freiwald, Tsao

et al. 2009). This conclusion was derived from two experiments exploiting cartoon faces: (1) Cells were presented with cartoon faces consisting of all possible combinations of seven basic parts (hair, bounding ellipse, irises, eyes, eyebrow, nose and mouth) and their sensitivity to the presence of specific parts was determined, (2) Cells were presented with cartoon faces in which the geometry of face parts was modulated along 19 different dimensions (e.g., iris size, intereye distance), and tuning was measured along each dimension.

To explore in detail the relationship between contrast tuning and selectivity for the presence of face parts within single face cells, we next repeated the experiments of Freiwald et al. in conjunction with our contrast tuning experiments. We hypothesized that tuning for the presence of a part depends not only on purely geometrical factors (i.e., the shape of the part), but also on part luminance or contrast relative to other parts. To test this hypothesis we presented three stimulus variants: (1) a parameterized face stimulus with correct contrast, (2) the same stimulus with fully inverted contrast, and (3) the original cartoon stimuli used in Freiwald et al., 2009 ("cartoon") (Figure 8A); the first two stimuli were derived from the parameterized contrast stimulus introduced in Figure 2, but with eyebrows, irises and hair added to allow direct comparison to the third stimulus. For each variant we presented the decomposition of the face into seven basic parts (2^7 stimuli). Thus, we could directly compare the results of Freiwald et al. 2009 to our current results and test whether selectivity for the presence of specific face parts also depends on the contrast of those parts.

We recorded from 35 additional face-selective cells from monkey H. The responses of an example cell to the decomposition of all three stimuli (normal contrast, inverted contrast,

cartoon) are shown in Figure 8A. We found that responses were similar between cartoon and normal contrast stimuli. Furthermore, we found that the inverted contrast decomposition elicited very different responses compared to the two normal contrast conditions. To determine whether the presence of a part played a significant role in modulating firing rate we performed seven way ANOVA with parts as the factors (similar to the analysis in Freiwald et al. 2009). Cells exhibited different tuning for parts for the three different stimulus variants (Figure 8B, 7-way ANOVA, $p<0.005$). To quantify the degree to which cells show similar tuning we counted the number of parts that were shared across two conditions. We found that cells were more likely to be tuned to the same part in the normal contrast and cartoon compared to inverted contrast and cartoon ($p < 0.001$, sign test). However, if a cell shows tuning for the presence of a part in the cartoon stimuli, this does not necessarily imply that it will also show preference for the same part in the artificial contrast stimuli (e.g., irises were found to be a significant factor for 16 cells in the correct contrast condition and 11 in the cartoon). More importantly, we found very different preferences for presence of a part between the normal and inverted contrast conditions which cannot be explained by different shapes of the parts since they were exactly the same. For example, while irises were found to be a significant factor in 16 cells for the correct contrast condition, only one cell preferred irises in the incorrect contrast. Thus, preference for a specific part depends not only on the part shape (i.e. contour), but also on its luminance level relative to other parts.

Contrast features and geometrical features both modulate face cell tuning

The second major finding reported in Freiwald et al. 2009 was that cells are tuned to the metric shape of subsets of geometrical features, such as face aspect ratio, inter-eye distance, iris size, etc. Such features are thought to be useful for face recognition. Our present results suggest that face-selective cells use coarse-level contrast features to build a representation which might be useful for face detection. Are these two different types of features, contrast features and geometric features, encoded by different cells, or are the same cells modulated by both type of features?

To answer this, we repeated the Freiwald et al. experiment in which cartoon stimuli were simultaneously varied along 19 feature dimensions, and presented in addition our artificial face stimuli which varied in contrast (see Figure 2B). We recorded the responses of 35 face-selective cells (monkey J) and found similar ramp-shape tuning curves for subsets of geometrical feature dimensions as previously reported. The example cell in Figure 8C increased firing rate when aspect ratio dimension was modified, but not when the inter-eye distance changed (Figure S7A). To determine whether cells were significantly tuned for each one of the 19 geometrical feature dimensions we repeated the analysis described in Freiwald et al. 2009 and computed the heterogeneity index (Figure S7B, see Experimental Procedures).

Out of the 35 face-selective cells, 29 were modulated by at least one geometrical feature (Figures 8D and S7C), where the most common feature was aspect ratio (Figure S7D). Cells were also modulated by contrast polarity features (Figure 8D). Out of the 35 cells, 19 were

modulated by at least one contrast polarity feature. Overall, 49% of the cells were modulated by both types of features (Figures 8E and S7E). Thus, tuning to low-spatial frequency coarse contrast features and to high spatial frequency geometrical features can co-occur in face-selective cells, suggesting that some cells encode information relevant for both detection and recognition.

Discussion

One of the most basic questions about face-selective cells in IT cortex is how they derive their striking selectivity for faces. Motivated by computational models for object detection that emphasize the importance of features derived from local contrast (Viola and Jones 2001, Lienhart and Maydt 2002, Sinha, Balas et al. 2006), this study focused on the question whether contrast features are essential for driving face-selective cells. Our main strategy was to probe cells with a parameterized stimulus set allowing manipulation of local luminance in each face part. The results suggest that detection of contrast features is a critical step used by the brain to generate face-selective responses. Four pieces of evidence support this claim. First, different combinations of contrasts could drive cells from no response to responses greater than that to a real face. Second, the polarity preference for individual features was remarkably consistent across the population in three monkeys. Third, the contrast feature preference followed with exquisite precision features that have been found to be predictive of the presence of a face in an image; these features are illumination invariant, agree with human psychophysics (Sinha, Balas et al. 2006), fMRI studies (George, Dolan et al. 1999, Gilad, Meng et al. 2009), and are ubiquitously used in artificial real-time face detection

(Viola and Jones 2001, Lienhart and Maydt 2002). Finally, the tuning to contrast features generalized from our artificial collage of parts to real face images.

Shape selectivity in IT has been proposed to arise from cells representing different feature combinations (Fujita, Tanaka et al. 1992, Tsunoda, Yamane et al. 2001, Tanaka 2003, Brincat and Connor 2004). Elucidating exactly what features drive activity of randomly sampled cells in IT has been difficult due to the large space of shapes one needs to test (Kourtzi and Connor 2011). Clever approaches such as parameterization of shape (Pasupathy and Connor 2002) or genetic optimization (Yamane, Carlson et al. 2008) are needed to make the problem tractable. Here, we took a different approach, focusing on a specific shape domain. The known shape selectivity of cells in face-selective regions in inferotemporal cortex allowed us to carefully test a specific computational model for generation of shape selectivity, the Sinha model (Sinha 2002).

A plethora of computer vision systems have been developed to detect faces in images. We chose to test the Sinha model for the same reasons that Sinha proposed this scheme in the first place: it is motivated directly by psychophysical and physiological studies of the human visual system. Specifically, Sinha's model naturally accounts for (1) the robustness of human face detection to severe image blurring, (2) its sensitivity to contrast inversion, and (3) its holistic properties. The Sinha model provides a simple, concrete distillation of these three properties of human face detection. Thus it is an important model to test physiologically, and our study is the first to test its critical predictions.

Sinha's theory makes three straightforward predictions. First, at least a subset of face cells should respond to grossly simplified face stimuli. We found that 51% of face cells responded

to a highly simplified 11-component stimulus and modulated their firing rate from no response to responses that were greater than that to a real face. Thus the first prediction of Sinha's theory was confirmed. Second, Sinha's theory predicts a subset of contrast polarity features to be useful for face detection. We found, first, that middle face patch cells selective for contrast across parts, were tuned for only a subset of contrasts. Second, all features predicted by Sinha were found to be important and were found with the correct polarity in all cases, and this was highly consistent across cells (Figures 4 and S4E). Thus, our results have a very strong form of consistency with Sinha's theory. A third prediction of Sinha's theory is that face representation is holistic: robust detection is a consequence of confirming the presence of multiple different contrast features. We found that the shapes of the detection templates used by many (though not all) cells indeed depended critically on multiple face parts and were thus holistic in Sinha's sense. Taken together, our results confirm the key aspects of the Sinha model and pose a tight set of restrictions on possible mechanisms for face detection used by the brain.

Despite these correspondences, our results also show that the brain does not implement an exact replica of the Sinha model. First, cells respond in a graded fashion as a function of the number of correct features, yet an all or none dependence is predicted by the model. Second, the simple Sinha model uses only 12 features to detect a face, while the population of middle face patch neurons encodes a larger number of features. Furthermore, these neurons do not respond to non-face images with 12 correct contrast features (Figure 6E), indicating additional mechanisms for detecting the presence of specific parts are in place.

Our results rule out alternative detection schemes. Models that use geometric, feature-based matching (Brunelli and Poggio 1993) can be ruled out as incomplete, since not only the position of, but also the contrast between features matters. The observation that some of our artificial face stimuli elicited responses stronger than that to a real face might also indicate that a fragment based approach (Ullman, Vidal-Naquet et al. 2002) is unlikely since that theory predicts that the maximal observed response should be to a patch of a real face image and not to an artificial uniform luminance patch; in addition, the holistic nature of the contrast templates in the middle face patches (Figure 4D) suggests cells in this region are not coding fragments. However, our results do not rule out the possibility that alternative schemes might provide an accurate description for cells in earlier stages of the face processing system.

Surprisingly, we found the subjective category of "face" to be dissociated from the selectivity of middle face patch neurons. First, Figure 2 shows that a face-like collage of 11 luminance regions in which only the contrast between regions is modulated can drive a face cell from no response to a response greater than that to a real face. All of the stimuli used in this experiment, including the ineffective ones, would be easily recognizable as a face to any primate naïve to the goals of the experiment. Yet, despite the fast speed of stimulus update, face cells did not respond to "wrong contrast" states of the face. Second, in Figure 6 we show that real face images with incorrect contrast relationships elicited a much lower response than those with 12 correct relationships (indeed, on average, even faces with only 4 correct relationships yielded close to no response at all). Perceptually, all of the real face images are easily recognizable as faces. Thus, it seems that the human categorical concept of face is

much less sensitive to contrast than the early detection mechanisms used by the face processing system.

Previous studies have found that global contrast inversion can either abolish responses in IT cells (Tanaka, Saito et al. 1991, Fujita, Tanaka et al. 1992, Ito, Fujita et al. 1994, Tanaka 1996), or have a small effect (Rolls and Baylis 1986, Baylis and Driver 2001). Our experiments shed some light on this apparent conflict, and suggest that at least for the case of faces, the response to global contrast inversion is highly dependent on the presence of external facial features. When external features are present, they can activate a contrast-independent mechanism for face detection. How internal and external features are integrated, however, remains unknown. One clue might be provided by the observation that middle face patch neurons respond to inverted contrast faces with external features with much longer latency. It is thus tempting to speculate that higher order face-selective regions are necessary for integrating internal and external facial features, yet, this remains to be validated in future experiments.

Our finding that cells are tuned to both contrast features and to geometrical features extends and complements the previous work by Freiwald et al. (Freiwald, Tsao et al. 2009). The Freiwald et al. study probed cells with parameterized cartoon faces and revealed two important tuning characteristics of cells: they are tuned for the presence of different constellations of face parts and are further modulated by the geometric shape of features such as aspect ratio, inter-eye distance, etc. The cartoon stimuli used in that study contained significant contrast differences between parts (see Figure 8A), but the contrasts were held fixed, thus their contribution to face cell responses was left undetermined. The present study

demonstrates the importance of having both correct contours and correct contrast to effectively drive face-selective cells. While contours alone can drive face-selective cells by a certain amount (Figure 5), correct contrast greatly increases the response, and under some circumstances may be necessary to elicit responses (Figures 6 and 8A).

The second main finding of the Freiwald et al. study was that cells are modulated by complex geometrical features encoded by high frequency information. The current study shows that cells are further modulated by coarse, low-level frequency contrast information. These two properties can in fact be represented in a single cell (Figure 8E), suggesting that cells may be encoding information that is useful both for detection of faces and recognition of individuals. Alternatively, such "dual" tuning characteristics could be a result of recognition processes occurring after detection processes, as predicted by computational models (Tsao and Livingstone 2008); according to the latter view, cells with dual tuning characteristics may nevertheless be contributing exclusively to recognition. Importantly, these two aspects of face cell tuning (tuning to coarse contrast features and tuning to high frequency geometrical contours) are not independent: images with correct contrast features but incorrect contours (Figure 6E), or correct contours but incorrect contrast features (Figure 8B), can both fail to elicit a significant response.

What mechanisms could provide the inputs for establishing the contrast sensitivity of face cells? Exploration of mechanisms for contour representation in area V4, a key area for mid-level object vision (Pasupathy and Connor 2002, Brincat and Connor 2004), suggests that cells in V4 are sensitive to contrast polarity (Pasupathy and Connor 1999). These cells are plausible candidates to provide input to the contrast sensitive cells we observed. Direct

recordings from the inputs to middle face patch cells, e.g., guided by in vivo tracer injections (Ichinohe, Matsushita et al. 2010) or antidromic identification (Movshon and Newsome 1996, Hoffmann, Bremmer et al. 2009), will be necessary to elucidate the contour and contrast tuning properties of face cell inputs.

Faces are a privileged object class in the primate brain, impervious to masking and attracting gaze an order of magnitude more powerfully than other objects (Cerf, Frady et al. 2009). What is the chain of events that enables faces to capture the visual consciousness of a primate so powerfully? Our results shed new light on the nature of templates used by the brain to detect faces, revealing the importance of contrast features. An important question we have not addressed is how these detection templates are read out to drive behavior. We found that different cells encoded different contrast features, suggesting a population code is used to describe a single image. The diversity of contrast features coded by cells in the middle face patches suggests that pooling and readout may be a function of subsequent processing stages, i.e., the problem of face detection has not yet been entirely solved at this stage. Alternatively, cells with face detection capabilities matching perception may already exist in the middle face patches, but constitute a specialized subset which will require more refined targeting techniques to access. Behavioral evidence suggests that a powerful link should exist between face detection machinery and brain areas controlling attention, suggesting a possible approach for tracing the readout neurons.

Figures

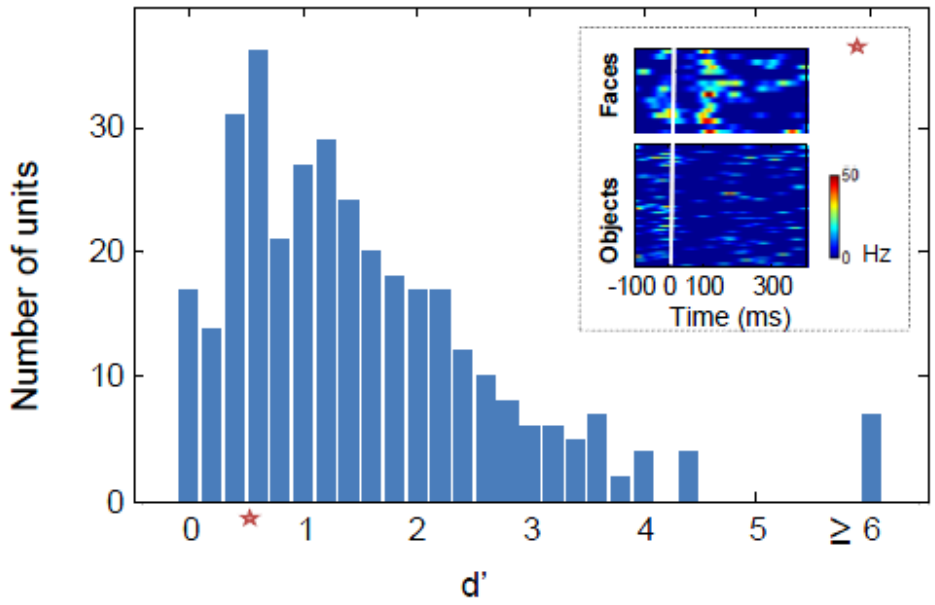

Figure 1. Face discriminability histogram for 342 recorded cells from three monkeys. Discriminability between face and non-face images was quantified with the d' measure. 16 images of faces and 80 images of non-face objects were presented to the monkey in random order. The response for each image was estimated as the average firing rate between [50,250] ms relative to stimulus onset, minus baseline activity between [0,50] ms. Inset depicts responses of an example cell with d'=0.66 (denoted by a red star) to face and object images. Each line represents the PSTH for a given image. All cells with d' > 0.5 were considered to be face-selective.

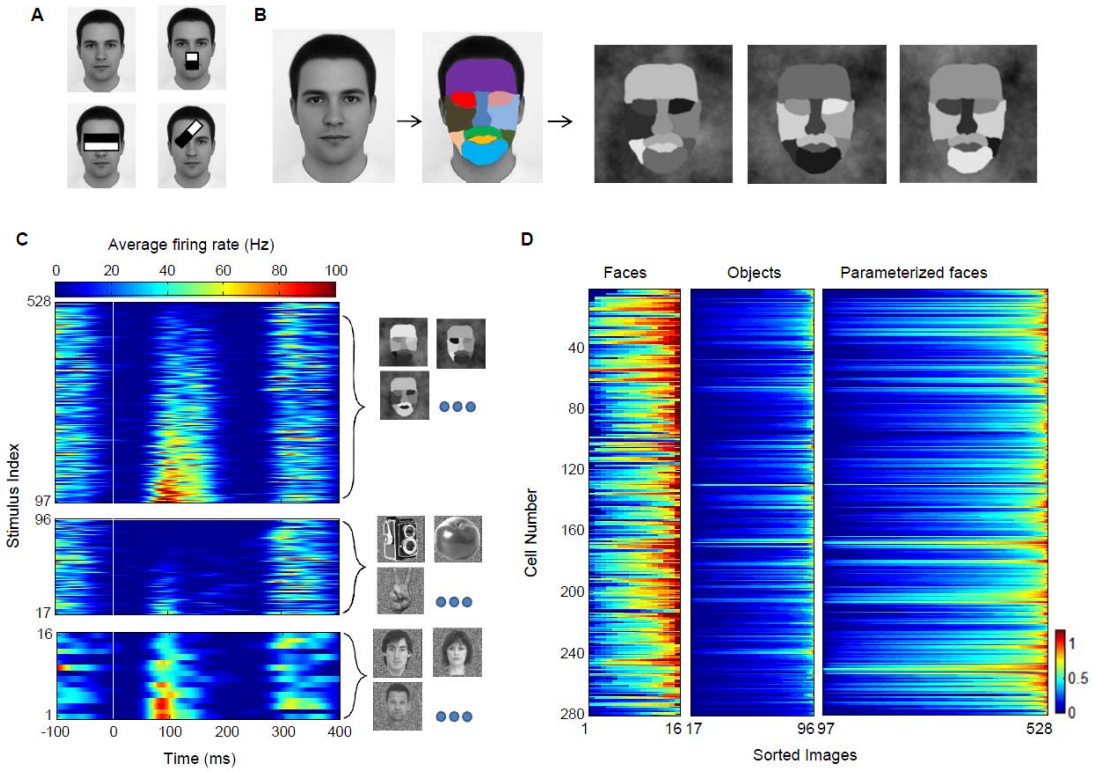

Figure 2. Responses to artificial parameterized face stimuli. (a) Features proposed by computational models for face detection. Each contrast feature has two subparts. The value of a feature is evaluated by summing and subtracting the intensity levels in its sub-region components. (b) Construction of a parameterized face that was used to probe cells for effects of local contrast. An average face was segmented into eleven subparts. Each part was assigned a unique intensity level. Three different instances are shown. (c) PSTH of a single cell to the 432 artificial face stimuli, 80 object stimuli and 16 face stimuli (sorted by mean response magnitude). Images were presented at time zero (white vertical line), for 100 ms and were followed by a gray screen for an additional 100 ms. (d) Normalized average firing rate estimated between [50, 250] ms relative to stimulus onset for all recorded cells in three monkeys. Each row represents one cell. Each group (faces, objects,

parameterized faces) was sorted such that the maximal firing rate is presented on the right for each cell (entries in each column do not correspond to the same stimulus).

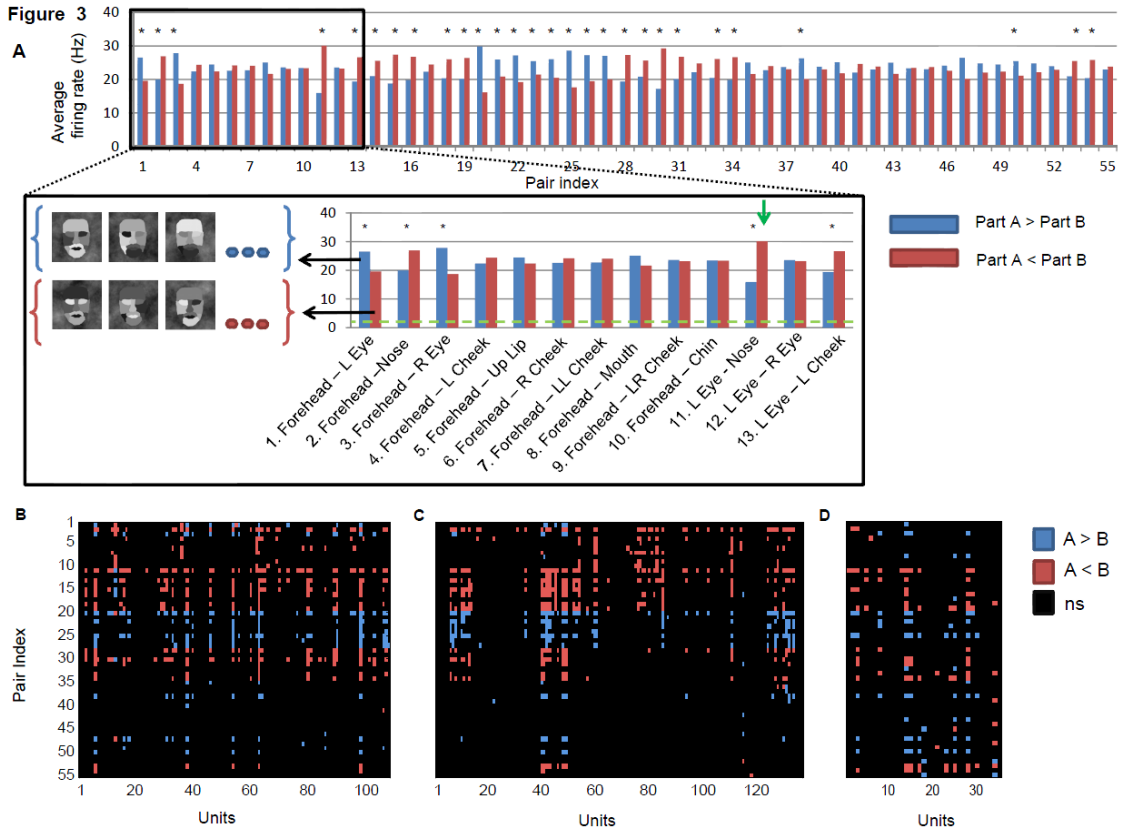

Figure 3. Single cell tuning for contrast polarity features. (a) Parameterized face stimuli were grouped according to whether the intensity in part A was greater or smaller than the intensity in part B. Blue bars represent the firing rate in the condition A>B, and red bars represent the firing rate in the condition B<A. Average firing rate (baseline subtracted) of an example cell to the two polarity conditions across all part pairs is presented (* $P < 10^{-5}$, Mann-Whitney test). Inset shows the first 13 part pairs with several examples of stimuli used in the averaging of the pair (Forehead-Left eye). Green horizontal line represents

baseline activity, and the green arrow represents the largest firing rate difference (15 Hz) (b,c,d). Tuning matrices for monkey (R,H, J) representing which part pair was found to be significant. Blue (red) pixels represent significant tuning for the A>B (A<B) condition.

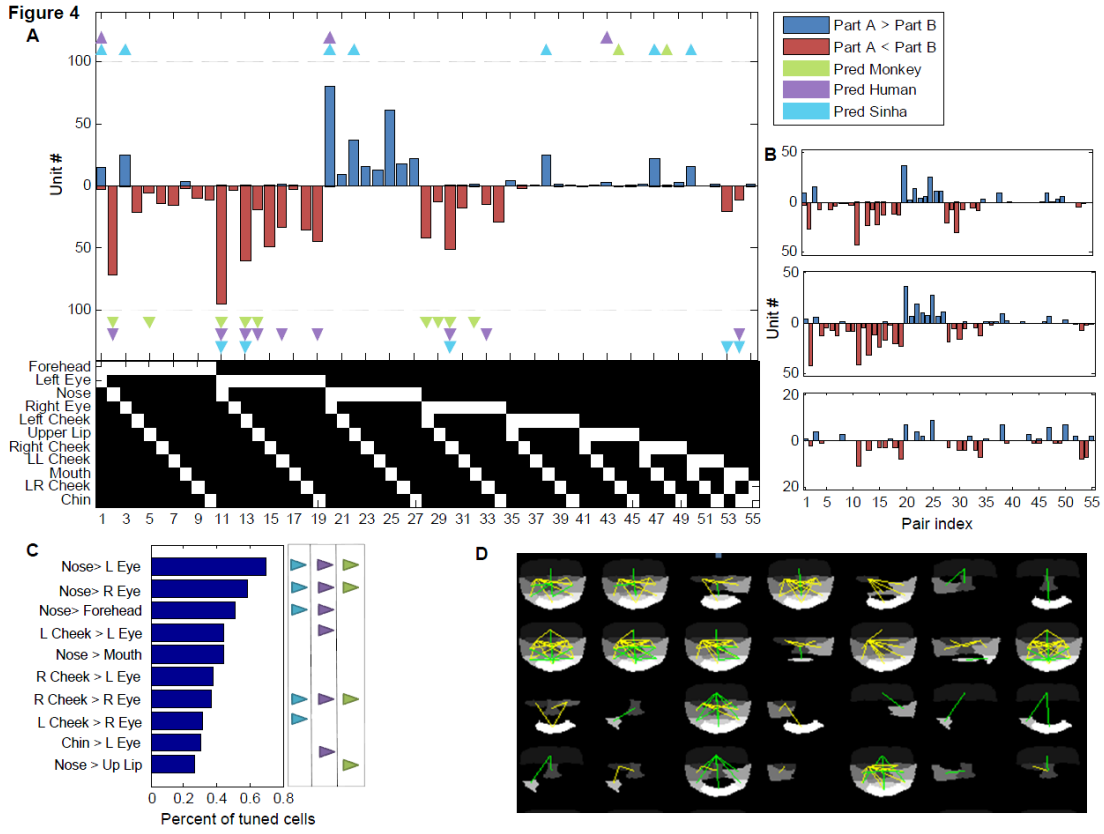

Figure 4. Consistency in contrast polarity preference. (a) Significant contrast feature histogram (data pooled from all three monkeys). Blue (red) bars indicate the number of cells tuned for intensity in part A greater (less) than intensity in part B. Triangles indicate three different feature polarity direction predictions (see Supplementary Fig. 4, main text). The binary table below the histogram denotes the two parts that define each of the 55 pairs; the upper bit represents part A and the lower bit represents part B. (b) Significant contrast

feature histogram for each of the three monkeys (R, H, J, from top to bottom). (c) Most common features and their preferred polarity across the population of cells that were tuned for at least one feature. Model predictions (and prediction's directionality) are represented by small triangles on the right (same convention as in (a)). (d) Graphical representation of feature tuning for a subset of random cells. Yellow lines represent features involving the eye region; green lines represent features which do not involve the eye region.

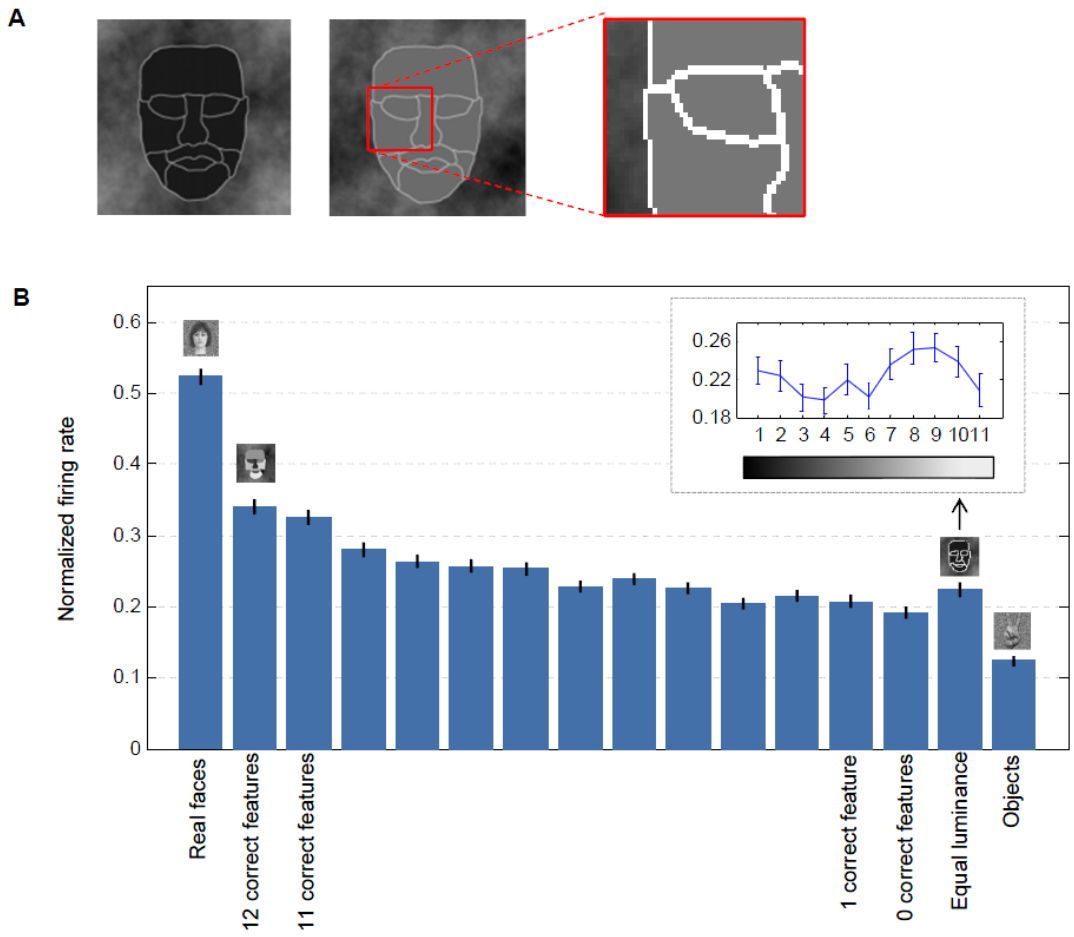

Figure 5. Contribution of contours vs. contrast to firing rate of cells. (a) Two instances of an equal-luminance parameterized face. Each part has the same intensity level and all

contours share the same (but brighter) intensity. (b) Normalized average firing rate (mean ± SEM) for 138 cells that were tuned for at least one contrast polarity feature (pooled across all monkeys). Firing rate of each cell was normalized to the stimulus which elicited the maximal response. Normal parameterized face stimuli are sorted by the number of their correct contrast polarity features. Correct contrast features were considered according to the Sinha model. Small inset shows firing rate variations for the equal luminance variant as a function of intensity level.

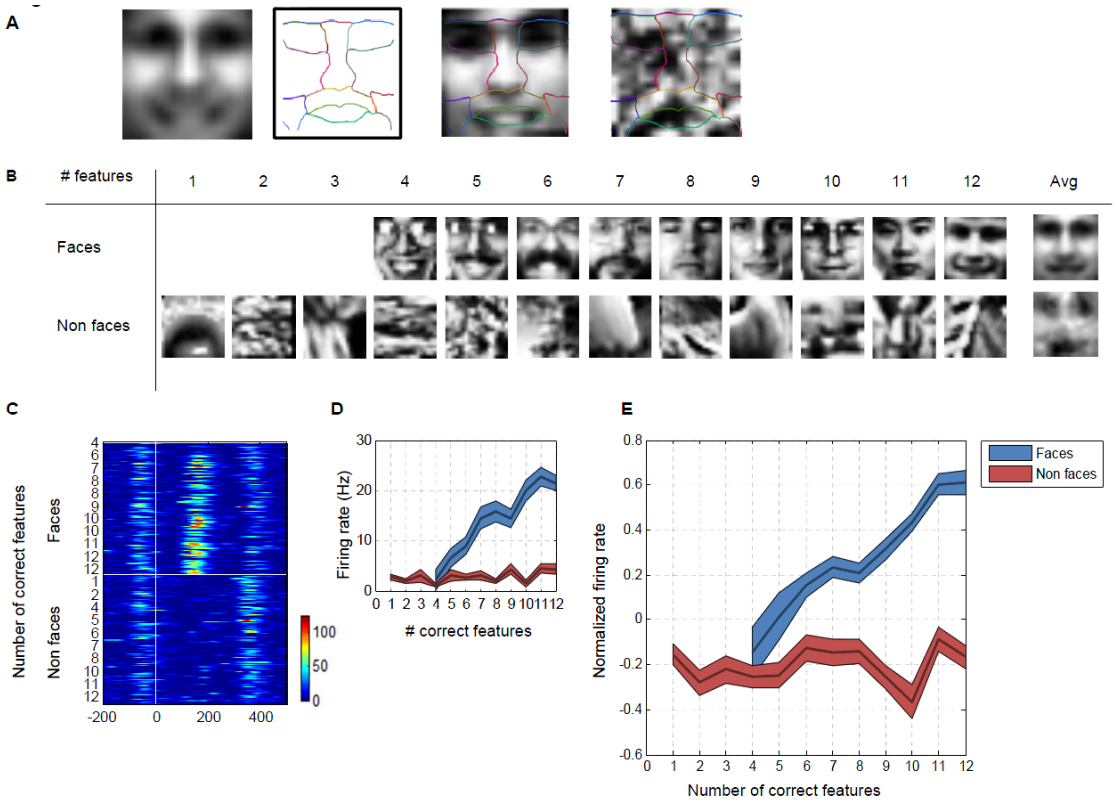

Figure 6. Responses to real face and non-face images as a function of the number of correct contrast features. (a) Left to right: average face computed by averaging all face images in the data set; manual delineation of parts based on the average face; an instance of a face

with the template overlaid; an instance of a non-face with the same template overlaid. (b) Examples of face and non-face images with indicated number of correct features (according to Sinha's model). Last column (Avg) shows the result of averaging all images containing 12 correct features. (c) Single cell PSTH to 207 face and 204 non-face images, sorted by the number of correct contrast features in each stimulus. (d) Average firing rate of the example cell shown in (c), as a function of the number of correct features for faces (blue curve) and non-faces (red). Firing rate was averaged on the interval [50,250] ms without baseline subtraction. Shaded area denotes standard error of the mean. (e) Population normalized firing rate (baseline subtracted) to face and non-face images as a function of the number of correct contrast features.

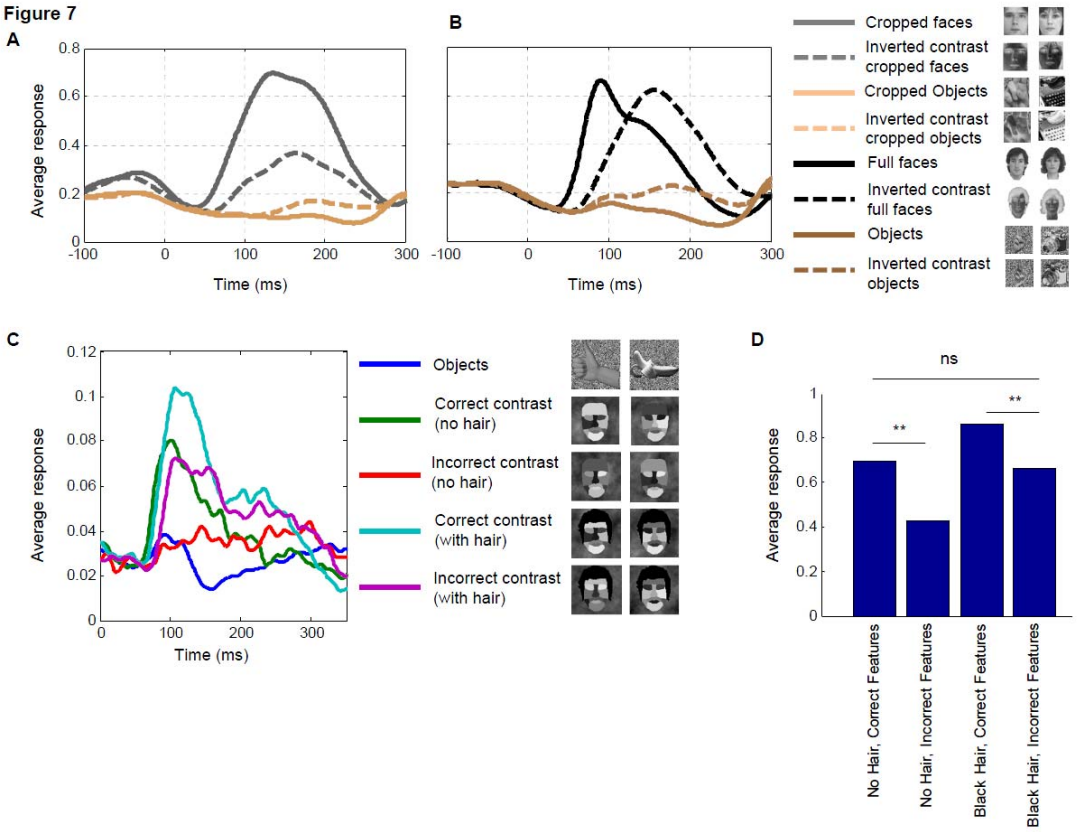

Figure 7. Responses to global contrast inversion. (a) Average population response of 20 cells to normal and inverted contrast real faces and objects. (b) Average population response of 20 cells to normal and inverted contrast cropped faces and cropped objects. Two exemplars from each category are shown in the legend. (c) Average population response of 35 cells to the artificial stimuli controls testing the effect of hair on internal contrast features. Two exemplars from each category are shown in the legend. (d) Average firing rate across the four conditions (** t-test, $p<0.01$).

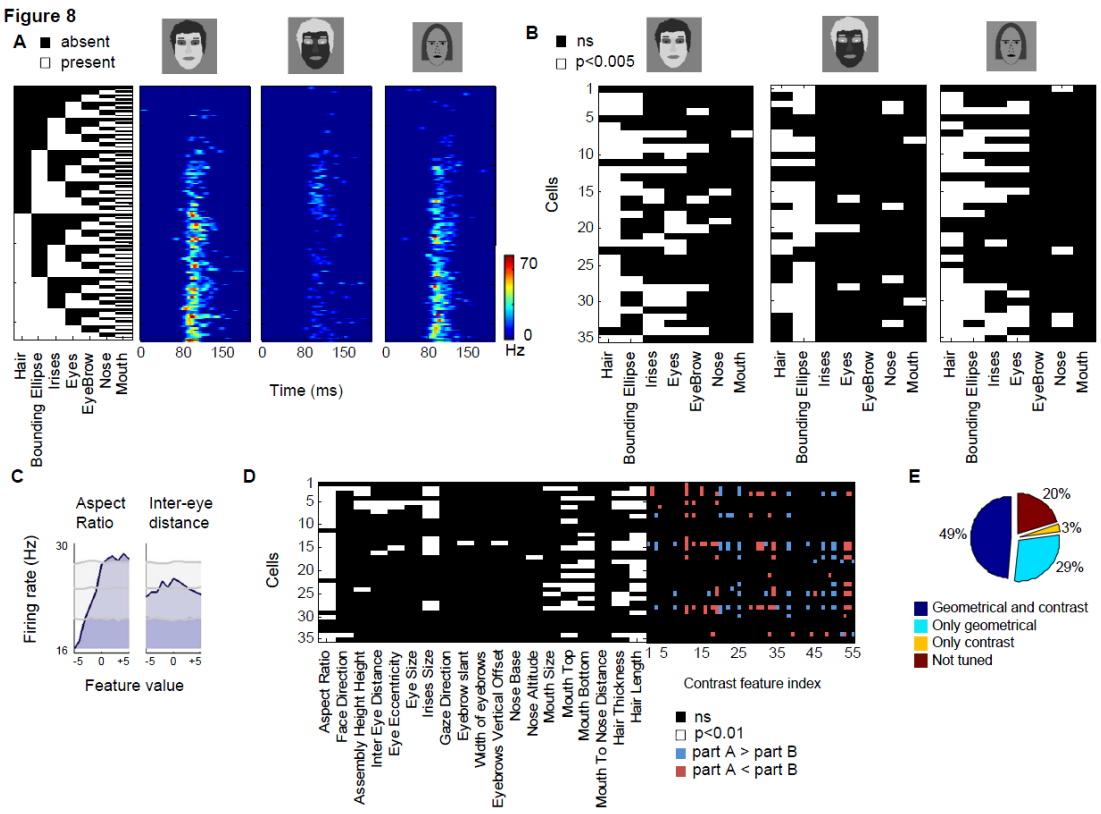

Figure 8. Relationship between tuning to part contrast, part presence, and part geometry. (a) Responses of a single cell to a decomposition of a face stimulus with correct contrast (left), inverted contrast (middle) and cartoon (right). For each row, the parts present are indicated by the white squares in the black and white matrix. (b) Significant tuning of all cells to presence of parts across the three stimulus conditions (7-way ANOVA, $p<0.005$). Each row represents a single cell and its tuning to parts across the three different decompositions. The cell shown in (a) is represented in the last row. (c) Tuning for geometrical features. Tuning of an example cell to two feature dimensions (aspect ratio, inter-eye distance); the tuning curve (blue) is shown at a delay corresponding to maximal modulation. Maximal, minimal, and mean values from the shift predictor are shown in

gray. (d) Significant geometrical feature tuning across all 35 cells (each row represents tuning of a single cell). Right block, tuning of the same cells to contrast polarity features. (e) Percentage of cells tuned for geometrical and contrast features.

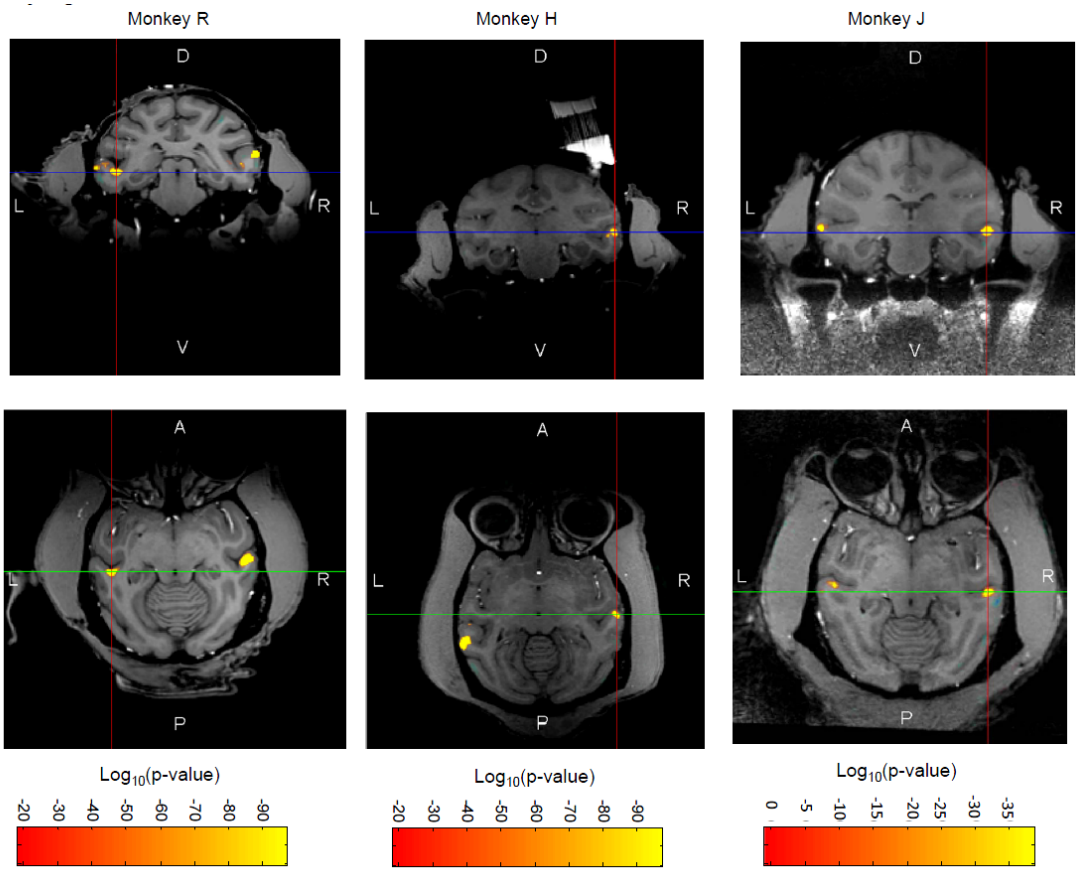

Supplementary Figure 1. MR guided electrophysiology. Coronal and sagittal MR slices showing electrode targeting ML (Monkey H, J) and MF (Monkey R). Face patch ML in monkey H was located at 5 mm anterior to the interaural line (+5, AP) axis, +29 along the medial-lateral (ML) axis, and +15 along the dorsal-ventral (DV) axis. Face patch MF was targeted in monkey R at AP +3.5, ML -23, and DV +13. Face patch ML in monkey J was targeted at AP +5, ML +27, DV +12.

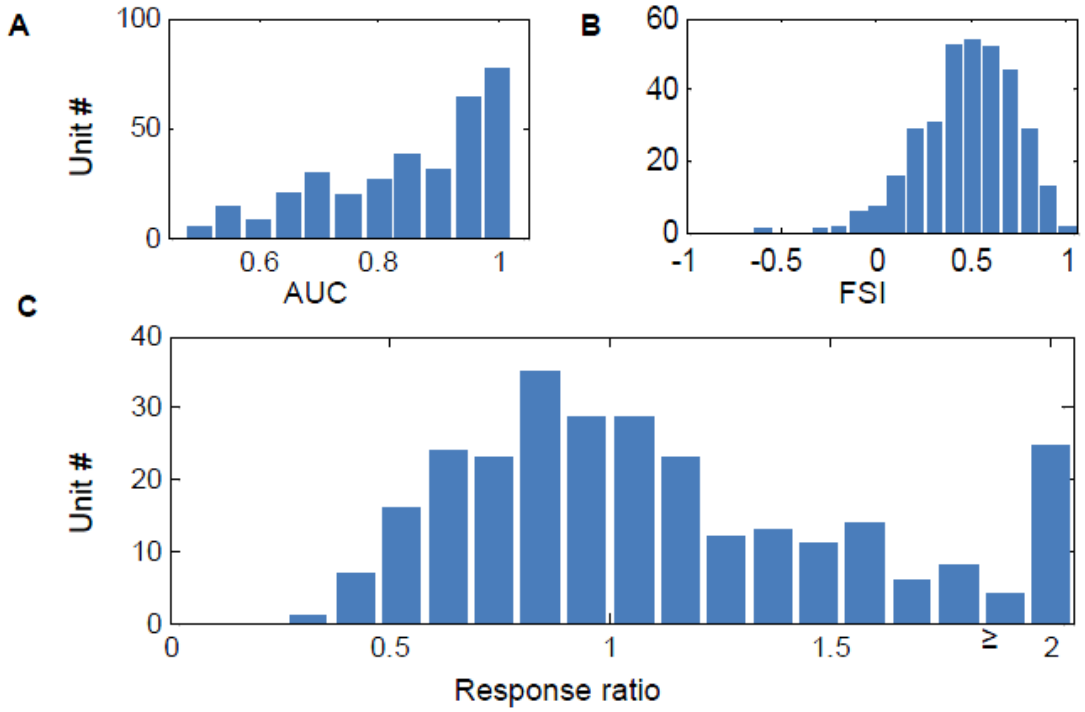

Supplementary Figure 2. Alternative measures for face selectivity and maximal evoked response by artificial face stimulus. (a) Face discriminability histogram for 342 recorded cells from three monkeys. Discriminability between face and non-face images was quantified with the AUC measure. (b) Face selectivity index histogram for 342 recorded cells from three monkeys. (c) Population histogram for the response ratio between the maximal evoked response to a parameterized face and the maximal evoked response to a real face. Values greater than one indicate that one of the parameterized faces elicited a response greater than the maximal response evoked by a real face.

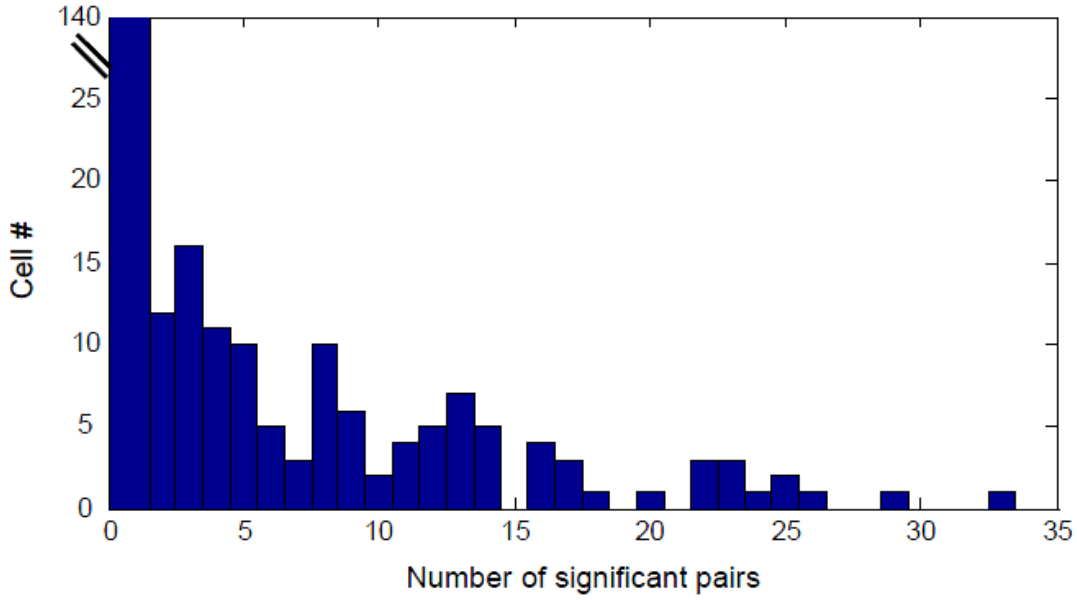

Supplementary Figure 3. Histogram of the number of significant contrast polarity features found in all three monkeys.

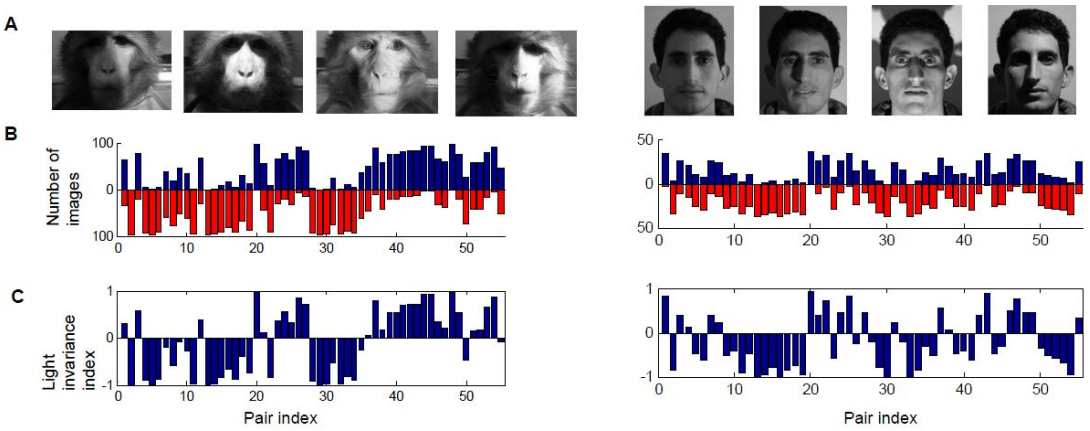

D

Human (Small Set) Light Invariance Index		Monkey (Small Set) Light Invariance Index	
1.00	L Cheek > L Eye	1.00	Nose > Forehead
1.00	L Cheek > L Eye	1.00	L Cheek > L Eye
1.00	R Cheek > R Eye	1.00	Nose > R Eye
1.00	LR Cheek > R Eye	1.00	Up Lip > R Eye
0.95	Up Lip > L Eye	0.98	Up Lip > Forehead
0.95	Chin > L Eye	0.98	R Cheek > LR Cheek
0.95	Nose > R Eye	0.96	Nose > L Eye
0.89	Chin > Mouth	0.96	Up Lip > L Eye
0.89	Nose > L Eye	0.96	R Cheek > R Eye
0.84	Up Lip > Mouth	0.96	Mouth > R Eye
0.84	Forehead > L Eye	0.92	L Cheek > R Eye
0.84	Nose > Forehead	0.92	Up Lip > LR Cheek

E

Predicted correct polarity features	Number of cells tuned for the predicted polarity	Number of cells tuned for opposite polarity predicted
Forehead > L Eye	15	3
Forehead > R Eye	25	1
L Cheek > L Eye	60	1
R Cheek > R Eye	51	1
Nose > L Eye	95	1
Nose > R Eye	80	1
Nose > Up Lip	37	0
L Cheek > Mouth	25	0
R Cheek > Mouth	22	1
LL Cheek > Mouth	16	0
LR Cheek > Mouth	20	0
Chin > Mouth	11	0

Supplementary Figure 4. Illumination invariance of contrast polarity features. (a) Several images of monkey and human faces used to estimate illumination-invariant contrast features. (b) Histogram of the number of images voting for a particular contrast polarity direction (Part A > Part B, or the opposite condition) for all 55 features (left, monkey; right, human). Feature table is given in Supplementary Table 1. Each feature was composed of two of the following parts: forehead, left (right) eye, nose, left (right) cheek, chin, mouth, and lower left (right) cheek. The polarity of a feature was determined by computing the median intensity level in each region and computing the sign of the difference. (c) Light invariance indices derived from (b). Illumination invariance index for each pair was defined as $\frac{\#Pos - \#Neg}{\#Pos + \#Neg}$. Invariance index of 1 or -1 denotes that all images voted for the same polarity direction. Zero denotes

that half of the images voted for condition A>B and half for A<B. (d) Table of 12 most predictive features (sorted by their light invariance index). (e) Predicted polarity features according to Sinha's face detection model[Sinha, 2002] and the number of cells found tuned for the predicted polarity (pooled from all three subjects).

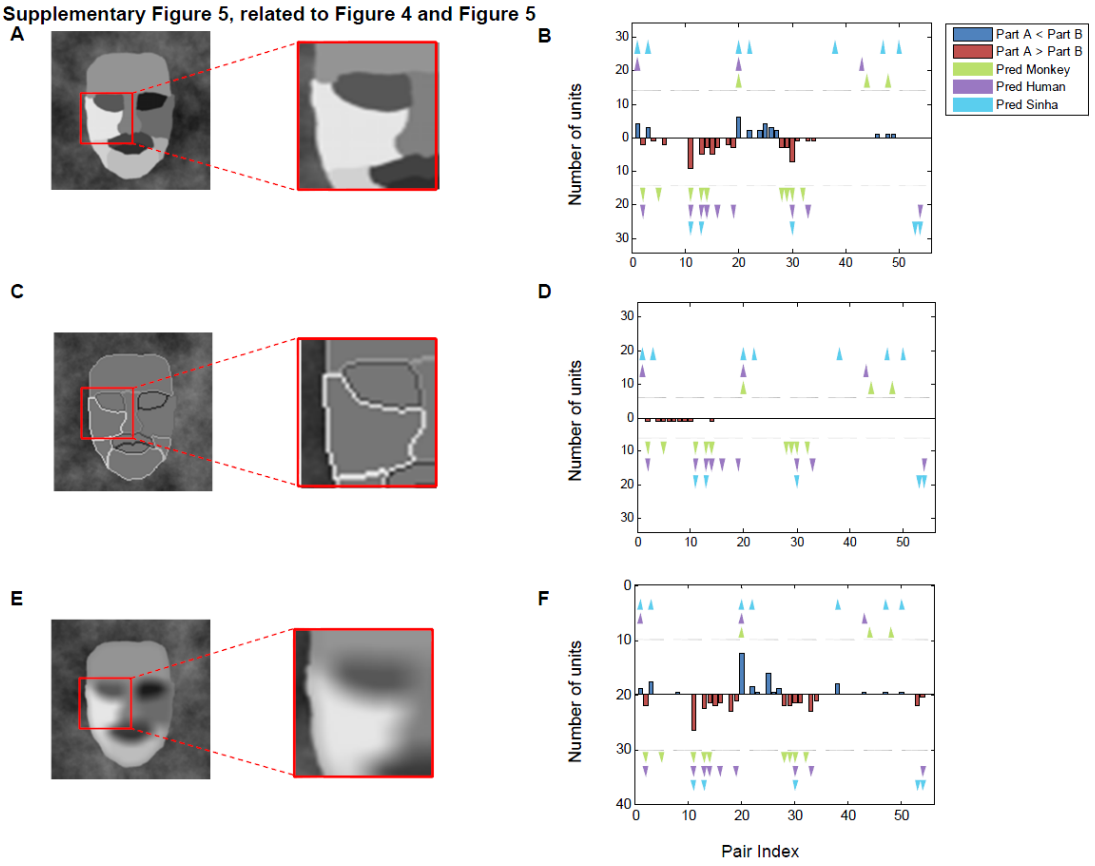

Supplementary Figure 5. Contribution of low frequencies to contrast polarity tuning. (a) Enlarged region of the original version of the artificial face stimulus. (b) Contrast polarity histogram for 18 face-selective cells from Monkey R to the original version of the artificial face stimulus. (c) A variant of the parameterized face stimulus preserving contrast relationships along contours. Enlarged region shows that same intensity levels were used for each part, but were confined to a narrow band along the boundary between parts. (d) Contrast

polarity histogram for the same 18 cells shown in (b) to the presentation of the variant shown in (c). (e) A low pass version of the parameterized face stimulus. (f) Histogram of contrast polarity tuning across a population of 34 face-selective cells from monkey R for the low pass version shown in (e).

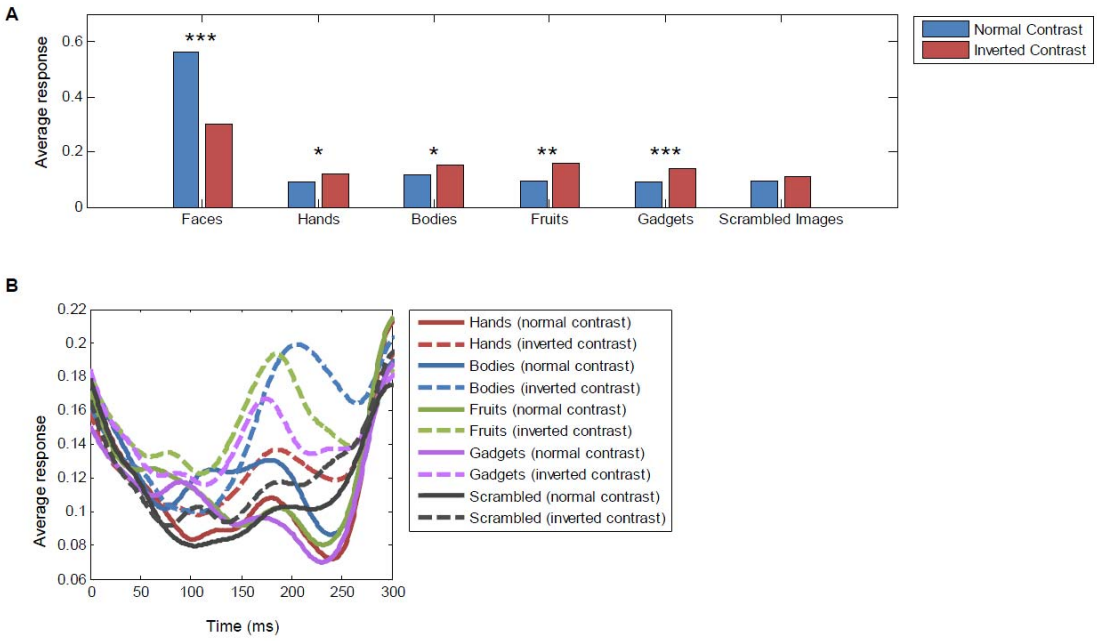

Supplementary Figure 6. Responses to contrast-inverted objects and cropped faces. (a) Average firing rate for a population of 20 face-selective cells. Each category (faces, hands, bodies, fruits, gadgets, scrambled images) contained 16 images. Statistical significance is denoted by * (P<0.05), ** (P<0.01) , *** (P<0.001). (b) Average PSTH for the different categories. Stimulus onset is at time zero.

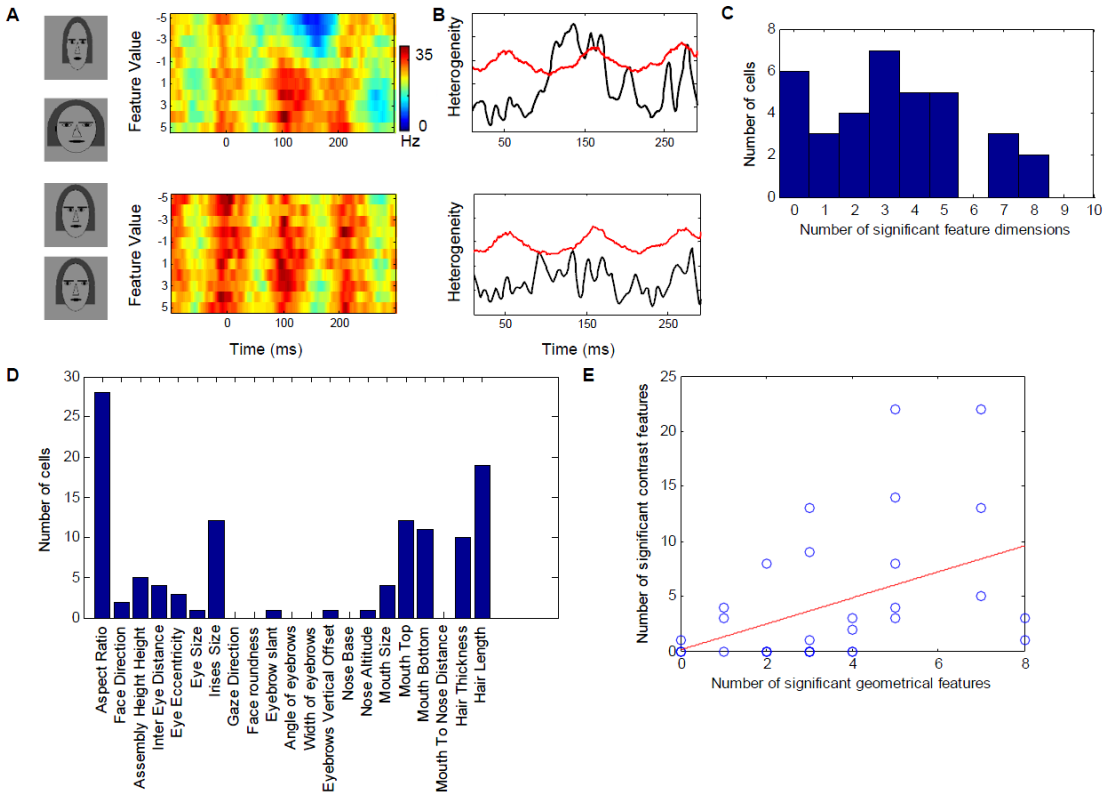

Supplementary Figure 7. Tuning to geometrical features. (a) Time-resolved tuning curves for an example cell. Each row represents the average response for a given feature value (image onset at time 0). (b) Time-resolved heterogeneity (black curve) and predicted heterogeneity from shift predicator (red). (c) Histogram of the number of tuned feature dimensions found in 35 cells. (d) Histogram of the most common geometrical features. (e) Correlation between the number of significant contrast polarity features and the number of significant geometrical features (R^2= 0.21).

1	Forehead - Left Eye	21	Nose - Left Cheek	41	Upper Lip - Right Cheek
2	Forehead - Nose	22	Nose - Upper Lip	42	Upper Lip – Lower Left Cheek
3	Forehead - Right Eye	23	Nose - Right Cheek	43	Upper Lip - Mouth
4	Forehead - Left Cheek	24	Nose – Lower Left Cheek	44	Upper Lip – Lower Right Cheek
5	Forehead - Upper Lip	25	Nose - Mouth	45	Upper Lip - Chin
6	Forehead - Right Cheek	26	Nose – Lower Right Cheek	46	Right Cheek - LL Cheek
7	Forehead – Lower Left Cheek	27	Nose - Chin	47	Right Cheek - Mouth
8	Forehead - Mouth	28	Right Eye - Left Cheek	48	Right Cheek – Lower Right Cheek
9	Forehead – Lower Right Cheek	29	Right Eye - Upper Lip	49	Right Cheek - Chin
10	Forehead - Chin	30	Right Eye - Right Cheek	50	Lower Left Cheek - Mouth
11	Left Eye - Nose	31	Right Eye – Lower Left Cheek	51	Lower Left Cheek – Lower Right Cheek
12	Left Eye - Right Eye	32	Right Eye - Mouth	52	Lower Left Cheek - Chin
13	Left Eye - Left Cheek	33	Right Eye – Lower Right Cheek	53	Mouth – Lower Right Cheek
14	Left Eye - Upper Lip	34	Right Eye - Chin	54	Mouth - Chin
15	Left Eye - Right Cheek	35	Left Cheek - Upper Lip	55	Lower Right Cheek - Chin
16	Left Eye – Lower Left Cheek	36	Left Cheek - Right Cheek		
17	Left Eye - Mouth	37	Left Cheek – Lower Left Cheek		
18	Left Eye – Lower Right Cheek	38	Left Cheek - Mouth		
19	Left Eye - Chin	39	Left Cheek – Lower Right Cheek		
20	Nose - Right Eye	40	Left Cheek - Chin		

Supplementary Table 1. Table of all 55 contrast features.

Chapter 3: Exploring optogenetic tools in the non-human primate

“It's a revolution. But we're catching up to the revolution that had been going on for the rest of the world."

- *Robert Desimone*

Introduction

An important step in understanding a cortical circuit is to precisely perturb activity in specific nodes of the circuit. Electrical microstimulation has been widely used in non-human primates (NHP) as a tool to probe perception (Salzman, Britten et al. 1990, Murphey and Maunsell 2007), decision making (Cohen and Newsome 2004, Moore and Fallah 2004), motor control (Graziano, Taylor et al. 2002), and network connectivity (Ekstrom, Roelfsema et al. 2008, Moeller, Freiwald et al. 2008, Logothetis, Augath et al. 2010). However, the effects of electrical microstimulation and its spread are still poorly understood (Histed, Bonin et al. 2009), and the technique has several drawbacks including inability to monitor activity during stimulation due to electrical artifacts, inability to target specific sub-populations of neurons, and difficulty in interpreting results due to the possibility of activating fibers of passage. Optogenetics is an emerging technology that can overcome many of these limitations by targeting specific cell populations (Yizhar, Fenno et al. 2011) and control neural activity to millimeter and millisecond precision (Boyden, Zhang et al. 2005).

Although optogenetics has been successful in altering and evoking motor movements in rodents (Gradinaru, Thompson et al. 2007), several attempts in the macaque failed to find any behavioral effects despite strong light-induced modulation of neural activity in pre-motor cortex (Diester, Kaufman et al. 2011), parietal regions (Han, Chow et al. 2011), FEF (Han, Qian et al. 2009), primary visual cortex (Ruiz, Lustig et al. 2013), and subcortical areas involved in motor planning and execution (Galvan, Hu et al. 2012). This is surprising because electrical microstimulation in the same areas of the same animals were found to reliably evoke limb (Diester, Kaufman et al. 2011) and eye movements (E. Boyden, personal

communication). Recently, three studies reported observable behavioral changes (Cavanaugh, Monosov et al. 2012, Gerits, Farivar et al. 2012, Jazayeri, Lindbloom-Brown et al. 2012), but only Jazayeri et al. were successful in evoking a movement following optical stimulation (ChR2 in primary visual cortex), suggesting stimulation evoked a phosphene percept to which monkeys were trained to respond. While these studies are important in providing evidence that optogenetic perturbations can lead to behavioral changes, they do not address the issue of how effective such perturbations are in comparison to known methods of perturbing behavior. Furthermore, the puzzle of why robust neural modulation can be evoked in motor areas without any observable induced motor behavior persists.

Various explanations have been proposed to explain the lack of behavioral effects induced by optical stimulation in NHPs including low cell infection percentage, labeling of cells that do not participate in behavior, small region of stimulated tissue, lack of stimulation of fibers of passage, low stimulation frequencies, and monitoring methods not subtle enough to observe possible effects. In this study, we examined the effects of five optogenetic constructs in the macaque frontal eye field (FEF) side-by-side with electrical micro-stimulation, to assess whether optical perturbation of the local network leads to observable motor changes during optical, electrical and combined stimulation. Our experiments address these concerns and suggest that ChR2 stimulation contributes to the initiation of movements, but in most cases stimulation evokes sub-threshold activity which is not sufficiently strong to evoke a motor response.

Methods

Experimental procedures

All procedures conformed to local and US National Institutes of Health guidelines, including the US National Institutes of Health Guide for Care and Use of Laboratory Animals. All experiments were performed with the approval of the Caltech Institutional Animal Care and Use Committee (IACUC) and the Caltech Institute Biosafety Committee.

FEF targeting

The frontal eye field was identified by anatomical landmarks in three macaque monkeys (males). Recording chamber placement and electrode trajectories were planned with Planner (Ohayon and Tsao 2012), a custom designed software for MRI-guided electrophysiology. Chambers were not aligned to stereotactic coordinates, hence, electrode trajectories span multiple AP slices (see Table 1).

Constructs and viral injection

Five different constructs with comparable titers were used in this study. AAV5-hSyn-eNpHR3.0-eYFP ($3x10^{12}$ virus molecules/ml), AAV5-hSyn-ChR2(H134R)-eYFP ($4x10^{12}$ virus molecules/ml), AAV5-hSyn-ChR2(E123A)-eYFP ($4x10^{12}$ virus molecules/ml), and AAV5-CamKII-ChR2(E123A)-mCherry ($4x10^{12}$ virus molecules/ml) were obtained from the Deisseroth Lab, Stanford. AAV5-CAG-ArchT-eGFP ($1x10^{12}$ virus molecules/ml) was obtained from the Boyden Lab, MIT. Constructs were packaged at the vector core facility at the University of North Carolina.

We injected 1 µl of virus for each 0.5 mm of cortex. Injections were restricted to sites in which single units were found and saccades could be evoked (with the exception of eNpHR3.0 site in monkey B). Capillary tubing (360 um OD, TSP200350, Polymicro) was filled with paraffin oil (Omega) using a 100 µl gas tight syringe (1710TTL, Hamilton) and a microinjection pump (UMP3 and SYS-MICRO4, WPI). Viral vectors were injected using a 32G injection needle (Hamilton, point style 4) connected to an elbow joint (C360-205, LabSmith), which was connected to a micro-manipulator drive (MO-97A, Narishige). A 23G guide tube was used to penetrate the dura and was placed in a grid (Crist instruments) sitting in the cranial chamber. The needle was slowly lowered (0.25 mm/min) to the injection site and 1 µl was injected at a rate of 40 nl/min. We monitored the injected quantity using a blue food dye (Esco Foods, Inc) preloaded into the tubing. We then waited 10 minutes for the virus to diffuse before slowly lowering the needle and repeating the procedure. All viral injections were performed in the same day in monkeys J and A. Monkey B went through two viral injection sessions separated by 6 months. Injections took place while animals were sedated (Dexdormitor 0.02 mg/kg).

Monkey J and B were injected with AAV5-hSyn-ChR2 (H123R)-eYFP, a membrane channel which excites neurons upon blue light illumination (Boyden, Zhang et al. 2005); AAV5-hSyn-eNpHR3.0-eYFP (*Natronomonas pharaonis* halorhodopsin), a chloride pump which inhibits neurons upon yellow or green light illumination (Gradinaru, Thompson et al. 2008, Gradinaru, Zhang et al. 2010) and AAV5-CAG-ArchT (Archaerhodopsin), a proton pump which inhibits neurons upon green light illumination (Chow, Han et al. 2010, Han, Chow et al. 2011). Monkey A was injected with AAV5-hSyn-ChR2(E123A), a mutant ChR2

with faster channel kinetics and AAV5-CamKII-ChR2(E123A), a mutant ChR2 with faster channel kinetics under a cell-type specific promoter for excitatory neurons (Gunaydin, Yizhar et al. 2010, Mattis, Tye et al. 2012).

Monkey A was first tested for neural modulations two weeks post injection (modulations found) and was tested for paired stimulation (optical, electrical) three weeks after injection (for two weeks). Monkey B was first tested for neural modulations three weeks post injection (modulations found) and tested for paired stimulation three and a half weeks post injection (for several months). Monkey J was first tested for neural modulations a month post injection (modulations found) and tested for paired stimulation five weeks post injection (for several months).

Optical stimulation

Optic fibers (BFL 22-200, Thorlabs) with furcation tubing were stripped for 10-15 cm using special stripping tools (FTS3, T16S31, ThorLabs) to expose the core. Super glue (modified ethyl cyanoacrylate, Dymax 222/3, Dymax Corporation) was used to attach electrodes at an offset of 0.5-1 mm relative to the tip of the optic fiber. Light was delivered using laser (DPSS 473 nm, 532 nm, Shanghai Lasers) coupled to optic fibers using **F**C/PC connectors (ADAFC2-PMN, Thorlabs). Laser light levels were measured prior to each experiment using a power meter (PM100D, S130C, Thorlabs).

Electrophysiology

Neural signals were recorded using Plexon (MAP, Plexon Inc.). LFP was filtered at 0.7-300 Hz and single and multiunit were filtered at 0.15-8 kHz and recorded at 40 kHz. Low impedance electrodes (50-100 kOhm, UEWLEJSMAN1G, FHC) were used for recording

and stimulation. Impedance was measured prior to experiments (NanoZ, White Matter ltd). Units were sorted offline semi-automatically using KlustaKwik (Kenneth D. Harris 2000). Units were classified as multiunit if more than 2% of the recorded spikes had an inter-spike interval smaller than 2 ms. A unit was defined as significantly modulated by light if the average number of spikes during baseline was significantly different (two tail paired t-test) compared to the average number of spikes during the stimulation period. Baseline period was matched for the duration of optical stimulation to ensure equal variance. Optical stimulation latencies were defined as the first time point in which average firing rate (smoothed using a Gaussian kernel, σ=2 ms) exceeded four times the standard deviation during baseline. For the analysis of firing rate changes (Figure 2a), three recording sessions were discarded (two in monkey B and one in monkey J) in which multiple optrodes were lowered to two sites simultaneously. The majority of units were collected from the same grid hole used for the viral injection (see Table 1).

Electrical microstimulation

Electrical microstimulation was delivered using a current isolator (A365, WPI) and monopolar electrodes with impedance of 50-100 kOhm (FHC). Biphasic pulses were delivered at 300 Hz, each pulse lasting 0.15-0.25 ms with 0.15 ms inter-pulse separation, cathodal leading. Currents varied between 10 – 90 μA. Pulses were generated with custom hardware (Arduino Due); pulse jitter < 5 μs.

Eye movements, saccades, and task

Monkeys were head fixed and passively viewed a screen (DELL P1130) in a dark room. A small fixation spot (0.25 degrees in diameter) was presented in the center of the screen. Eye

position was monitored during the experiments using an ISCAN system running at 120 Hz. Juice rewards were delivered every 2-3.5 seconds when the monkey fixated the dot. Juice reward was still delivered if monkeys broke fixation for periods shorter than 300 ms (allowing blinks or saccades evoked by electrical microstimulation). Eye traces were aligned in time to stimulation onset and in space to the position of the eye at t=0 (i.e., x(t=0)=y(t=0)=0). We defined the baseline interval of a trial to be 150 ms prior to stimulation onset to 50 ms post stimulation and discarded stimulation trials during which there was no stable baseline, typically corresponding to eye blinks or saccades just prior to the stimulation trial. For measuring saccade amplitude, eye position was defined as: $\sqrt{(x)^2 + (y)^2}$. Circular statistics were computed with CircStat (Berens 2009). Saccade direction and amplitude were estimated by averaging the instantaneous measures at 150-200 ms relative to stimulation onset. Stimulations (both electrical and optical) were considered successful if they evoked a saccade with amplitude greater than 1.8 visual degrees and were within 40 degrees of the average saccade direction (evoked with the highest electrical current). Saccade latencies were defined as the first time point at which eye position exceeded five times the standard deviation during baseline for 10 ms continuously.

To determine whether a significant increase in saccade probability occurred during combined optical and electrical stimulation, we used the binomial distribution to estimate likelihood of observing k out of N saccades, with baseline success probability in each trial obtained from the fraction of successful saccades during electrical stimulation alone. On average, in each experiment we delivered 22±10 electrical stimulations, 21±9 combined electrical and optical

stimulations, and 132±45 optical stimulations alone. The number of coupled stimulations did not differ statistically from the number of electrical stimulations ($p>0.5$, paired t-test).

To generate normalized current plots we mapped the lowest current level used to 0 and highest current to 1 and linearly interpolated percentages. In half of the trials, stimulation was delivered while the fixation spot was visible and in the other half of the trials stimulation was delivered after the spot was extinguished (Goldberg, Bushnell et al. 1986). For estimating saccade accuracy, the concentration parameter κ was estimated from a Von-mises distribution: $f(x \mid \mu, \kappa) = \frac{e^{\kappa \cos(\mu - x)}}{2\pi I(\kappa)}$, where μ is the mean saccade direction and I is the modified Bessel function of order 0.

MRI/fMRI

Structural MRIs were taken in Siemens 3T with a single loop coil. Isotropic 0.5 mm resolution scans were obtained using the following parameters: TR: 2300 ms, TE: 2.94 ms, 256 slices, Field of View (FoV): 128 mm, FoV phase: 100%, slice thickness: 0.5 mm, bandwidth:190 Hz/Px, phase encoding: F>>H, 0% phase oversampling.

fMRI scans were taken in a Siemens 3T with AC88 gradient insert using custom eight channel coil. Full brain coverage scans were obtained at 1 mm isotropic resolution with the following parameters: TR: 2000 ms, TE: 17 ms, number of slices: 54, FoV: 96 mm, FoV phase: 100%, slice thickness: 1 mm, bandwidth: 1860 Hz/Px, phase encoding: F>>H, 0% phase oversampling, PAT2 with GRAPPA reconstruction. Prior to scanning, a contrast enhancing agent was injected to the blood (Feraheme, 8 mg/kg). During scanning, the monkey was required to fixate a small white dot (0.25 deg) on a gray background, while

electrical or optical stimulation were applied. Juice rewards were given during rest blocks after three seconds of continuous fixation and randomly (every 2-4 seconds) during stimulation blocks (since the monkey could not hold fixation due to stimulation). Eye position was monitored using a camera and infrared light (ISCAN) sampled at 120 Hz.

Stimulation parameters used during the fMRI scans. Electrical: train rate = 1 Hz, train length = 200 ms, pulse frequency = 300 Hz, pulse width = 250 μs, electrical current = 50-300 μA, pulse shape = rectangular biphasic pulses with 100 μs separation between pulses. Optical: train rate = 1 Hz, train length = 900 ms, pulse frequency = 80 Hz, pulse width = 8 ms, irradiance 82 – 381 mW/mm^2.

fMRI designs and data analysis

To determine significance levels, we used the General Linear Model (GLM) to analyze the time courses. We defined four explanatory variables: Rest (inter stimulation blocks), Optical (optical stimulation alone), Electrical (electrical stimulation alone), and Combined (electrical and optical stimulation). We modeled the combined stimulation blocks with an additional explanatory variable to allow non-linear interactions between the two stimulation types. Blocks were either 40 or 32 seconds long. 13-20 runs were collected per monkey. Analysis was done using available analysis packages (motion correction: AFNI, GLM fitting: FSFast). Visualizations and data post processing were done with custom scripts written in Matlab (Mathworks) and Freesurfer. Raw signal was converted to percent change and the sign was flipped (due to Feraheme). Data was smoothed with a spatial 1 mm isotropic Gaussian kernel and with a 1 second Gaussian kernel along the time axis. ROI analysis was performed using an ROI selected based on anatomical landmarks (known optrode tip position).

Histology

Monkey B was perfused with 4% PFA (4 L) and then with a 4% PFA + 10% sucrose (1 L). The brain was removed and placed in 4% PFA and 10% Sucrose for 2 days, and then in 4% PFA and 20% Sucrose for 4 days. 50 μm full-brain sections of frozen tissue were taken with a microtome (American Optical Company, Model 860, Buffalo NY). Immunohistochemistry primaries used were: DAPI (1:50,000, D9542 Sigma), Anti-NeuN (1:5000, Millipore MAB377), Anti-CamKII (1:50, SantaCruz sc-13082), Anti-Parvalbumin (1:5000, Sigma P3088), Anti-GFAP (1:5000, Sigma G3893). Sections were incubated with primaries and PGT (Gelatine 2 g/L, 0.25% Triton in PBS) solution overnight (except Anti-CamKII, which was incubated for 72 h in a cold room). Sections were triple washed with PBS and then incubated with secondary antibodies for two hours: Anti-Rabbit Cy5 (A10523, Invitrogen), Anti-Mouse Cy3 (A10521, Invitrogen). Sections were mounted on glass slides (5075-FR, Brain Research Laboratories) using ProLong Gold Antifade Reagent (P36934, Invitrogen). Slides were imaged with Olympus confocal FV1000 using UPLSAPO 10x 0.40 NA lens. Custom software for visualization, registration and annotation was developed in Matlab. 2D affine transformation was used to register high-magnification Z-stack images to a wide-field fluorescence image. The latter was then registered using another 2D affine transformation to the corresponding photograph of the frozen tissue block. The entire frozen tissue block was then registered using 3D affine transformation to the MRI scan using Planner (Ohayon and Tsao 2012). Two brain series spanning the FEF were used for the quantitative histological anaylsis: 1) NeuN, DAPI, YFP, GFAP and 2) CamKII, PV, YFP, DAPI.

Results

Localization of FEF and viral injection

We localized the FEF in three monkeys according to anatomical landmarks in MRI scans. Within the FEF of each monkey, a recording chamber was implanted (not perpendicular to the cortical surface, Figure 1a, b, MRI reconstructions aligned to chamber coordinates). Electrode trajectories targeted the anterior bank of the arcuate sulcus.

We electrically stimulated each of the sites prior to injections and tested whether saccades could be evoked with currents lower than 50 μA. Saccadic eye movements with similar characteristics to previous studies (Bruce, Goldberg et al. 1985) were evoked by electrical stimulation in 7 out of 8 of the injection grid holes (Figure 1c, d), with the exception of eNpHR3.0 site in Monkey B (which was on the rim of the arcuate sulcus). Electrically evoked saccades started 87.9± 35 ms after stimulation. We observed saccade amplitudes ranging between 2-30 visual degrees across the different sites (Figure 1d). Saccade direction changed along the penetration (e.g., Figure 1d, ChR2 injection in Monkey B).

Multiple viral injections were made in each monkey along the penetration trajectory (in each grid hole). Viral injection of different constructs were separated by at least 2 mm from each other. Each injection was separated by 500 um from neighboring injection sites along the same trajectory (see inset in Figure 1b, Materials and Methods).

Cells are strongly modulated by light

Two to four weeks following viral injections we began recordings to characterize light-induced neural activity using custom-built optrodes (electrode glued to an optic fiber). We

characterized hSyn-ChR2(H134R) sites (monkeys J and B) with 473 nm laser and tested neural responses to continuous light (500-2000 ms, irradiance < 318 mW/mm^2) or short pulses (5-8 ms, 40-80 Hz, irradiance < 318 mW/mm^2). Figure 2a (first column) depicts the response of an example single unit from Monkey B to a 500 ms pulse of blue light. The unit significantly increased firing rate compared to baseline activity measured one second before stimulation ($p<0.001$, two tail paired t-test); Spike wave form (shown in Figure 2a on the top right) remained the same, indicating the response was not due to other cells or to an electrically-induced artifact. The observed reduction of firing rate during the stimulation interval was attributed to our laser instability and was correlated with the output, as measured with a power meter (Figure 2a, bottom right inset).

Similar neural modulations were observed in both monkeys and statistics were pooled for plotting purposes (statistics for each monkey in each injection site are given in Table. 1). Out of 184 recorded single units, 78% of the units significantly modulated their response (Figure 2b, leftmost column). The majority of units increased their responses (117 out of 144 modulated units), and the population was significantly up-modulated ($p<0.001$, two tail paired t-test). Out of the 144 modulated units, 126 were probed with a 500 ms continuous pulse of light and showed increase in firing rate. The average response of those units followed the same response as the unit shown in Figure 2a (Figure 2c top). Similar to previous studies (Han, Qian et al. 2009, Diester, Kaufman et al. 2011), we observed a light-induced artifact in the local field potential. A strong downward deflection to light onset and strong upward deflection when light was turned off were observed (Figure 2c, bottom), likely due to the Becquerel effect (Han 2012) . The mean response latency was 2.84 ms (Figure 2d, latencies

shown only up to 20 ms), with the majority of units responding within 1 ms. We found that 27 recorded units showed a reduction in firing rate, which could be due to secondary network effects or to spread from a neighboring viral injection of an inhibitory opsin.

Qualitatively similar responses were observed in hSyn-ChR2(E123A) and CamKII-ChR2(E123A) sites (Figure 2, second and third columns); 74% of recorded units modulated their response and responses were similar in shape, amplitude and latencies (Figure 2, second and third columns, Table. 1). ChR2(E123A) mutant was shown to evoke higher firing rates in vivo in rodents (Mattis, Tye et al. 2012) and indeed we found a small, but significant increase in the cumulative distribution of firing rate ratio ($p=0.03$, two sample, one tail Kolmogorov-Smirnov test).

We illuminated CAG-ArchT and hSyn-eNpHR3.0 sites with 532 nm laser by delivering continuous light (500-2000 ms). Firing rate was almost completely eliminated during the stimulation period and quickly recovered when the light was turned off (Figure 2a. single unit examples, fourth and fifth columns). The majority of units were strongly silenced (68% of all recorded units in ArchT sites and 52% in eNpHR3.0 sites, Table 1, Figure 2b, fourth and fifth columns). In both ArchT and eNpHR3.0 sites we observed a positive deflection of the LFP to light onset (Figure 2c, fourth and fifth columns) and a negative deflection when light was turned off.

Optical stimulation coupled to low current electrical stimulation increases probability of evoked saccades

In the work of Han et al. and Gertis et al. (Han, Qian et al. 2009, Gerits, Farivar et al. 2012), optical stimulation in FEF expressing ChR2 did not evoke saccades even though strong firing

rate changes were observed. Thus, it remained unclear whether such perturbations can contribute to the generation of a saccadic eye movement.

To test whether FEF optical stimulation contributes to generation of saccadic eye movements we probed FEF with both optical and electrical stimulation. While high current electrical stimulation reliably evokes saccades (see Figure 1c-d), low current electrical stimulation reduces the probability of evoking a saccade without significant changes to saccade amplitude or velocity (Bruce, Goldberg et al. 1985). Thus, one direct way to test whether optical stimulation contributes to generation of saccadic eye movement is to deliver at the same time low current electrical stimulation and optical stimulation and evaluate whether the probability of evoking saccades changes compared to low-current electrical stimulation alone.

While monkeys passively fixated a small dot, we lowered an optrode until eye movements could be evoked with low current electrical stimulation (< 50 μA), and single units were modulated with light. A stimulation pulse (optical or electrical) was considered successful in evoking a saccade if eye position changed more than 1.8 degrees (similar results were obtained using a higher threshold of 5 degrees, see Online Methods). For example, a 25 μA electrical stimulation in the ChR2 site in monkey B (at depth 1 mm relative to the first injection) evoked saccades in only 10/18 stimulation attempts (Figure 3a-c, top row). When the same electrical current was coupled to optical stimulation, a significant increase in number of saccades was observed ($p = 0.0003$, binomial test, Figure 3a-c middle row): 100% (17/17) of stimulations were successful in evoking a saccade. Optical stimulation without

electrical stimulation evoked one saccade which could be attributed to random eye movements of the monkey (Figure 3c, bottom row).

We define an experiment as a set of consecutive trials during which stimulation type (optical, electrical or both) were randomly interleaved, while stimulation parameters (current and irradiance) were held fixed. In each experiment we delivered on average 22±10 electrical stimulations, 21±9 combined electrical and optical stimulations, and 132±45 optical stimulations alone.

We repeated experiments at various depths along the penetration and considered each a separate site (Table 2). Within each site, we varied the level of electrical current, ranging from values that did not evoke any saccades (~10 μA) to values that reliably evoked saccades (~50-90 μA). The scatter plot in Figure 3d shows the percentage of evoked saccades in all recorded experiments (regardless of electrical current used) in all three monkeys. We found that 50/193 experiments resulted in a significant change in the probability of evoking saccades when optical stimulation was coupled to electrical stimulation ($p<0.01$, binomial test, see Materials and Methods). Significant increase was found in all three monkeys (see Table 2), and the average percentage of evoked saccades with optical and electrical stimulation was significantly higher than with electrical stimulation alone ($p<0.001$, $n=193$, paired right tail t-test).

In accord with previous studies, we found a monotonic increase in the probability of evoked saccades as the electrical current amplitude increased (Figure 3e data pooled across all hSyn sites in three monkeys, Figure 3f, data plotted for each viral injection separately). One may expect that the effect of optical stimulation will be more pronounced during experiments in

which the electrical stimulation was low and indeed we found that the increase in saccade probability during combined stimulation was larger for low electrical currents (Figure 3e, f). Furthermore, when the electrical current was set to the lowest level for which no saccades were evoked, the addition of optical stimulation still increased the probability and saccades were observed during combined stimulation (15 significant experiments, points along the Y axis in Figure 3d). Yet, in all these experiments, optical stimulation alone did not evoke any significant number of saccades (0.96 ± 1.55%, one-sided binomial test) compared to the number of saccades that would be expected by chance (due to random gaze shifts).

One concern with measuring behavior when using optical stimulation is that light leakage from the optic fiber might influence the monkey's behavior. Although we sealed the chamber and surrounds to prevent light leakage, the possibility remained that the observed eye movements were due to the monkey noticing light from the optic fiber and redirecting his gaze upwards. To control for this we ran several experiments in which an electrode was lowered to the FEF and an optic fiber was lowered into the chamber, but not the brain. We did not find any significant increase in saccade probability during these experiments (Figure 3g). Furthermore, the saccades evoked during combined stimulation typically followed the direction evoked by electrical stimulation alone (and not upwards, as would be expected from the location of the light source).

In two monkeys, saccades evoked by the combined stimulation started significantly earlier compared to saccades evoked with only electrical stimulation (Figure 4a, $p<0.01$, Kolmogorov-Smirnov test, Table. 2). We also found that stimulation effectiveness in evoking saccades depended on whether the fixation dot appeared on the screen, or was

extinguished just prior to stimulation (Figure 4b, see Materials and Methods). In both monkeys J & B we observed an increase in the efficacy of stimulation (either electrical or combined) when the fixation dot was not displayed (and the opposite case in monkey A).

Out of 193 stimulation experiments, we only found five that led to a significant change in saccade direction during combined optical and electrical stimulation compared to the direction observed during electrical alone evoked saccades (Figure 4c, $p<0.01$ non parametric multi-sample test for equal medians using CircStat). The average saccade deviation on those five experiments was 5.75 ± 2.89 degrees. Similarly, we only observed three experiments in which there was a significant change in saccade amplitude (Figure 4d, $p<0.01$, Mann-Whitney test), with a small amplitude difference (0.21±1.47 degrees).

Saccades evoked with optical stimulation alone

The results so far suggest that optical stimulation contributes to the generation of saccadic eye movement, but is not strong enough to initiate a movement without the coupled electrical stimulation. We found, however, for one specific site in monkey B (stretching between 2-2.5mm below the first injection site) that optical stimulation alone could consistently evoke saccades without electrical stimulation (Fig 5a-c, first row). In this example, the success rate of evoking a saccade with a 200 ms continuous light pulse was 76% (n=43 stimulation pulses). Saccades had similar onset latencies and amplitudes to those evoked by electrical stimulation at the same site (Figure 5a-c, second row).

We tested various stimulation trains and found that saccades could still be evoked with a shorter train (100 ms, 80 Hz, 8 ms pulse) (Figure 5a-c, third row). However, the efficiency of the stimulation decreased with lower pulse frequencies (Figure 5a-c, fourth row, Figure

5d), suggesting high frequency optical stimulation is a necessary condition for evoking a saccade. However, no optical stimulation evoked saccades were observed in a third monkey injected with second generation ChR2 which has improved channel kinetics and can be used to drive cells to higher firing rates (Figure 2). Stimulating at those sites did, however, evoke a similar increase in saccade probability when coupled to electrical microstimulation (Figure 3f).

On a consecutive day, we returned to the special site in monkey B and tested the effect of manipulating laser intensities on the percent of evoked saccades. We found that increasing the laser intensity led to a quick saturation in the success rate of evoking saccades (60%, Figure 5e) and that saccades could be evoked with as little as 82 mW/mm^2.

We also noticed that the direction of saccades evoked by optical stimulation significantly differed from that evoked by electrical stimulation by 16 degrees (Figure 5b, second and third rows; $p<0.001$, nonparametric multi-sample test for equal medians using CircStat). This difference may have been caused by the 0.5 mm offset between the electrode tip and the tip of the optic fiber, and indicates that two sub populations encoding different directions were stimulated.

Optical stimulation was successful in evoking saccades when delivered at depth 2-2.5 mm relative to the first injection, but not at other depths (even though they could be still evoked with electrical stimulation), or in neighboring grid hole penetrations. There are several possible explanations for this: 1) the effective site contained an especially high concentration of ChR2 expressing cells (see histological analysis below). 2) The effective site had some unique physiological properties, for example, lower spike thresholds. 3) The effective site

had some unique functional specificity, for example, a higher concentration of cells encoding the same saccade direction.

We reasoned that if the site contained neurons with lower spike threshold, then lower electrical currents should still evoke a saccade (compared to currents used in other sites). However, when we probed this site with varying electrical currents, we observed similar percentage of evoked saccades compared to other sites (Figure 5f), suggesting similar electrical thresholds were needed to evoke a behavior.

We found that electrically evoked saccades in the special site were significantly more accurate in their direction compared to all other sites ($p<0.01$ one side t-test, Figure 5g, data pooled across all hSyn sites from three monkeys, see Materials and Methods). Thus, a parsimonious explanation why saccades could be driven optically only at this site is that there was some functional specificity, such as a larger concentration of cells encoding the same saccade direction.

Inhibition of FEF using ArchT

We repeated the optical and electrical experiments in ArchT sites, to test the effects of optical inhibition on initiation of. Only sites in which reliable saccades could be evoked by electrical microstimulation and units were modulated by light were investigated.

An example experiment is presented in Figure 6a (data from monkey J). In this case, inhibition had no significant effect on the number of evoked saccades during combined stimulation compared to electrical stimulation alone. Although we observed a small number of saccades in the optical stimulation alone condition, those were not oriented towards a consistent direction and could be considered random eye movements that happened to align

with stimulation onset (Figure 6a, bottom row). We also observed cases in which combined electrical and optical stimulation resulted in a significant reduction in the number of evoked saccades (Figure 6b, data from monkey B) compared to the number of saccades evoked with electrical stimulation alone. Although we observed a small number of saccades following the optical stimulation (n=12/203), they were not oriented towards a consistent direction (Figure 6b, bottom row).

Overall, out of 72 stimulation experiments (in 10 sites of two monkeys, see Table 2, see population average in Figure 6c), only 12 were found to significantly modulate the number of evoked saccades (Figure 6d, $p<0.01$, binomial test), but the overall population was not significantly modulated (Figure 6d, $p=0.69$, paired two-tail t-test) and some of the significant experiments led to a decrease while some led to an increase in saccade probability. No significant change in saccade direction was found during combined electrical and optical inhibition compared to electrical stimulation alone (Figure 6e, $p=0.05$, paired two tail t-test) and only one experiment led to a significant increase in saccade amplitude. Saccade latencies were also not statistically different ($p= 0.23$, Kolmogorov-Smirnov test, Figure 6f). These results suggest that local inhibition of FEF does not lead to saccade initiation and that local inhibition during electrical stimulation in most cases is not strong enough to overcome the electrical stimulation.

fMRI activity during electrical and optical stimulation in the FEF

One explanation previously proposed to explain the lack of evoked movements following optogenetic stimulation in the macaque is that the volume of stimulated tissue is much

smaller compared to that evoked with electrical stimulation (Han, Qian et al. 2009, Diester, Kaufman et al. 2011). Previous studies suggested that optogenetics can be combined with fMRI to measure the evoked activity across the brain (Lee, Durand et al. 2010, Desai, Kahn et al. 2011, Gerits, Farivar et al. 2012), but have not directly compared how the pattern of activation induced by electrical stimulating differs from that induced by optical stimulation. Here, we measured fMRI activity while simultaneously applying electrical, optical, or combined stimulation to the FEF to assess the spread of activity.

An optrode was lowered to FEF until saccades could be evoked with low current electrical microstimulation (< 50 μA) and single units were modulated by light. The monkey was transported to the scanner and scanned while it performed a fixation task. We delivered pulses of optical stimulation, electrical stimulation, or both in a block design to directly assess the contribution of each type of stimulation (Figure 7a).

The average time course of a small ROI centered close to the optrode tip is shown in Figure 7a. We found that the fMRI signal increased significantly during electrical stimulation and also during combined stimulation, but not during optical stimulation alone (Figure 7b,c). The smallest p-value in the ROI was above 0.01 for the contrast Optical-Rest. This result was reproducible across multiple days in different sites, with different configurations: various optical stimulation trains, thicker optical fibers and two optrode simultaneous stimulation in neighboring sites. Furthermore, no activation during optical stimulation was observed in Monkey B's special site in which optical stimulation did evoke saccades (Figure 7a, top).

Histological analysis

At the end of the experimental period monkey B was perfused and standard immunohistochemistry procedures were performed to validate opsin expression. We observed strong expression at all three injection sites (wide field fluorescence, Figure 8a-b, no antibodies were used to amplify YFP). We labelled cells with NeuN (pan-neuronal marker), GFAP (astrocytes marker), CamKII (excitatory maker), and PV (inhibitory marker). Most YFP expressing cells were found within 2 mm of the injection site (several examples in Figure 8c) and expressed NeuN as well. No expression was found in GFAP positive cells. We counted about 100 cells that expressed CamKII and YFP, but only one cell was found to express YFP and PV (PV is known to label only a subset of inhibitory neurons, which may explain the low count number). We observed YFP expression mainly in layers II-III and V-VI (assessed from DAPI staining, Figure 8d). Tissue damage was observed in superficial regions from guide tube penetration as well as in deep tissue from repetitive optrode insertion.

To analyze the extent of the viral expression quantitatively, and to assess whether there was a significant increase in opsin expression at the unique ChR2 site in which optical stimulation evoked saccades, a custom software was developed to register images across different modalities (MRI, frozen tissue block, wide-field fluorescence, high magnification Z-stacks, see Figure 9a). This enabled us to represent labeled cells relative to the MRI and the non-vertical injection penetration track (see injection reconstruction in Figure 9b; note that depth along the penetration does not necessarily correspond to increasing cortical layers).

We manually annotated 3143 YFP expressing cells (small example tissue shown in Figure 9c). The coordinate of each annotated cell (represented schematically as a green dot in Figure 9b), was represented in 3D cylindrical coordinates relative to the first injection site (white line, Figure 9b). A histogram of YFP-expressing cells, relative to the 3D injection path, as a function of depth and radial distance is shown in Figure 9d. The marginal distribution as a function of radial distance was bi-modal and contained two peaks at 1.3 mm and 2.4 mm. We attributed the first peak to the ChR2 injection and the second peak to the neighboring ArchT and eNpHR3.0 injections. The two peaks were separated at a valley that reached its minimum at 1.9 mm (this was also true when the distribution was normalized by considering the increase in circumference, see gray curve, Figure 9d). We therefore plotted the marginal distribution of ChR2 as a function of depth for only YFP expressing cells within 2 mm radius (9d, right plot). We found that the peak expression levels were at depth 2.7 mm. No significant increase in YFP labelled cells was found between 2-2.5 mm, corresponding to the special site in which saccades were observed with optical stimulation ($p>0.5$, bootstrapping, see red box in Figure 9d).

Discussion

In this study we injected several optogenetic constructs into the macaque FEF to examine the effects of optical stimulation in evoking saccadic eye movements. On average, 74% of the single units recorded in injected regions significantly modulated their firing rate during optical stimulation. This number is slightly higher than previously reported numbers (40-50%) (Diester, Kaufman et al. 2011), and may be related to larger volumes we injected (with similar titers) or to larger area covered with lowered electrode impedance.

Recently, three studies emerged with reports about optogenetic manipulation in macaques leading to observed behavioral changes. Gertis et al. (Gerits, Farivar et al. 2012) reported a reduction in response latencies when monkeys performed a visually guided saccade task during ChR2 stimulation in the FEF, but no optically-evoked saccades. Cavanaugh et al. (Cavanaugh, Monosov et al. 2012) found that inactivation of the superior colliculus leads to a small shift in saccade endpoint and a slight increase in saccade latency. Jazayeri et al. (Jazayeri, Lindbloom-Brown et al. 2012) trained animals to respond to flashes of light with an eye movement and reported consistent saccades to the same location following ChR2 stimulation in primary visual cortex, suggesting stimulation evoked the perception of a phosphene. While these studies are important in providing evidence that optogenetic perturbations can lead to behavioral changes, they do not address the issue of how effective optogenetic perturbations are in comparison to the most widely used method of perturbing behavior in monkeys, electrical stimulation. They also do not address how optogenetic and electrical perturbations interact, a question important for clarifying whether the two types of perturbations act upon common circuits.

By examining the effects of optogenetic constructs side by side with electrical microstimulation, we show that ChR2 optical stimulation has a similar effect as low current (or low frequency) electrical stimulation. In ChR2-injected regions, optical stimulation did not evoke a saccade in most cases, despite strong neural modulation. The question whether these neural perturbations contribute in any way to initiation of a saccade was answered by coupling the optical stimulation to low current electrical stimulation. A significant increase in the number of evoked saccades was observed, essentially increasing the efficacy of

electrical stimulation, suggesting optical stimulation contributes to network activity that can evoke a movement, but without the low electrical current injection, the effects remain sub-threshold and are not strong enough to initiate a movement. In particular, when electrical current was so low such that it alone did not evoke any saccades, the addition of optical stimulation did lead to evoked saccades. This result rules out previously hypothesized idea that optical stimulation modulates cells that do not participate in generating behavior or that stimulation activates neurons not in the right way needed to generate a movement (Diester, Kaufman et al. 2011). Our results suggest that optical and electrical stimulation work on a functionally overlapping population of cells because the behavioral effects are additive.

In one monkey we found that optical stimulation alone reliably evoked saccades. Modulating the optical stimulation train parameters revealed that higher stimulation frequencies were more effective in driving saccades and that movements could be evoked with as little as 82 mW/mm^2. This suggested that ChR2 with improved channel kinetics which allow higher stimulation frequencies may be more effective in driving behavior. However, optical stimulation in a third monkey injected with second generation ChR2 (Gunaydin, Yizhar et al. 2010, Mattis, Tye et al. 2012) did not evoke saccades, nor did a construct targeting pyramidal neurons (CamKII-ChR2:E123A). It is important to note that neurons in both regions injected with these two variants showed strong modulation (similar number of modulated cells to those observed in the two other monkeys), and that an increase in saccade probability was observed when optical stimulation was coupled to low current electrical stimulation. Thus, second generation ChR2, although capable of driving cells to higher frequencies, failed to evoke a movement in the tested sites (we do not rule out the possibility

that ChETA variants may work in sites that may have some special characteristics, like the one we observed in monkey B).

The level of electrical current needed to evoke saccades did not differ significantly in the special site of monkey B, compared to nearby sites in which optical stimulation was not effective, suggesting it was not due to some basic physiological difference such as a lower spike threshold. We propose two plausible explanations why saccades were evoked in this site. One is that the site included a larger fraction of cells encoding the same saccade direction, rendering focal optical stimulation more effective. This was supported by our analysis showing that saccades evoked in that region were the most accurate ones. Another possibility is that the region had a significant increase in viral expression. Our histological analysis did not show a significant increase in expression at the special site in which saccades were evoked with optical stimulation. However, we did find a small peak of YFP expressing cells at depth 2.7 mm, and cannot rule out completely that the mismatch is due to small errors caused by non-linear tissue deformation (e.g., caused by repetitive fiber insertion in following experiments) .

Previous studies have shown that combined fMRI and electrical stimulation can reveal regions connected to the site of stimulation (Tolias, Sultan et al. 2005, Moeller, Freiwald et al. 2008, Logothetis, Augath et al. 2010). Experiments with rodents using combined fMRI and optical stimulation (ofmri) suggested ChR2 stimulation can be used to trace anatomical connections (Lee, Durand et al. 2010, Desai, Kahn et al. 2011). In contrast to a recent report by Gertis et al. (Gerits, Farivar et al. 2012) who stimulated NHP with ChR2 in FEF, we found no significant BOLD activation elicited by ChR2 stimulation close to the optrode tip (but

strong activation during interleaved electrical stimulation blocks). We made numerous attempts to replicate Gertis's result, including using various second generation ChR2 constructs, different stimulation parameters, thicker fibers diameters, and simultaneously stimulating two adjacent sites. Thus, one possible explanation why Gertis et al. observed significant activation might be related to their use of an active saccade task in the scanner, compared to the fixation paradigm employed in this study.

The correlation between the large behavioral response evoked by electrical stimulation and the strong fMRI activity observed at the stimulation site during electrical stimulation suggests that a critical difference between electrical and optogenetic stimulation may be the volume of stimulated tissue. However, optical stimulation at the effective site in Monkey B (Figure 7), which evoked saccades, did not lead to a significant BOLD increase, suggesting motor movements can be evoked with small stimulated volumes (that may not be visible at 1 mm^3 fMRI scanning resolution).

Low current electrical stimulation in the FEF is sufficient to evoke saccades and induce strong fMRI activity close to the tip, and presumably activates a distributed sparse network of cells (Histed, Bonin et al. 2009). It is possible that that these cells are highly functionally correlated, and optogenetic stimulation fails to stimulate similarly functionally homogeneous networks. If this is the case, increasing the reliability of optogenetic stimulation in evoking motor movements may not necessarily require engineering tools with larger expression volumes, or light that penetrates deeper (e.g., C1V1, see (Yizhar, Fenno et al. 2011)), but rather targeting sparse functional correlated networks.

While optogenetics has many advantages over electrical stimulation, our experiments suggest that the classical method of evoking motor movement with direct current injection is still more effective compared to existing optogenetic constructs. Optical stimulation led in most cases to a sub-threshold activity which was not sufficient to initiate a movement. Yet, such perturbation can be used to modulate ongoing motor behavior, such as latency or direction (Cavanaugh, Monosov et al. 2012, Gerits, Farivar et al. 2012). Optogenetics has revolutionized neuroscience, making it possible to test hypotheses about how local circuit perturbations affect or generate behavior. Our demonstration that ChR2 stimulation increases the efficacy of low current electrical stimulation and that ChR2 stimulation alone can evoke saccades is an important step in establishing the applicability of the technique for dissecting behaviorally relevant neural circuits in NHPs and paves the way for further investigation to discover the necessary and sufficient conditions required for evoking motor responses.

Figures

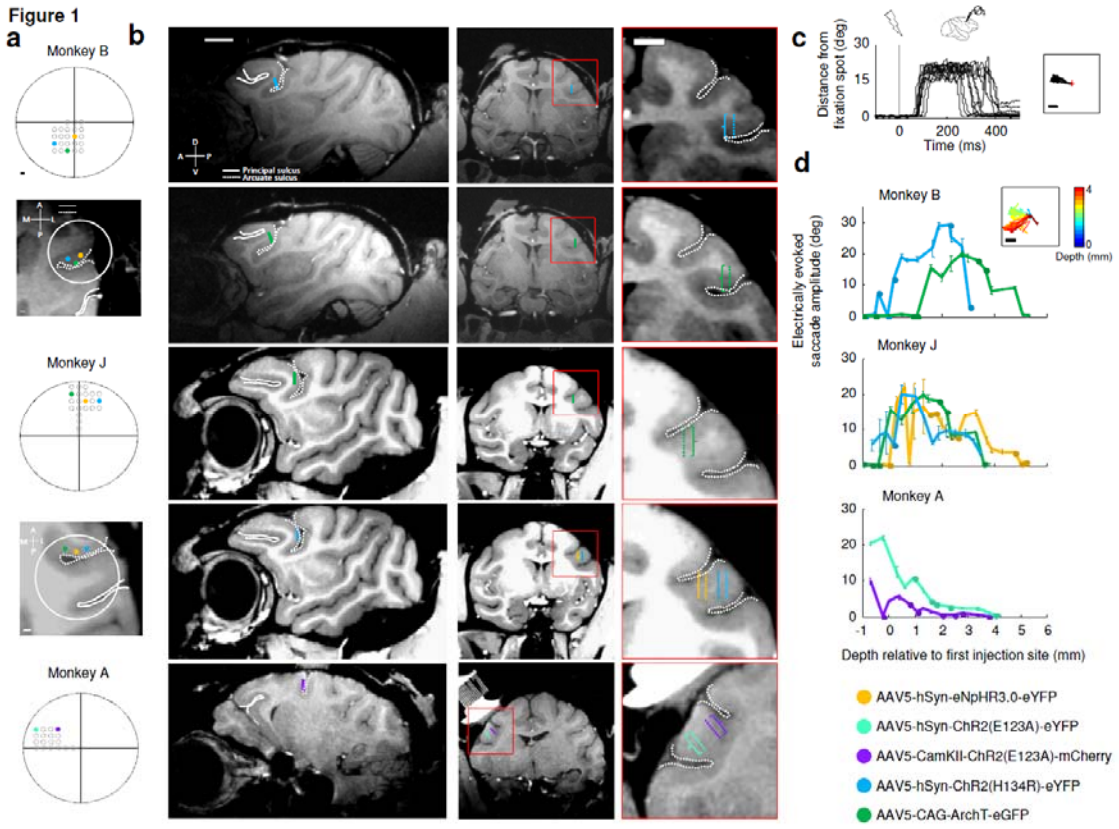

Figure 1. FEF injection sites and electrically evoked saccades. (**a**) Top view of the grids used to inject viral vectors and to record neural signals. MRI reconstruction aligned to chamber coordinates is shown below for monkeys B and J. Scale bar: 1 mm. (**b**) MRI reconstructions of injection sites (sagittal and coronal views); eNpHR3.0 injection in monkey B not shown due to space limitations. Cross sections are aligned to show the full injection trajectory. Scale bar: 10 mm. Zoom inset: injection sites (each is represented by a small dot). Scale bar: 5 mm. (**c**) Example of electrically evoked saccades in the ChR2 site in monkey B at depth 0.5 mm relative to the first injection site (distance from fixation spot on the left, eye trace on the right). Eye trace is aligned to electrical microstimulation (delivered at time 0). (**d**) Average

saccade amplitude evoked by electrical microstimulation at various depths in all injection sites (mean ± SEM). Small inset on top plot shows all evoked saccades as a function of depth in the ChR2 site in monkey B prior to viral injection (depth is color coded).

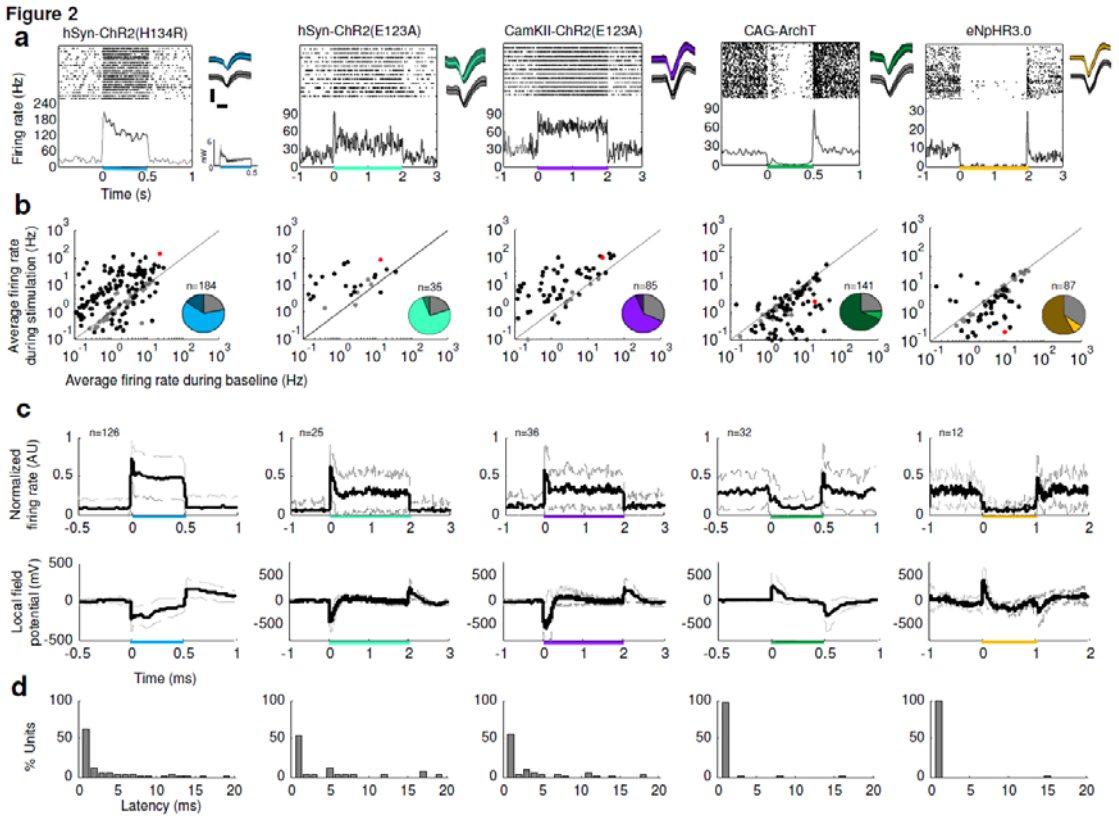

Figure 2. Electrophysiological characterization of light-induced modulation of neural activity in the FEF. (**a**) Peri-stimulus time histogram for a single unit recorded from each injection site and the corresponding raster plot (shown above). Stimulation interval is denoted by the colored bar. Traces on right of each plot shows the average spike wave (mean ± std) form during stimulation (in color) and before and after stimulation (in gray). Scale bar: 250μV and 250 μs. Bottom right small inset: measured laser output intensity. (**b**) Scatter plot of average firing rate during the stimulated interval compared to baseline activity across all

recorded cells in all injection sites (data pooled across monkeys). Monkeys were required to maintain fixation on a small dot. Juice rewards were delivered every 2-4 seconds if the monkey did not break fixation. Black dots denote significant modulation compared to baseline ($p<0.05$, two tail paired t-test), gray dots denote non-significant modulation, example cell shown in (a) is highlighted in red. Pie charts denote the fraction of non-modulated units (gray), up-modulated units (bright color) and down-modulated units (dark color) (**c**) Average unit responses to continuous light (mean ± std; top: normalized firing rate; bottom: local field potential). Average is over modulated units only (up modulated for ChR2, and down-modulated for ArchT and eNpHR3.0). (**d**) Histogram of response latencies.

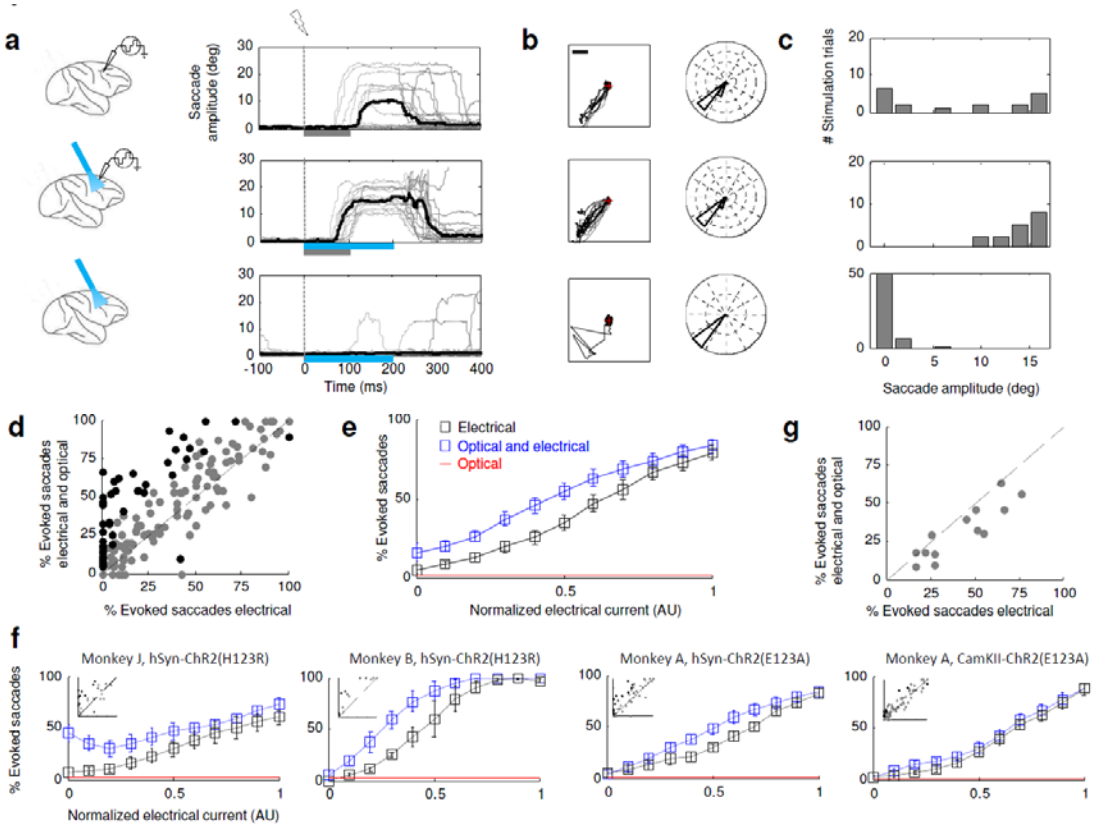

Figure 3. Optical and electrical stimulation in ChR2 sites. (**a**) Schematics of three different stimulation configurations: electrical (top), electrical and optical (middle), optical (bottom); right panels show eye position traces from an example ChR2 site in monkey B elicited by the three stimulation configurations (relative to onset of stimulation at at=0). Solid black curve represents the median trace of all trials, including stimulation trials that did not evoke saccades (note it does not represent the average amplitude of evoked saccades). Configuration 1: electrical stimulation, denoted as a gray bar below plot (100 ms, 300 Hz, 0.25 μs biphasic, 25 μA); Configuration 2: coupled optical stimulation (200 ms continuous pulse, 190 mW/mm^2, denoted as blue bar below plot) and electrical stimulation (same parameters as Configuration 1); Configuration 3: optical stimulation (200 ms continuous pulse, 190 mW/mm^2). (**b**) Left: eye position for all stimulation trials; scale bar: 5 degrees. Right: normalized polar histogram for trials with evoked saccades. (**c**) Histogram of average saccade amplitude following stimulation (measured at 150-200 ms relative to stimulation onset). (**d**) Scatter plot of the percentage of evoked saccades for combined optical and electrical stimulation vs. electrical stimulation alone. Each dot represents a single experiment (multiple stimulations) performed with a fixed electrical current and fixed irradiance. Data shown for all four ChR2 sites in three monkeys. Black dots indicate experiments with a significant difference ($p<0.01$, binomial test, see Online Methods); gray dots, not significant. (**e**) Percentage of successfully evoked saccades by electrical stimulation (black curve), combined optical and electrical stimulation (blue curve) and optical stimulation alone (red curve). Data pooled across three monkeys and three injection sites (hSyn promoter). Electrical currents were normalized by the minimal and maximal currents used in each site

(see Online Methods). Error bars denote S.E.M. (**f**) Similar to (d) and (e), but data is plotted for each injection site separately. (**g**) Similar to (d), but for control sessions in which the optic fiber was outside the brain.

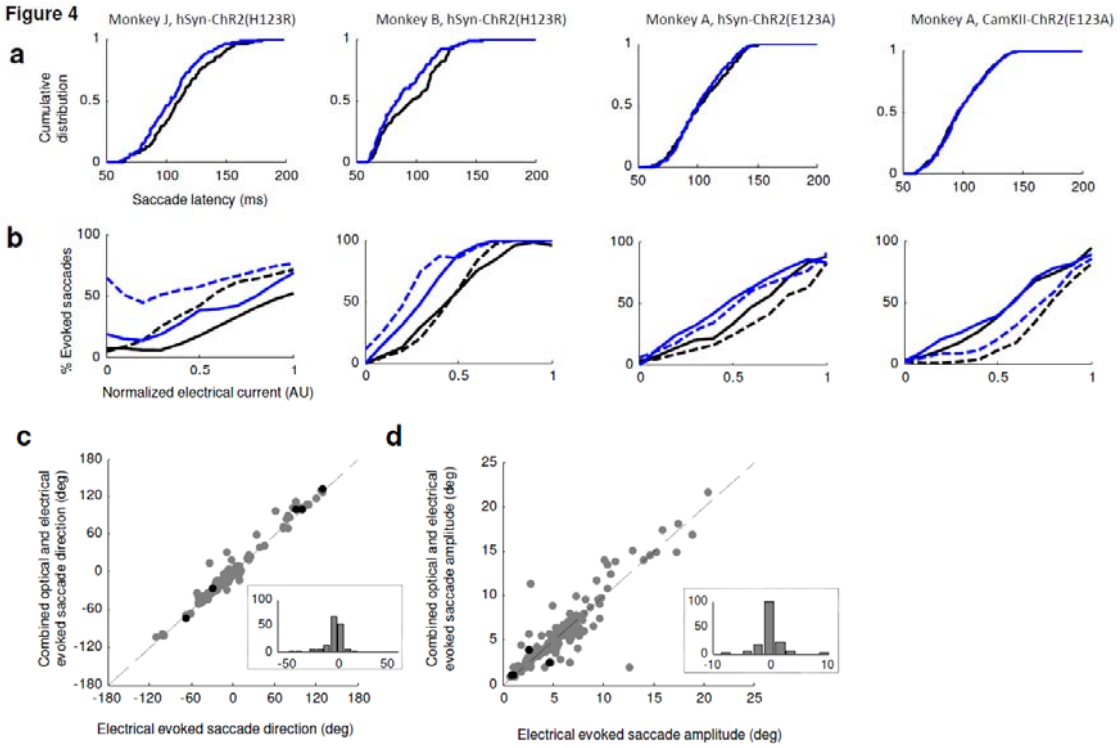

Figure 4. Optical modulation of saccade parameters. (**a**) Cumulative distribution of saccade latencies (data shown for each ChR2 injection site). Blue curve: combined electrical and optical stimulation; Black curve: electrical stimulation. (**b**) Effectiveness of stimulation when the fixation dot was on the screen (solid curves), or when it was extinguished just prior to stimulation (dotted curves). (**c**) Scatter plot of mean saccade direction for combined optical and electrical stimulation vs. electrical stimulation alone. Black dots indicate experiments with a significant difference in direction ($p<0.01$, nonparametric test for equal medians); gray dots: not significant. Small inset shows the difference in saccade direction across all recorded

experiments. (**d**) Scatter plot of mean saccade amplitude. Conventions same as in (c). Black dots indicate significant change in amplitude ($p<0.01$, Mann-Whitney test).

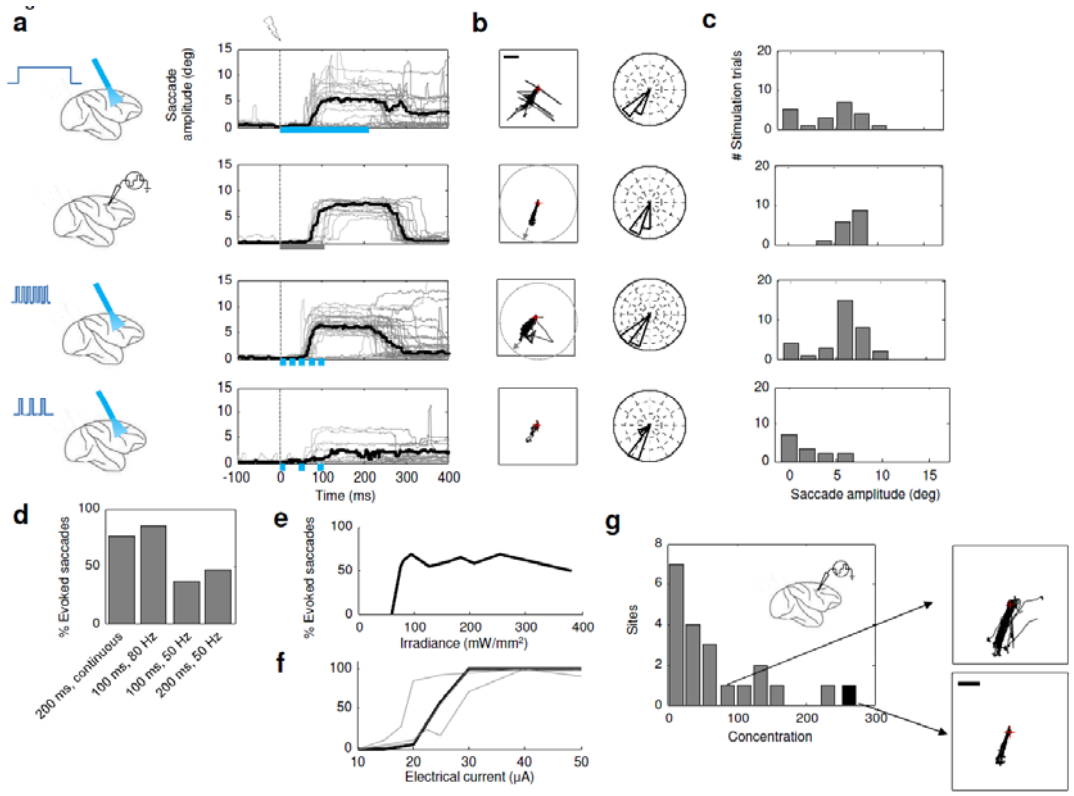

Figure 5. Saccades evoked with ChR2 Optical stimulation. (**a-c**) Conventions same as in Figure 3. First row, Optical stimulation with a 200 ms continuous pulse. Second row, Electrical stimulation (100 ms, 300 Hz, 0.25 μs biphasic, 50 μA). Third row, Optical stimulation (100 ms, 80 Hz, 8 ms pulse). Fourth row, Optical stimulation (100 ms, 50 Hz, 8 ms pulse). Scale bar: 5 degrees. (**d**) Percent evoked saccades for four different optical stimulation trains. (**e**) Percent evoked saccades as a function of optical stimulation laser intensity. (**f**) Percent evoked saccades as a function of electrical current. The special site in which saccades were evoked with optical stimulation is shown in black. Three other sites from monkey B are shown in gray. (**g**) Histogram of von Mises concentration parameter of

electrically-evoked saccades across all recorded sessions (gray bars) and the concentration parameter (for electrically evoked saccades) found at the special site from in which optical stimulation alone evoked saccade (black bar). Higher concentration values correspond to smaller saccade angular variance (more accurate saccades). Upper right inset shows eye movements with a low concentration parameter (κ=76); bottom right inset shows eye movements for the highest concentration, found at the site in which optical stimulation evoked saccades (κ=263). Scale bar: 5 degrees.

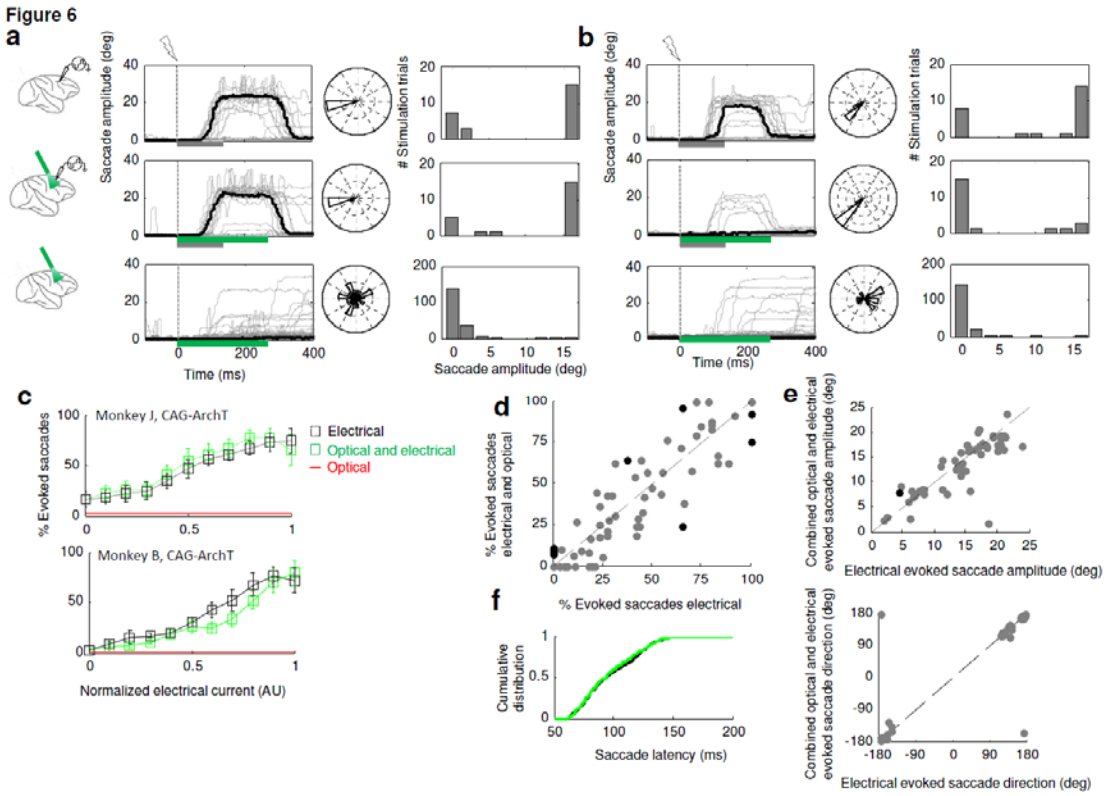

Figure 6. Optical and electrical stimulation in ArchT sites. Conventions same as Figure 3. (**a**) Representative stimulation experiment in Monkey J. Top row: electrical stimulation (100 ms, 300 Hz, 0.25 μs biphasic, 70 μA), middle row: combined stimulation (100 ms, 300 Hz, 0.25 μs biphasic, 70 μA + 200 ms continuous optical pulse, 190 mW/mm^2), bottom row:

optical stimulation (200 ms continuous optical pulse, 190 mW/mm^2). (**b**) Representative stimulation experiment in Monkey B. Electrical stimulation (100 ms, 300 Hz, 0.25 μs biphasic, 25 μA), optical stimulation (200 ms continuous optical pulse, 190 mW/mm^2). (**c**) Percentage of successfully evoked saccades by electrical stimulation (black curve), combined optical and electrical stimulation (green curve), and optical stimulation alone (red curve). Data shown for each monkey separately. (**d**) Scatter plot of the percentage of evoked saccades for combined optical and electrical stimulation vs. electrical stimulation alone. Data pooled from both monkeys. (**e**) Average saccade amplitude and direction during optical and combined stimulation. (**f**) Cumulative distribution of saccade latencies for electrical stimulation (black trace), and combined electrical and optical stimulation (green).

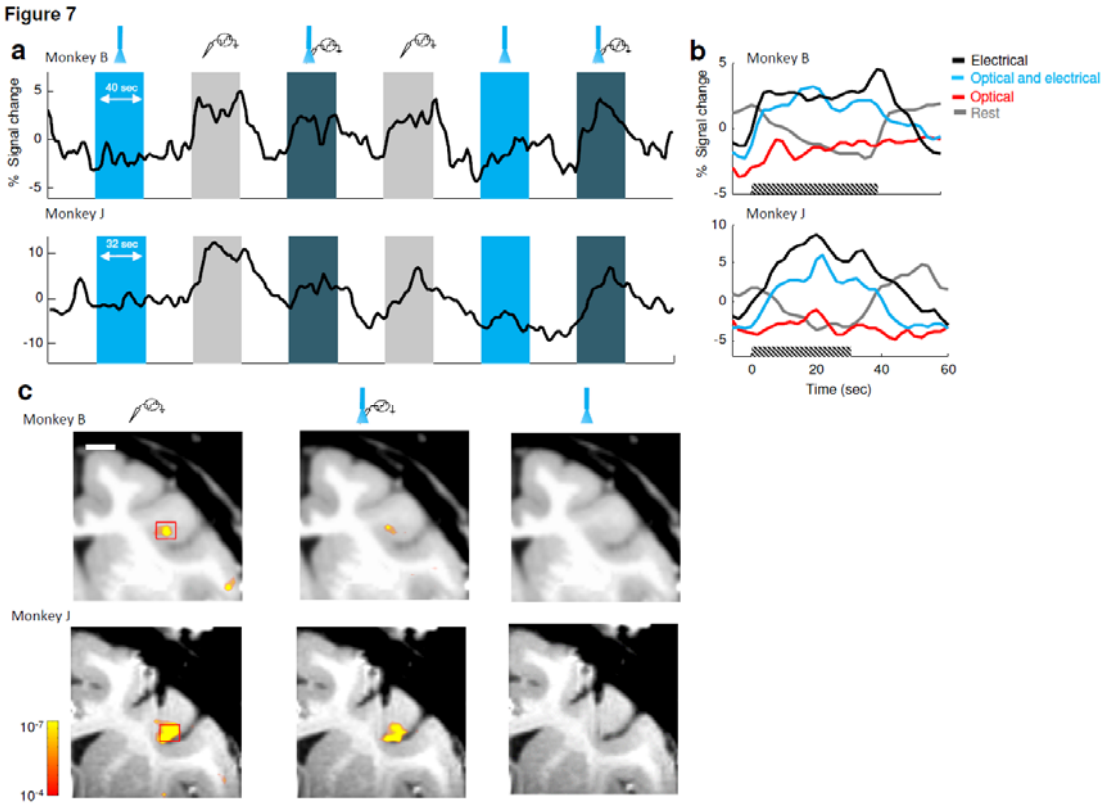

Figure 7. fMRI activity close to the optrode tip during electrical and optical stimulation. (**a**) Average fMRI response measured during a block design experiment with conditions: rest (white background), optical stimulation (bright blue background, 1 Hz train for 900 ms; pulses: 80 Hz, 8 ms, 82 mW/mm^2), electrical stimulation (gray background, 1 Hz train for 200 ms; pulses: 300 Hz, 150 µs biphasic, 50 µA), and combined electrical and optical stimulation (dark blue background). Responses were averaged in a small ROI close to the electrode tip (shown in (c)). Scale bar: 5 mm. (**b**) fMRI peristimulus time course (aligned to conditions onsets). (**c**) Coronal section aligned to stereotactic coordinates (AP = 26) showing significant activity during electrical stimulation blocks (left), combined stimulation (middle), and optical stimulation alone (right).

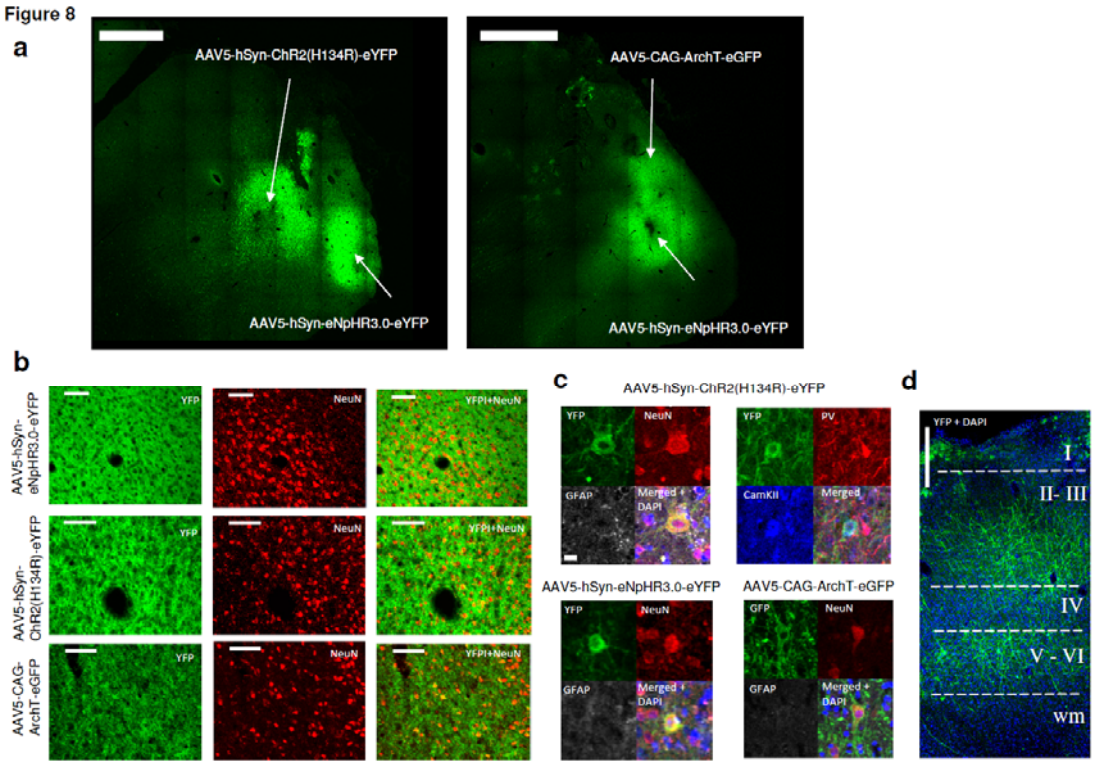

Figure 8. Injection sites and immunohistochemistry in Monkey B. (**a**) Wide field fluorescence; scale bar 2 mm. (**b**) Expression close to the injection site. Left YFP, middle: NeuN, right: YFP and NeuN. Scale bar: 500 um. (c) Immunohistochemistry of four example cells taken from ChR2, Arch and eNphR3.0 Sites. Opsin fluorophore (YFP/GFP, green), pan neuronal maker (NeuN, red), cell nucleus (DAPI, blue), astroglia (GFAP, white), excitatory marker (CamKII, blue). Scale bar 10 μm. (**d**) YFP expression pattern across cortical layers (DAPI in blue).

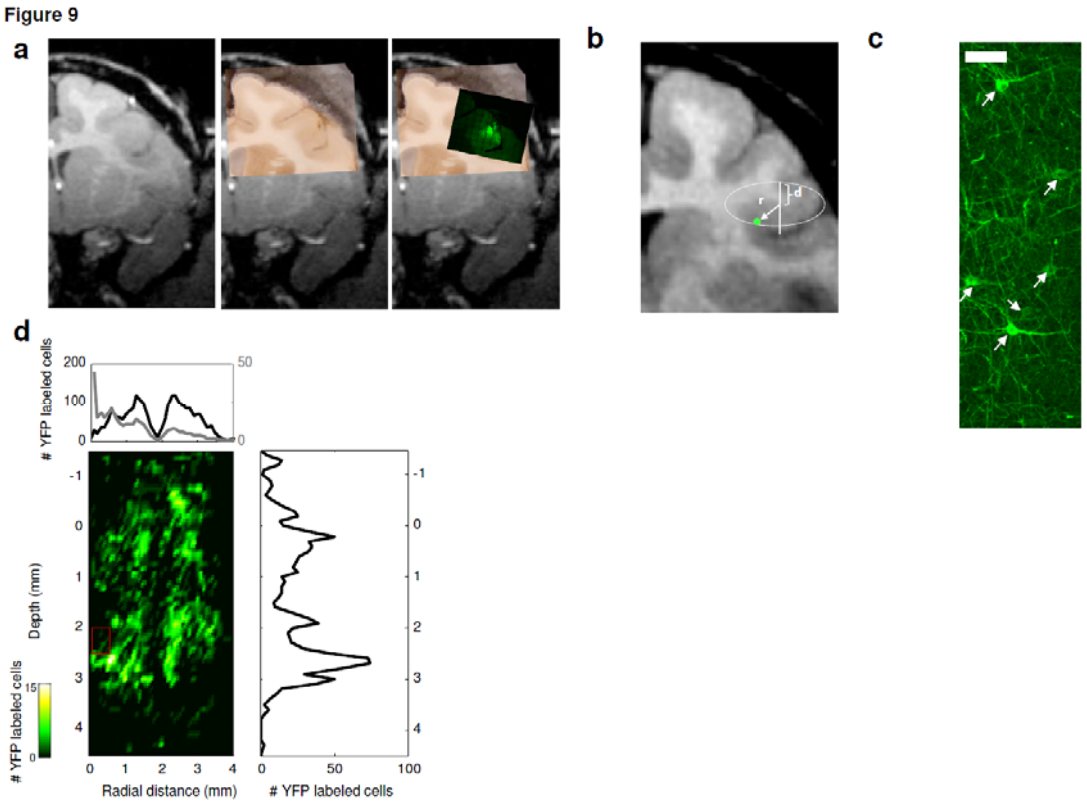

Figure 9. Quantitative histology of ChR2 expressing cells in monkey B. (**a**) Coronal MRI section of the right hemisphere showing a section of the FEF (left, scale bar: 3.5 mm). The same coronal slice overlaid with a registered photograph of the frozen tissue block (middle)

and the same slice overlaid with registered wide field YFP fluorescence (right). (**b**) Schematic of coordinate system used to represent the location of YFP expressing cells. Injection trajectory (white line), overlaid on the reconstructed MRI scan. YFP expressing cell (green dot) is represented in 3D cylindrical coordinates as a function of depth (relative to the first injection site), radial distance and angle. (**c**) Example of annotated cells in a small patch of ChR2 expressing tissue; scale bar 20 μm. (**d**) Histogram of YFP expressing cells as a function of radial distance from the injection trajectory and depth (relative to first injection site). The special site in which optical stimulation evoked saccades is highlighted in red. Top: marginal distribution of YFP expressing cells as a function of radial distance (black), and the distribution normalized to the radial circumference (gray). Right: marginal distribution as a function of depth (at radial distance smaller than 2mm).

List of tables

Opsin	Monkey	# Injections	Stereotactic coordinate of first injection (AP,ML,DV)	Stereotactic coordinate of last injection (AP,ML,DV)	# Units recorded	# Significantly modulated units	% Up modulated (out of # sig units)	% Down Modulated	% Units recorded from injection grid hole
AAV5-hSyn-ChR2(H134R)-eYFP	B	8	[28.02,15.00,22.54]	[26.08,15.90,19.42]	35	29 (82%)	25 (86%)	4 (14%)	100%
AAV5-hSyn-ChR2(H134R)-eYFP	J	9	[26.54,17.48,24.82]	[25.50,17.58,21.19]	149	115 (77%)	92 (80%)	23 (20%)	60%
AAV5-CAG-ArchT-eGFP	B	9	[27.81,17.43,23.81]	[25.59,17.91,20.24]	33	29 (87%)	0 (0%)	29 (100%)	63%
AAV5-CAG-ArchT-eGFP	J	9	[26.67,13.67,24.82]	[25.52,13.73,20.80]	108	78 (72%)	11 (15%)	67 (85%)	95%
AAV5-hSyn-eNpHR3.0-eYFP	J	9	[26.07,15.42,24.90]	[25.06,15.72,21.23]	37	27 (72%)	4 (15%)	23 (85%)	100%
AAV5-hSyn-eNpHR3.0-eYFP	B	9	[28.66,18.49,21.25]	[26.50,18.90,17.80]	65	43 (66%)	12 (28%)	31 (72%)	100%
AAV5-hSyn-ChR2(E123A)-eYFP	A	8	[25.57,-18.66,25.04]	[24.52,-16.40,22.30]	35	28 (80%)	26 (92%)	2 (8%)	50%
AAV5-CamKII-ChR2(E123A)-mCherry	A	8	[23.37,-16.48,26.97]	[23.36,-14.32,24.26]	85	58 (68%)	53 (91%)	5 (9%)	100%

Table 1: List of injection sites, their coordinates and the number of single units recorded.

Opsin	Monkey	Number of sites probed with electrical & optical stimulation	Number of stimulation experiments (at various currents)	Number of experiments showing significant modulation	Latency (electrical)	Latency (electrical&optical)	Latency p-value
AAV5-hSyn-ChR2(H134R)-eYFP	B	3	20	7 (35%)	98.36 ± 24.60	91.13 ± 23.67	0.0017
AAV5-hSyn-ChR2(H134R)-eYFP	J	5	27	13 (48%)	115.38 ± 29.52	106.88 ± 24.26	0.0038
AAV5-hSyn-ChR2(E123A)-eYFP	A	9	58	16 (28%)	106.84 ± 31.72	104.11 ± 20.77	0.22935
AAV5-CamKII-ChR2(E123A)-mCherry	A	13	88	14 (16%)	100.32 ± 21.26	100.90 ± 21.10	0.8334
AAV5-CAG-ArchT-eGFP	B	5	35	5 (14%)	103.14 ± 26.24	103.50 ± 27.35	0.48456
AAV5-CAG-ArchT-eGFP	J	5	37	7 (19%)	97.50 ± 25.42	95.71 ± 22.14	0.29592

Table 2: List of the number of stimulation experiments, latencies of evoked saccades and p-value indicating whether the latency distribution during combined stimulation significantly

differed compared to latencies of saccades evoked with electrical stimulation alone (Kolmogorov-Smirnov test).

Chapter 4: Conclusions and Outlook

Three topics have been addressed in this thesis: MR-guided electrophysiology, face-detection in face-selective regions and application of optogenetics to perturbing activity in NHPs. In this last chapter, I comment on their possible impact, speculate on future directions, and present preliminary unpublished data from attempts to apply optogenetics in the face patch system.

MR-Guided Electrophysiology

Planner, the MR-guided electrophysiology planning software I developed, was initially intended to assist me in my own experiments. However, it quickly became apparent that I wasn't the only one facing the problems associated with deep brain targeting and that the larger community would also benefit from such a tool. In the past two years, over 30 labs around the world have downloaded and experimented with *Planner*. In our lab, *Planner* has transformed the workflow of designing and carrying out experiments. It has significantly reduced the expertise needed to target a single or even multiple brain region simultaneously, reduced multiple iterations needed to target a region and their associated costs, as well as the time required to design and execute experiments. Due to the overall success and interest, I continued to develop and continuously added new features. For example, *Planner* now has features to enable the targeting of multiple brain regions using a single grid by modelling the direction of each grid-hole independently of all others. *Planner* can automatically generate CAD models of grids which can be easily fabricated using existing 3D printers (see Figure 1). Support for combining histology and MRI was added, to enable easy 3D registration between anatomical tracers and functional scans.

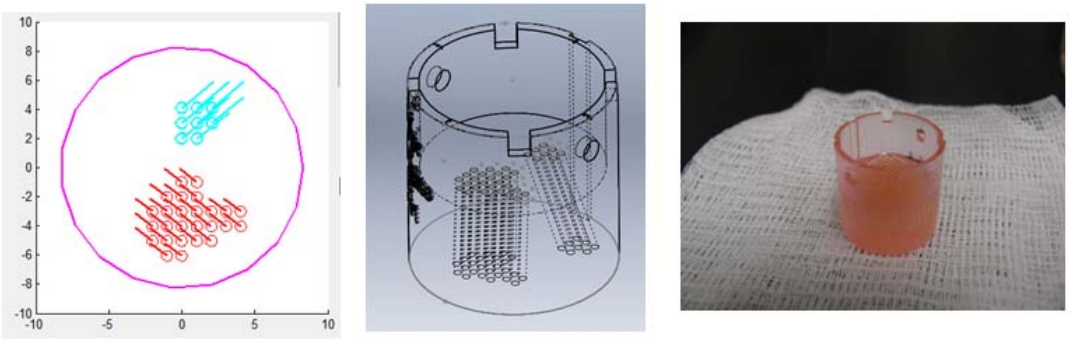

Figure 1. Targeting two brain structures from a single chamber. Left: top view of a generic grid containing two group of holes, each pointing to a different 3D direction. Middle: automatically generated CAD model of the the grid. Right: printed model.

Planner was designed to address two problems: chamber placement and grid design. The former still requires some amount of engineering know-how due to the variability in stereotactic frames and lack of publicly available information about the mechanical aspects of them. It is also apparent that existing NHP stereotactic frames are simply not built to achieve our desired level of accuracy. The mechanical stability is rather poor, especially compared to existing rodent stereotactic frames, which not only have better construction, but also digital read out of the individual joints. Overall, it seems that a better solution for chamber placement still awaits. Recent advances in 3D sensing, such as the development of Kinect, will allow low-cost real-time chamber placement by tracking the 3D shape of the skull/implant and the chamber, similar to the costly BrainSight system by Rogue Research. Preliminary results with the developer version of Kinect demonstrated that the existing image and depth resolutions are simply not sufficient to achieve the desired millimeter resolution

needed for accurate chamber placement. However, it is quite likely the future version with HD support will be suitable for this task.

Face Processing

Our initial observation that faces with the same contours, but different local contrasts lead to significant differences in firing rate for face-selective cells suggest that we managed to tap into a critical mechanism used by these cells. It brings to question some fundamental assumptions about what type of information our visual system extracts from the retinal input in early visual regions. The wide spread view argues for extraction and integration of contours in the first stages (V1->V4). However, this view cannot explain how selectivity for contrast in large regions is generated. Many open questions remain about how face-selective cells build up this contrast selectivity and where this information flows from.

Another aspect that has not been explored fully is how such features are integrated and whether a simple computational model can explain the observed firing rates. The standard viola-jones architecture argues for Boolean feature detector with yes/no responses. Our observations indicate that face-selective cells in regions MF and ML have graded responses. Preliminary analysis demonstrated that the graded responses depend on the intensity in each part (Figure 2). We considered several models to explain the observed variation in responses and classified models according to whether they use first order or second order approximation, and whether each approximation is linear or not:

$R = \overbrace{f_1(I_1) + f_2(I_2) + \ldots + f_{11}(I_{11})}^{\text{First Order Approximation}} + \overbrace{f_{12}(I_1, I_2) + f_{23}(I_2, I_3) + \ldots + f_{10,11}(I_{10}, I_{11})}^{\text{Second Order Approximation}} + baseline$, where R is the observed average firing rate per image (1x432), f_i are the first order approximation functions, I_i are the luminance levels in each of the eleven parts and f_{ij} are second order approximation functions.

Luminance/Contrast Models are a first order linear approximation which requires eleven coefficients. The responses are described as: $R = \alpha_1 I_1 + \ldots + \alpha_{11} I_{11} + \ldots + baseline$.

The contrast model describes the data in terms of the luminance difference across pairs of parts: $R = \alpha_{1,2}(I_1 - I_2) + \alpha_{2,3}(I_2 - I_3) + \ldots + baseline$. The contrast model is equivalent to the luminance model since the coefficients can be rearranged to form a first order linear model.

The Contrast Polarity Model, on the other hand, is a second order non-linear approximation. The non-linear functions are the sign of the luminance difference across pairs of parts: $R = \alpha_{1,2}\sigma(I_1 - I_2) + \alpha_{2,3}\sigma(I_2 - I_3) + \ldots + \alpha_{11,12}\sigma(I_{11} - I_{12}) + baseline$

The full model requires 55 coefficients. It can be shown that a linear combination of these coefficients can in fact yield the original luminance permutation. Thus, this model encapsulates the data found in a first order linear approximation (in case inputs are permutations). Any subset of this model that contains less than 55 coefficients cannot be used to reconstruct the exact permutation from the subset of coefficients.

To test these models, we used the general linear model (GLM) to account for the response variance: $R = X\beta$, where R is the average response to a different stimulus, X is the design matrix containing the regressor coefficients, and β is the weight vector. The design matrix for the luminance model contained the permutations used to construct the stimuli. The design matrix for contrast sign model contained the sign of the difference of the selected part pairs. We used adjusted R^2 measure to compare between model with different number of regressors $R^2 = 1-\left(1-\tilde{R}^2\right)\frac{n-1}{n-p-1}$, where n is the number of data points, p is the number of regressors, and $\tilde{R}$ is the unadjusted explained variance.

Our model fitting results indicated that a first order linear model could account for 67% of the variance of the average population response. However, the fraction was significantly lower for explaining individual cell responses (13% ± 12%), suggesting that second order information is needed.

To assess the contribution of contrast magnitude vs. contrast polarity we compared GLM fits for contrast models and contrast polarity models with a varying number of regressors. We found that the contrast polarity model with 11 regressors could explain the average population response equally as well as the contrast model (magnitude and polarity), suggesting that the population response can be explained in terms of contrast polarity alone (Figure 3). The two models had similar power in explaining individual cell responses as well ($P > 0.7$, paired t-test).

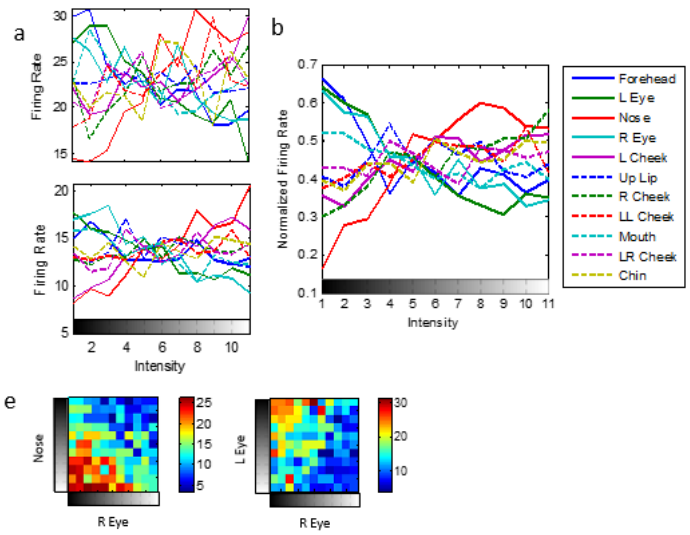

Figure 2. Responses to intensity changes in parts constituting the face. a) two examples of face-selective cells average responses as a function of the intensity in a specific part (averaged across all other parts). b) Population analysis shows that the critical regions are the nose, forehead and two eyes. c) 2D distribution of firing rates as a function of the intensity in two parts.

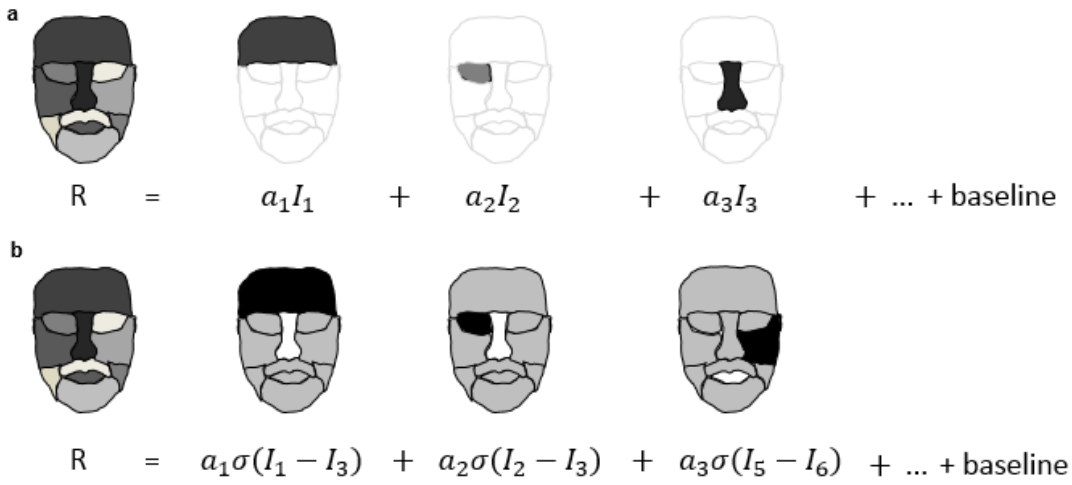

Figure 3. Model comparison. a) Intensity model predicts the responses are a linear combination of the intensities in each part. b) Contrast polarity model predicts that the responses are a weighted sum of the sign between parts.

Optogenetics

One of the goals of my experiments with applying optogenetics in NHPs was to test how useful this technique is compared to existing electrical micro-stimulation, which our lab has been using for several years. While there are obvious advantages of using optogenetics (the ability to target specific cell types, stimulate only the soma without axons, etc), many challenges remain. First and foremost, it seems that such approach is less suited for acute experiments. Optrode probes have larger diameter (~300um for a home-brewed optrode) compared to standard tungsten electrodes (175um) causing significant more damage (Figure 4). Associated problems are attempting to push a flat fiber tip into the brain, compared to a sharp electrode tip that is only a few microns. Other issues are related to gaps caused by gluing the electrode to the fiber. Beveling the fiber tip is difficult since the silica core is very fragile. For experiments lasting more than a couple of weeks, it is therefore advised to use smaller fiber diameters (< 100um) with very thin tungsten electrodes (75um). A better alternative is to use custom coaxial probes (Ozdena, Wangb et al. 2013) which are unfortunately not yet commercially available. Another direction is to develop custom MR-compatible semi-chronic drives, such as the one in Figure 4b. A semi-chronic small advancer that could remain in the chamber for the duration of the experiments (weeks) may be more effective in reducing damage.

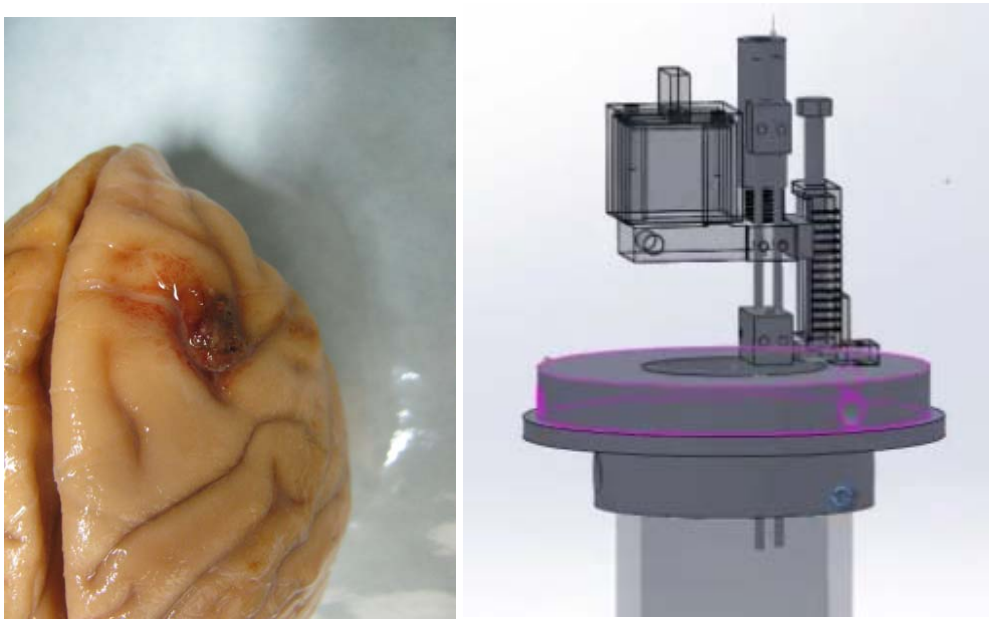

Figure 4. Left: damage from repetitive acute optogenetic experiments in the frontal eye field of monkey B. Right: semi-chronic MR-compatible drive, designed to lower a small optic fiber with fine tetrode wires.

My experiments with applying Optogenetics to non-human primates have emphasized how little we know about underlying mechanism for driving motor behavior. For example, when considering the frontal-eye-field, it is not clear what exactly happens when electrical micro-stimulation is used to evoke saccades. The effective stimulation frequencies needed are higher than 100 Hz, beyond the biologically feasible firing rate range of most pyramidal neurons. Can it be that such stimulation inhibits large portions of the network? How does it "tap" to only a subset of neurons that encode a specific saccade direction? Why only that direction "wins" even though a large fraction of the network is strongly modulated? It seems that once we better understand how electrical stimulation drives the network to evoke a motor

behavior, we could better engineer optogenetics expression and light delivery system to achieve more effective stimulations.

It is quite clear that current optogenetic construct/probes/light delivery methods still fall short compared to electrical micro-stimulation when it comes for evoking behavior in NHP. However, this does not mean optogenetics is not useful. Far from it! One major advantageous optogenetic has over electrical stimulation is the ability to record while stimulating. Preliminary results of targeting viral injection to face-patch MF revealed that face-selective cells can be robustly modulated with light (figure 5). Interestingly, it is quite clear that stimulation does not saturate the dynamic range of firing rate that can be evoked by cells (at least, not when delivering continuous stimulation). In figure 5, for example, two face-selective cells are shown. The response to individual non-face objects with stimulation varies greatly, indicating that different amount of input/inhibition is applied on the cell. Furthermore, complex firing dynamics are observed following stimulation. For example, the right most cell in figure 6 shows very strong excitation when stimulation is applied and the monkey is fixating a dot, compared to strong inhibition that takes place when the monkey is stimulated and fixates a face. Studying temporal dynamics with optogenetics stimulation is also an interesting direction. For example, in figure 7, the same 50 ms train is applied to a face-selective cell at varying lags relative to stimulus onset. Although stimulation ends at 50 ms, a clear reduced response is observed for the presented face. A result that is probably not caused directly from the channel kinetics, since those are fast to close when light is off, but rather due to second network effects coming into play to inhibit this cell.

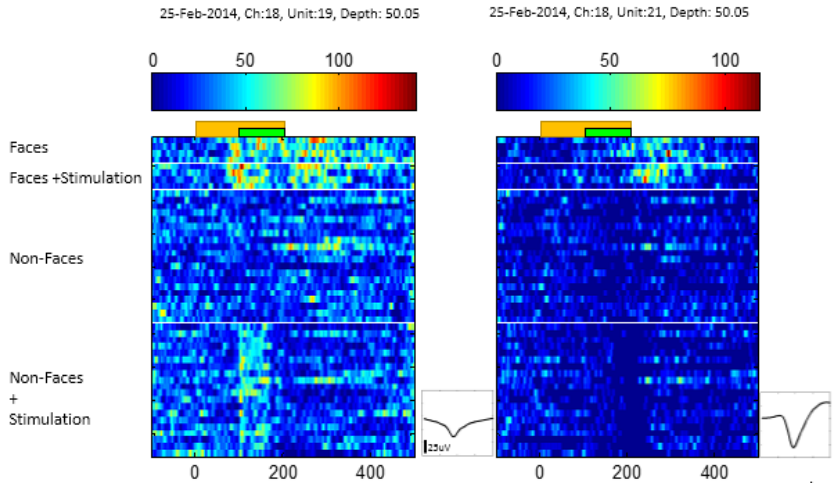

Figure 5. ChR2 modulation of face-selective cells. Recordings in face patch MF, injected with AAV5-hSyn-ChR2(H134R)-eYFP. Orange intervals represents the interval an image was on the screen. Continuous light stimulation (green interval) was delivered 100 ms after stimulus onset (time 0) for 100 ms. Small insets show spike wave form.

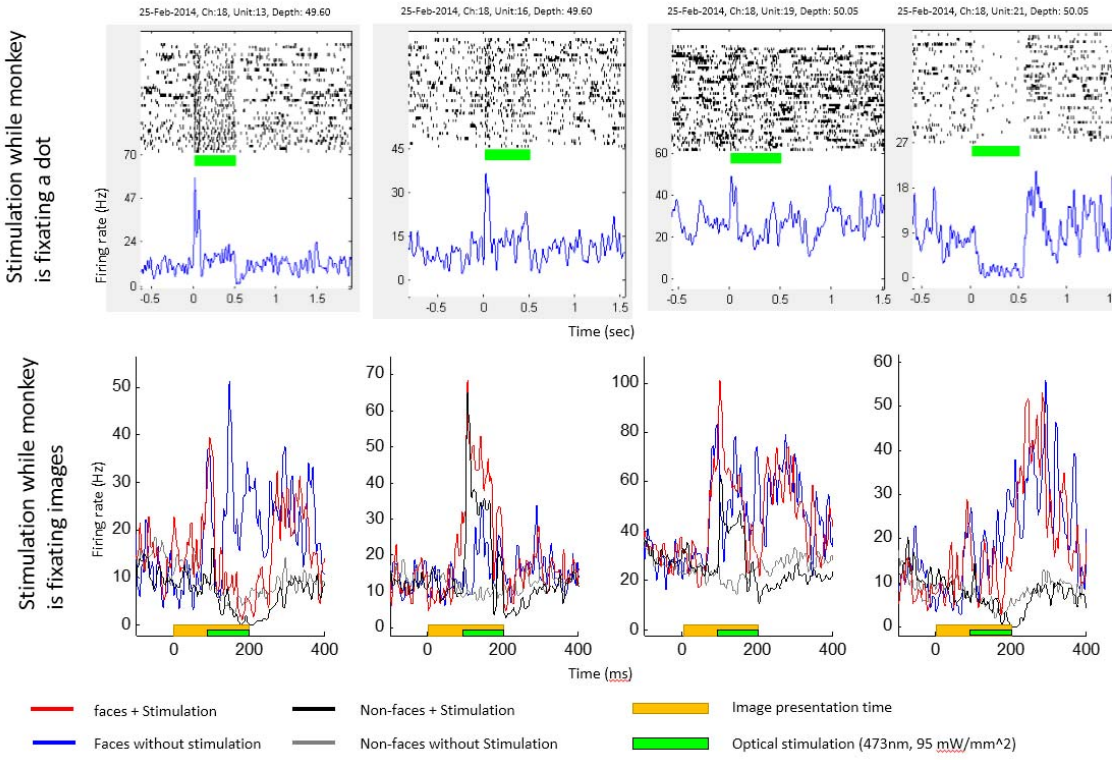

Figure 6. ChR2 modulation of face-selective cells. Top: responses of four face-selective cells to a brief 500 ms light stimulation while monkey is fixating a small dot. Bottom: same cells, but responses to a 100 ms light stimulation (green interval), at 100 ms lag relative to image presentation (orange interval). Images were either faces or non-face objects.

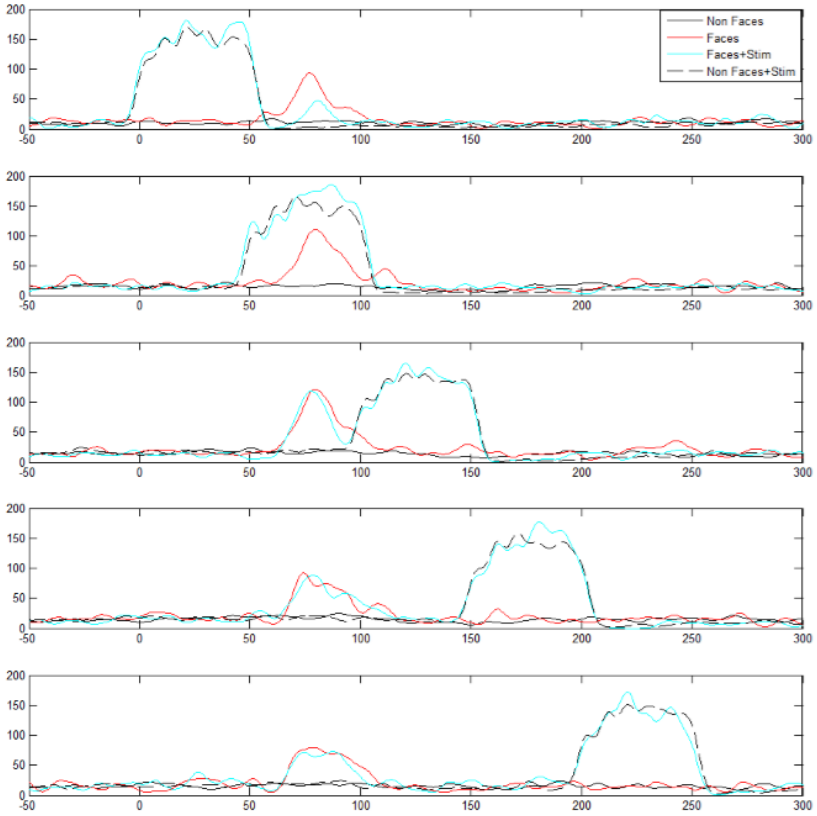

Figure 7. Temporal dynamics of a face-selective cell in face patch MF. Continuous light pulse (50 ms) delivered at [0, 50, 100, 150, 200] ms relative to image onset. Monkey was fixating non-face images (black trace) or face images (red and cyan traces).

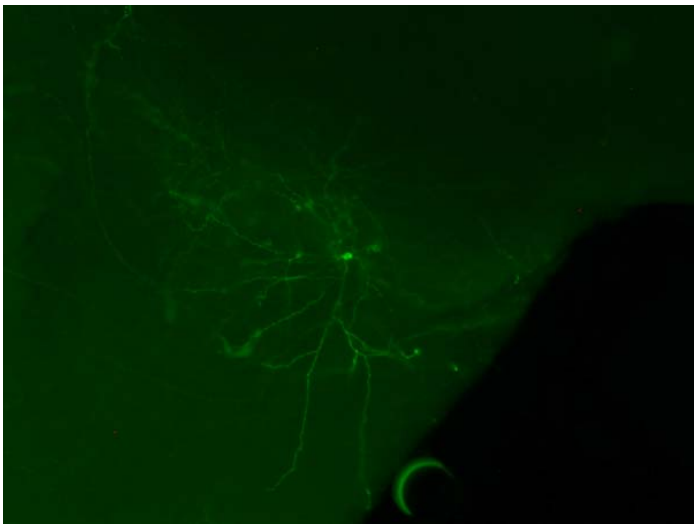

Figure 8. A double labeled cell in a rat injected with CAV-Cre in motor cortex and AAV-EF1a-DIO-ChR2-eYFP in sensimotor cortex.

Finally, one of the more exciting directions of applying optogenetics is the study of the functional properties of specific cell types. Only a handful of promoters to target specific cell types in NHP are currently available (Thy1, hSyn, CAG, CMV, CamKII). Among them, only CamKII express in a subset of neurons (excitatory pyramidal), and even that needs to be validated carefully as the same promoter can express differently when delivered with different viral vectors (AAV/Lenti). If expression is limited to a specific cell type, identification may be done based on latency analysis, yet, such approach may be tricky due to fast secondary network effects.

Another interesting avenue is to study cells not only based on their expression patterns according to a specific promoter, but to use viral intersection techniques to specifically label cells according to some Boolean logic. For example, by injecting retrograde virus carrying

the Cre cassette to region X, and injecting Cre-dependent (lox-floxed ChR2 construct) to region Y, one can label only the cells that project from X to Y. The main issue with this approach is the lack of safe retrograde viruses that can carry the gene of interest. Recently, several reports emerged about a new virus: Canine Adeno Virus (CAV) which was shown to transport retrograde in rodents, with minimal or no long term damage (Kremer, Boutin et al. 2000, Soudais, Laplace-Builhe et al. 2001, Soudais, Skander et al. 2004, Bru, Salinas et al. 2010). Pilot studies in rats performed in our lab seemed encouraging. We targeted primary motor cortex and injected CAV-Cre, and primary sensorimotor region (S1) and injected AAV5-EF1a-DIO-ChR2-eYFP, a lox-flocked ChR2 construct. Standard immunohistochemistry analysis revealed a very sparse set of neurons expressing YFP (figure 8).

We attempted to replicate these results on NHPs. We first localized face-responsive regions, specifically using fMRI. Regions AL and ML were chosen for the experiment since they were easily accessible and known to have strong anatomical connection. We then electrically micro-stimulated region AL while monkeys were scanned in the fMRI and observed very small region in MF activated (figure 9). We targeted that small region for electrophysiology And delivered CAV-Cre and CAV-GFP to that region. We then targeted region AL for electrophstiology, and injected AAV5-EF1a-DIO-ChR2(h134R)-mCherry. Unfortunately, no light responsive cells were found in face patch AL. Attempts were made to debug things in-vivo by constructing a fiber-optic fluorescence microscope. A fiber was slowly lowered and multiple measurements of returned fluorescence were taken as a function of depth (figure

10). This data suggested that CAV-GFP did express in region ML, but since no light responsive cells were found in AL, we are left to conclude that either the retrograde transport was not efficient to reach AL, or that our targeting of the projection from ML to AL is off.

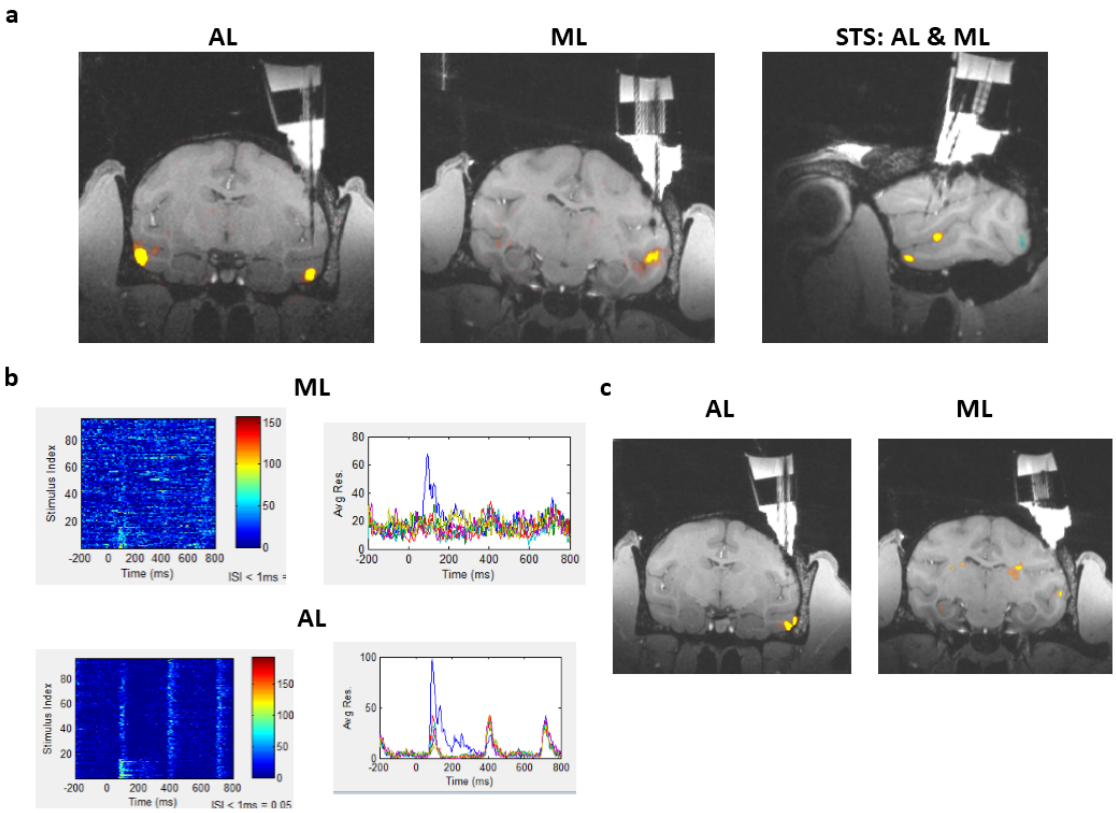

Figure 9. Localizing suitable regions for viral intersection experiment. **a)** fMRI result of a face-localizer in monkey H clearly identified regions AL and ML on the right hemisphere. **b)** MR-guided electrophysiology confirmed that these regions contain face-selective cells. **c)** Combined fMRI and electrical micro-stimulation in face-patch AL revealed that a very small region of ML is significantly active when AL is stimulated.

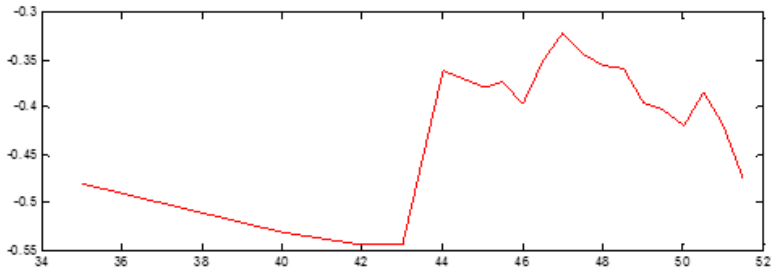

Figure 10: In-vivo fluorescence measurement in a region injected with CAV-GFP in monkey H. X axis denotes depth in mm and Y axis denotes measured fluorescence values (AU).

Bibliography

1. Baldassi, C., A. Alemi-Neissi, M. Pagan, J. J. Dicarlo, R. Zecchina and D. Zoccolan (2013). "Shape similarity, better than semantic membership, accounts for the structure of visual object representations in a population of monkey inferotemporal neurons." *PLoS Comput Biol* **9**(8): e1003167.
2. Baylis, G. C. and J. Driver (2001). "Shape-coding in IT cells generalizes over contrast and mirror reversal, but not figure-ground reversal " *Nature Neuroscience* **4**: 857-858.
3. Bell, A. H., N. J. Malecek, E. L. Morin, F. Hadj-Bouziane, R. B. Tootell and L. G. Ungerleider (2011). "Relationship between functional magnetic resonance imaging-identified regions and neuronal category selectivity." *J Neurosci* **31**(34): 12229-12240.
4. Berens, P. (2009). "CircStat: A Matlab Toolbox for Circular Statistics." *Journal of Statistical Software* **31**(10).
5. Boyden, E. S. (2011). "A history of optogenetics: the development of tools for controlling brain circuits with light." *F1000 Biol Rep* **3**: 11.
6. Boyden, E. S., F. Zhang, E. Bamberg, G. Nagel and K. Deisseroth (2005). "Millisecond-timescale, genetically targeted optical control of neural activity." *Nat Neurosci* **8**(9): 1263-1268.
7. Brincat, S. L. and C. E. Connor (2004). "Underlying principles of visual shape selectivity in posterior inferotemporal cortex." *Nat Neurosci* **7**(8): 880-886.

8. Bru, T., S. Salinas and E. J. Kremer (2010). "An update on canine adenovirus type 2 and its vectors." *Viruses* **2**(9): 2134-2153.
9. Bruce, C. J., M. E. Goldberg, M. C. Bushnell and G. B. Stanton (1985). "Primate frontal eye fields. II. Physiological and anatomical correlates of electrically evoked eye movements." *J Neurophysiol* **54**(3): 714-734.
10. Brunelli, R. and T. Poggio (1993). "Face Recognition - Features Versus Templates." *Ieee Transactions on Pattern Analysis and Machine Intelligence* **15**(10): 1042-1052.
11. Buffalo, E. A., S. J. Ramus, R. E. Clark, E. Teng, L. R. Squire and S. M. Zola (1999). "Dissociation between the effects of damage to perirhinal cortex and area TE." *Learn Mem* **6**(6): 572-599.
12. Cavanaugh, J., I. E. Monosov, K. McAlonan, R. Berman, M. K. Smith, V. Cao, K. H. Wang, E. S. Boyden and R. H. Wurtz (2012). "Optogenetic inactivation modifies monkey visuomotor behavior." *Neuron* **76**(5): 901-907.
13. Cerf, M., E. P. Frady and C. Koch (2009). "Faces and text attract gaze independent of the task: Experimental data and computer model." *J Vis* **9**(12): 10 11-15.
14. Chow, B. Y., X. Han and E. S. Boyden (2012). "Genetically encoded molecular tools for light-driven silencing of targeted neurons." *Prog Brain Res* **196**: 49-61.
15. Chow, B. Y., X. Han, A. S. Dobry, X. Qian, A. S. Chuong, M. Li, M. A. Henninger, G. M. Belfort, Y. Lin, P. E. Monahan and E. S. Boyden (2010). "High-performance genetically targetable optical neural silencing by light-driven proton pumps." *Nature* **463**(7277): 98-102.

16. Cohen, M. R. and W. T. Newsome (2004). "What electrical microstimulation has revealed about the neural basis of cognition." *Current Opinion in Neurobiology* **14**: 1-9.
17. Conway, B. R., S. Moeller and D. Y. Tsao (2007). "Specialized color modules in macaque extrastriate cortex." *Neuron* **56**(3): 560-573.
18. Deisseroth, K., G. Feng, A. K. Majewska, G. Miesenbock, A. Ting and M. J. Schnitzer (2006). "Next-generation optical technologies for illuminating genetically targeted brain circuits." *J Neurosci* **26**(41): 10380-10386.
19. Desai, M., I. Kahn, U. Knoblich, J. Bernstein, H. Atallah, A. Yang, N. Kopell, R. L. Buckner, A. M. Graybiel, C. I. Moore and E. S. Boyden (2011). "Mapping brain networks in awake mice using combined optical neural control and fMRI." *J Neurophysiol* **105**(3): 1393-1405.
20. Desimone, R., T. D. Albright, C. G. Gross and C. Bruce (1984). "Stimulus-selective properties of inferior temporal neurons in the macaque." *J Neurosci* **4**(8): 2051-2062.
21. DiCarlo, J. J., D. Zoccolan and N. C. Rust (2012). "How does the brain solve visual object recognition?" *Neuron* **73**(3): 415-434.
22. Diester, I., M. T. Kaufman, M. Mogri, R. Pashaie, W. Goo, O. Yizhar, C. Ramakrishnan, K. Deisseroth and K. V. Shenoy (2011). "An optogenetic toolbox designed for primates." *Nat Neurosci* **14**(3): 387-397.
23. Dugue, G. P., W. Akemann and T. Knopfel (2012). "A comprehensive concept of optogenetics." *Prog Brain Res* **196**: 1-28.

24. Eifuku, S., W. C. De Souza, R. Tamura, H. Nishijo and T. Ono (2004). "Neuronal correlates of face identification in the monkey anterior temporal cortical areas." *J Neurophysiol* **91**(1): 358-371.

25. Ekstrom, L. B., P. R. Roelfsema, J. T. Arsenault, G. Bonmassar and W. Vanduffel (2008). "Bottom-up dependent gating of frontal signals in early visual cortex." *Science* **321**(5887): 414-417.

26. Frangi, A., Niessen, W., Vincken, K., Viergever, M. (1998). "Multiscale vessel enhancement filtering." *Medical Image Computing and Computer-Assisted Intervention*: 130–137.

27. Freiwald, W. A. and D. Y. Tsao (2010). "Functional Compartmentalization and Viewpoint Generalization Within the Macaque Face-Processing System." *Science* **330**(6005): 845-851.

28. Freiwald, W. A., D. Y. Tsao and M. S. Livingstone (2009). "A face feature space in the macaque temporal lobe." *Nat Neurosci* **12**(9): 1187-1196.

29. Fujita, I., K. Tanaka, M. Ito and K. Cheng (1992). "Columns for visual features of objects in monkey inferotemporal cortex." *Nature* **360**(6402): 343-346.

30. Galvan, A., X. Hu, Y. Smith and T. Wichmann (2012). "In vivo optogenetic control of striatal and thalamic neurons in non-human primates." *PLoS One* **7**(11): e50808.

31. George, N., R. J. Dolan, G. R. Fink, G. C. Baylis, C. Russell and J. Driver (1999). "Contrast polarity and face recognition in the human fusiform gyrus." *Nat Neurosci* **2**(6): 574-580.

32. Gerits, A., R. Farivar, B. R. Rosen, L. L. Wald, E. S. Boyden and W. Vanduffel (2012). "Optogenetically induced behavioral and functional network changes in primates." *Curr Biol* **22**(18): 1722-1726.
33. Gilad, S., M. Meng and P. Sinha (2009). "Role of ordinal contrast relationships in face encoding." *Proc Natl Acad Sci USA* **106**(13): 5353-5358.
34. Goldberg, M. E., M. C. Bushnell and C. J. Bruce (1986). "The effect of attentive fixation on eye movements evoked by electrical stimulation of the frontal eye fields." *Exp Brain Res* **61**(3): 579-584.
35. Gradinaru, V., K. R. Thompson and K. Deisseroth (2008). "eNpHR: a Natronomonas halorhodopsin enhanced for optogenetic applications." *Brain Cell Biol* **36**(1-4): 129-139.
36. Gradinaru, V., K. R. Thompson, F. Zhang, M. Mogri, K. Kay, M. B. Schneider and K. Deisseroth (2007). "Targeting and readout strategies for fast optical neural control in vitro and in vivo." *J Neurosci* **27**(52): 14231-14238.
37. Gradinaru, V., F. Zhang, C. Ramakrishnan, J. Mattis, R. Prakash, I. Diester, I. Goshen, K. R. Thompson and K. Deisseroth (2010). "Molecular and cellular approaches for diversifying and extending optogenetics." *Cell* **141**(1): 154-165.
38. Graziano, M. S., C. S. Taylor and T. Moore (2002). "Complex movements evoked by microstimulation of precentral cortex." *Neuron* **34**(5): 841-851.
39. Gross, C. G. (1973). "Inferotemporal cortex and vision ".
40. Gross, C. G. (1994). "How Inferior Temporal Cortex Became a Visual Area." *Cerebral Cortex* **4**(5): 455-469.

41. Gunaydin, L. A., O. Yizhar, A. Berndt, V. S. Sohal, K. Deisseroth and P. Hegemann (2010). "Ultrafast optogenetic control." *Nat Neurosci* **13**(3): 387-392.

42. Han, X. (2012). "Optogenetics in the nonhuman primate." *Prog Brain Res* **196**: 215-233.

43. Han, X., B. Y. Chow, H. Zhou, N. C. Klapoetke, A. Chuong, R. Rajimehr, A. Yang, M. V. Baratta, J. Winkle, R. Desimone and E. S. Boyden (2011). "A high-light sensitivity optical neural silencer: development and application to optogenetic control of non-human primate cortex." *Front Syst Neurosci* **5**: 18.

44. Han, X., X. Qian, J. G. Bernstein, H. H. Zhou, G. T. Franzesi, P. Stern, R. T. Bronson, A. M. Graybiel, R. Desimone and E. S. Boyden (2009). "Millisecond-timescale optical control of neural dynamics in the nonhuman primate brain." *Neuron* **62**(2): 191-198.

45. Harmon, L. D. and B. Julesz (1973). "Masking in visual recognition: effects of two-dimensional filtered noise." *Science* **180**(4091): 1194-1197.

46. Haupts, U., J. Tittor and D. Oesterhelt (1999). "Closing in on Bateriorhodopsin: Progress in Understanding the Molecule." *Annv. Rev. Biophys. Biomol. Struct* **28**: 367-399.

47. Heinrich, S. P. and M. Bach (2010). "Less is more: Subjective detailedness depends on stimulus size." *Journal of Vision* **10**(10): 2.

48. Heisele, B., T. Poggio and M. Pontil (2000). Face Detection in Still Gray Images, Center for Biological and Computational Learning, MIT.

49. Histed, M. H., V. Bonin and R. C. Reid (2009). "Direct activation of sparse, distributed populations of cortical neurons by electrical microstimulation." *Neuron* **63**(4): 508-522.

50. Hoffmann, K. P., F. Bremmer and C. Distler (2009). "Visual response properties of neurons in cortical areas MT and MST projecting to the dorsolateral pontine nucleus or the nucleus of the optic tract in macaque monkeys." *Eur J Neurosci* **29**(2): 411-423.

51. Horel, J. A., D. E. Pytko-Joiner, M. L. Voytko and K. Salsbury (1987). "The performance of visual tasks while segments of the inferotemporal cortex are suppressed by cold." *Behav Brain Res* **23**(1): 29-42.

52. Ichinohe, N., A. Matsushita, K. Ohta and K. S. Rockland (2010). "Pathway-specific utilization of synaptic zinc in the macaque ventral visual cortical areas." *Cereb Cortex* **20**(12): 2818-2831.

53. Issa, E. B. and J. J. DiCarlo (2012). "Precedence of the eye region in neural processing of faces." *J Neurosci* **32**(47): 16666-16682.

54. Ito, M., I. Fujita, H. Tamura and K. Tanaka (1994). "Processing of contrast polarity of visual images in inferotemporal cortex of the macaque monkey." *Cereb Cortex* **4**(5): 499-508.

55. Jazayeri, M., Z. Lindbloom-Brown and G. Horwitz (2012). "Saccadic eye movements evoked by optogenetic activation of primate V1." *Nature Neuroscience*.

56. Jing, W., W. Wenchao, L. Lin, L. Li, W. Guimei, T. Heng, J. Huihui, W. Jianhong, M. Yuanye and H. Xintian (2010). "A new MRI approach for accurately implanting microelectrodes into deep brain structures of the rhesus monkey (Macaca mulatta)." *J Neurosci Methods* **193**(2): 203-209.

57. Kanwisher, N., J. McDermott and M. M. Chun (1997). "The fusiform face area: a module in human extrastriate cortex specialized for face perception." *J Neurosci* **17**(11): 4302-4311.

58. Kayser, C., C. I. Petkov, M. Augath and N. K. Logothetis (2007). "Functional imaging reveals visual modulation of specific fields in auditory cortex." *J Neurosci* **27**(8): 1824-1835.

59. Kenneth D. Harris, D. A. H., Jozsef Csicsvari, Hajime Hirase, and György Buzsáki (2000). "Accuracy of Tetrode Spike Separation as Determined by Simultaneous Intracellular and Extracellular Measurements. ." *Journal of Neurophysiology* **84**: 401-414.

60. Kiani, R., H. Esteky, K. Mirpour and K. Tanaka (2007). "Object category structure in response patterns of neuronal population in monkey inferior temporal cortex." *J Neurophysiol* **97**(6): 4296-4309.

61. Klapoetke, N. C., Y. Murata, S. S. Kim, S. R. Pulver, A. Birdsey-Benson, Y. K. Cho, T. K. Morimoto, A. S. Chuong, E. J. Carpenter, Z. Tian, J. Wang, Y. Xie, Z. Yan, Y. Zhang, B. Y. Chow, B. Surek, M. Melkonian, V. Jayaraman, M. Constantine-Paton, G. K. Wong and E. S. Boyden (2014). "Independent optical excitation of distinct neural populations." *Nat Methods* **11**(3): 338-346.

62. Konkle, T. and A. Oliva (2012). "A real-world size organization of object responses in occipitotemporal cortex." *Neuron* **74**(6): 1114-1124.

63. Kourtzi, Z. and C. E. Connor (2011). "Neural representations for object perception: structure, category, and adaptive coding." *Annu Rev Neurosci* **34**: 45-67.

64. Kremer, E. J., S. Boutin, M. Chillon and O. Danos (2000). "Canine adenovirus vectors: an alternative for adenovirus-mediated gene transfer." *J Virol* **74**(1): 505-512.

65. Kriegeskorte, N., M. Mur, D. A. Ruff, R. Kiani, J. Bodurka, H. Esteky, K. Tanaka and P. A. Bandettini (2008). "Matching categorical object representations in inferior temporal cortex of man and monkey." *Neuron* **60**(6): 1126-1141.

66. Lafer-Sousa, R. and B. R. Conway (2013). "Parallel, multi-stage processing of colors, faces and shapes in macaque inferior temporal cortex." *Nat Neurosci* **16**(12): 1870-1878.

67. Lee, J. H., R. Durand, V. Gradinaru, F. Zhang, I. Goshen, D. S. Kim, L. E. Fenno, C. Ramakrishnan and K. Deisseroth (2010). "Global and local fMRI signals driven by neurons defined optogenetically by type and wiring." *Nature* **465**(7299): 788-792.

68. Leite, F. P., D. Tsao, W. Vanduffel, D. Fize, Y. Sasaki, L. L. Wald, A. M. Dale, K. K. Kwong, G. A. Orban, B. R. Rosen, R. B. Tootell and J. B. Mandeville (2002). "Repeated fMRI using iron oxide contrast agent in awake, behaving macaques at 3 Tesla." *Neuroimage* **16**(2): 283-294.

69. Leopold, D. A., I. V. Bondar and M. A. Giese (2006). "Norm-based face encoding by single neurons in the monkey inferotemporal cortex." *Nature* **442**(7102): 572-575.

70. Lerchner, W., B. Corgiat, V. Der Minassian, R. C. Saunders and B. J. Richmond (2014). "Injection parameters and virus dependent choice of promoters to improve neuron targeting in the nonhuman primate brain." *Gene Ther* **21**(3): 233-241.

71. Li, X., D. V. Gutierrez, M. G. Hanson, J. Han, M. D. Mark, H. Chiel, P. Hegemann, L. T. Landmesser and S. Herlitze (2005). "Fast noninvasive activation and inhibition of neural and network activity by vertebrate rhodopsin and green algae channelrhodopsin." *Proc Natl Acad Sci USA* **102**(49): 17816-17821.

72. Lienhart, R. and J. Maydt (2002). "An extended set of haar-like features for rapid object detection." *2002 International Conference on Image Processing, Vol I, Proceedings*: 900-903.

73. Lin, J. Y. (2012). "Optogenetic excitation of neurons with channelrhodopsins: light instrumentation, expression systems, and channelrhodopsin variants." *Prog Brain Res* **196**: 29-47.

74. Lin, J. Y., M. Z. Lin, P. Steinbach and R. Y. Tsien (2009). "Characterization of engineered channelrhodopsin variants with improved properties and kinetics." *Biophys J* **96**(5): 1803-1814.

75. Logothetis, N. K. (2008). "What we can do and what we cannot do with fMRI." *Nature* **453**(7197): 869-878.

76. Logothetis, N. K., M. Augath, Y. Murayama, A. Rauch, F. Sultan, J. Goense, A. Oeltermann and H. Merkle (2010). "The effects of electrical microstimulation on cortical signal propagation." *Nat Neurosci* **13**(10): 1283-1291.

77. Logothetis, N. K., J. Pauls, H. H. Bulthoff and T. Poggio (1994). "View-dependent object recognition by monkeys." *Curr Biol* **4**(5): 401-414.

78. Logothetis, N. K., J. Pauls and T. Poggio (1995). "Shape representation in the inferior temporal cortex of monkeys." *Curr Biol* **5**(5): 552-563.

79. Logothetis, N. K. and D. L. Sheinberg (1996). "Visual object recognition." *Annu Rev Neurosci* **19**: 577-621.

80. Mattis, J., K. M. Tye, E. A. Ferenczi, C. Ramakrishnan, D. J. O'Shea, R. Prakash, L. A. Gunaydin, M. Hyun, L. E. Fenno, V. Gradinaru, O. Yizhar and K. Deisseroth (2012). "Principles for applying optogenetic tools derived from direct comparative analysis of microbial opsins." *Nat Methods* **9**(2): 159-172.

81. Moeller, S., W. A. Freiwald and D. Y. Tsao (2008). "Patches with links: a unified system for processing faces in the macaque temporal lobe." *Science* **320**(5881): 1355-1359.

82. Moore, T. and M. Fallah (2004). "Microstimulation of the frontal eye field and its effects on covert spatial attention." *J Neurophysiol* **91**(1): 152-162.

83. Movshon, J. A. and W. T. Newsome (1996). "Visual response properties of striate cortical neurons projecting to area MT in macaque monkeys." *J Neurosci* **16**(23): 7733-7741.

84. Murphey, D. K. and J. H. Maunsell (2007). "Behavioral detection of electrical microstimulation in different cortical visual areas." *Curr Biol* **17**(10): 862-867.

85. Nagel, G., M. Brauner, J. F. Liewald, N. Adeishvili, E. Bamberg and A. Gottschalk (2005). "Light activation of channelrhodopsin-2 in excitable cells of Caenorhabditis elegans triggers rapid behavioral responses." *Curr Biol* **15**(24): 2279-2284.

86. Nagel, G., D. Ollig, M. Fuhrmann, S. Kateriya, A. M. Musti, E. Bamberg and P. Hegemann (2002). "Channelrhodopsin-1: a light-gated proton channel in green algae." *Science* **296**(5577): 2395-2398.

87. Nagel, G., T. Szellas, W. Huhn, S. Kateriya, N. Adeishvili, P. Berthold, D. Ollig, P. Hegemann and E. Bamberg (2003). "Channelrhodopsin-2, a directly light-gated cation-selective membrane channel." *Proc Natl Acad Sci USA* **100**(24): 13940-13945.

88. Oesterhelt, D. and W. Stoeckenius (1973). "Functions of a New Photoreceptor Membrane " *Proc. Nat. Acad. Sci.* **70**(10): 2853-2857.

89. Ohayon, S., W. A. Freiwald and D. Y. Tsao (2012). "What makes a cell face selective? The importance of contrast." *Neuron* **74**(3): 567-581.

90. Ohayon, S., P. Grimaldi, N. Schweers and D. Y. Tsao (2013). "Saccade modulation by optical and electrical stimulation in the macaque frontal eye field." *J Neurosci* **33**(42): 16684-16697.

91. Ohayon, S. and D. Y. Tsao (2012). "MR-guided stereotactic navigation." *J Neurosci Methods* **204**(2): 389-397.

92. Ozdena, I., J. Wangb, Y. Luc, T. Maya, J. Leea, W. Good, D. J. O'Sheae, P. Kalanithi, I. Diester, M. Diagne, K. Deisseroth, K. V. Shenoyd and A. V. Nurmikko (2013). "A coaxial optrode as multifunction write-read probe for optogenetic studies in non-human primates." *Journal of neuroscience Methods* **219**: 142-154.

93. Pagan, M., L. S. Urban, M. P. Wohl and N. C. Rust (2013). "Signals in inferotemporal and perirhinal cortex suggest an untangling of visual target information." *Nat Neurosci* **16**(8): 1132-1139.

94. Papageorgiou, C. P., M. Oren and T. Poggio (1998). "A general framework for object detection." *Sixth International Conference on Computer Vision*: 555-562.

95. Pasupathy, A. and C. E. Connor (1999). "Responses to contour features in macaque area V4." *J Neurophysiol* **82**(5): 2490-2502.

96. Pasupathy, A. and C. E. Connor (2002). "Population coding of shape in area V4." *Nat Neurosci* **5**(12): 1332-1338.

97. Paxinos, G., X. F. Huang and A. W. Toga (2000). The rhesus monkey brain in stereotaxic coordinates. San Diego, CA, Academic Press.

98. Paxinos, G. and C. Watson (2007). The rat brain in stereotaxic coordinates. Amsterdam ; Boston ;, Academic Press/Elsevier.

99. \Poggio, T. and S. Edelman (1990). "A network that learns to recognize three-dimensional objects." *Nature* **343**(6255): 263-266.

100. Popivanov, I. D., J. Jastorff, W. Vanduffel and R. Vogels (2012). "Stimulus representations in body-selective regions of the macaque cortex assessed with event-related fMRI." *Neuroimage* **63**(2): 723-741.

101. Rolls, E. T. and G. C. Baylis (1986). "Size and Contrast Have Only Small Effects on the Responses to Faces of Neurons in the Cortex of the Superior Temporal Sulcus of the Monkey." *Experimental Brain Research* **65**(1): 38-48.

102. Ruiz, O., B. R. Lustig, J. J. Nassi, A. H. Cetin, J. H. Reynolds, T. D. Albright, E. M. Callaway, G. R. Stoner and A. W. Roe (2013). "Optogenetics through windows on the brain in the nonhuman primate." *J Neurophysiol*.

103. Rust, N. C. and J. J. Dicarlo (2010). "Selectivity and tolerance ("invariance") both increase as visual information propagates from cortical area V4 to IT." *J Neurosci* **30**(39): 12978-12995.

104. Saleem, K. (2006). Atlas of the rhesus monkey brain in stereotaxic coordinates : a combined mri and histology. Boston, MA, Elsevier.

105. Saleem, K. S. and N. Logothetis (2007). A combined MRI and histology atlas of the rhesus monkey brain in stereotaxic coordinates. London ; Burlington, MA, Academic.

106. Salzman, C. D., K. H. Britten and W. T. Newsome (1990). "Cortical microstimulation influences perceptual judgements of motion direction." *Nature* **346**(6280): 174-177.

107. Schwartz, E. L., R. Desimone, T. D. Albright, C. G. Gross and C. Bruce (1984). "Stimulus-selective properties of inferior temporal neurons in the macaque." *J Neurosci* **4**(8): 2051-2062.

108. Sereno, M. I., A. M. Dale, J. B. Reppas, K. K. Kwong, J. W. Belliveau, T. J. Brady, B. R. Rosen and R. B. Tootell (1995). "Borders of multiple visual areas

in humans revealed by functional magnetic resonance imaging." *Science* **268**(5212): 889-893.

109. Sinha, P. (2002). "Qualitative representations for recognition." *Biologically Motivated Computer Vision, Proceedings* **2525**: 249-262.

110. Sinha, P., B. Balas, Y. Ostrovsky and R. Russell (2006). "Face recognition by humans: Nineteen results all computer vision researchers should know about." *Proceedings of the IEEE* **94**(11): 1948-1962.

111. Sirotin, Y. B. and A. Das (2009). "Anticipatory haemodynamic signals in sensory cortex not predicted by local neuronal activity." *Nature* **457**(7228): 475-479.

112. Soudais, C., C. Laplace-Builhe, K. Kissa and E. J. Kremer (2001). "Preferential transduction of neurons by canine adenovirus vectors and their efficient retrograde transport in vivo." *FASEB J* **15**(12): 2283-2285.

113. Soudais, C., N. Skander and E. J. Kremer (2004). "Long-term in vivo transduction of neurons throughout the rat CNS using novel helper-dependent CAV-2 vectors." *FASEB J* **18**(2): 391-393.

114. Sperka, D. J. and J. Ditterich (2011). "Splash: a software tool for stereotactic planning of recording chamber placement and electrode trajectories." *Front Neuroinformatics* **5**: 1.

115. Tanaka, K. (1996). "Inferotemporal cortex and object vision." Annu Rev *Neurosci* **19**: 109-139.

116. Tanaka, K. (2003). "Columns for complex visual object features in the inferotemporal cortex: clustering of cells with similar but slightly different stimulus selectivities." *Cereb Cortex* **13**(1): 90-99.

117. Tanaka, K., H. Saito, Y. Fukada and M. Moriya (1991). "Coding visual images of objects in the inferotemporal cortex of the macaque monkey." *J Neurophysiol* **66**(1): 170-189.

118. Tolias, A. S., F. Sultan, M. Augath, A. Oeltermann, E. J. Tehovnik, P. H. Schiller and N. K. Logothetis (2005). "Mapping cortical activity elicited with electrical microstimulation using FMRI in the macaque." *Neuron* **48**(6): 901-911.

119. Tootell, R. B., J. B. Reppas, K. K. Kwong, R. Malach, R. T. Born, T. J. Brady, B. R. Rosen and J. W. Belliveau (1995). "Functional analysis of human MT and related visual cortical areas using magnetic resonance imaging." *J Neurosci* **15**(4): 3215-3230.

120. Torralba, A. and P. Sinha (2001). "Statistical context priming for object detection." *Eighth Ieee International Conference on Computer Vision, Vol I, Proceedings*: 763-770.

121. Tsao, D. Y., W. A. Freiwald, T. A. Knutsen, J. B. Mandeville and R. B. Tootell (2003). "Faces and objects in macaque cerebral cortex." *Nat Neurosci* **6**(9): 989-995.

122. Tsao, D. Y., W. A. Freiwald, R. B. Tootell and M. S. Livingstone (2006). "A cortical region consisting entirely of face-selective cells." *Science* **311**(5761): 670-674.

123. Tsao, D. Y., W. A. Freiwald, R. B. H. Tootell and M. S. Livingstone (2006). "A cortical region consisting entirely of face-selective cells." *Science* **670**: 670-674.

124. Tsao, D. Y. and M. S. Livingstone (2008). "Mechanisms of face perception." *Annu Rev Neurosci* **31**: 411-437.

125. Tsao, D. Y., S. Moeller and W. A. Freiwald (2008). "Comparing face patch systems in macaques and humans." *Proc Natl Acad Sci USA* **105**(49): 19514-19519.

126. Tsao, D. Y., W. Vanduffel, Y. Sasaki, D. Fize, T. A. Knutsen, J. B. Mandeville, L. L. Wald, A. M. Dale, B. R. Rosen, D. C. Van Essen, M. S. Livingstone, G. A. Orban and R. B. Tootell (2003). "Stereopsis activates V3A and caudal intraparietal areas in macaques and humans." *Neuron* **39**(3): 555-568.

127. Tsunoda, K., Y. Yamane, M. Nishizaki and M. Tanifuji (2001). "Complex objects are represented in macaque inferotemporal cortex by the combination of feature columns." *Nat Neurosci* **4**(8): 832-838.

128. Ullman, S., M. Vidal-Naquet and E. Sali (2002). "Visual features of intermediate complexity and their use in classification." *Nature Neuroscience* **5**(7): 682-687.

129. Urban, A. and J. Rossier (2012). "Genetic targeting of specific neuronal cell types in the cerebral cortex." *Prog Brain Res* **196**: 163-192.

130. Van Essen, D. C. (2002). "Windows on the brain: the emerging role of atlases and databases in neuroscience." *Curr Opin Neurobiol* **12**(5): 574-579.

131. Viola, P. and M. Jones (2001). "Rapid object detection using a boosted cascade of simple features." *2001 IEEE Computer Society Conference on Computer Vision and Pattern Recognition, Vol 1, Proceedings*: 511-518.

132. Wang, G., M. Tanifuji and K. Tanaka (1998). "Functional architecture in monkey inferotemporal cortex revealed by in vivo optical imaging." *Neurosci Res* **32**(1): 33-46.

133. Yamane, Y., E. T. Carlson, K. C. Bowman, Z. Wang and C. E. Connor (2008). "A neural code for three-dimensional object shape in macaque inferotemporal cortex." *Nat Neurosci* **11**(11): 1352-1360.

134. Yizhar, O., L. E. Fenno, T. J. Davidson, M. Mogri and K. Deisseroth (2011). "Optogenetics in neural systems." *Neuron* **71**(1): 9-34.

135. Yizhar, O., L. E. Fenno, M. Prigge, F. Schneider, T. J. Davidson, D. J. O'Shea, V. S. Sohal, I. Goshen, J. Finkelstein, J. T. Paz, K. Stehfest, R. Fudim, C. Ramakrishnan, J. R. Huguenard, P. Hegemann and K. Deisseroth (2011). "Neocortical excitation/inhibition balance in information processing and social dysfunction." *Nature* **477**(7363): 171-178.

136. Zhang, F., M. Prigge, F. Beyriere, S. P. Tsunoda, J. Mattis, O. Yizhar, P. Hegemann and K. Deisseroth (2008). "Red-shifted optogenetic excitation: a tool for fast neural control derived from Volvox carteri." *Nat Neurosci* **11**(6): 631-633.

137. Zoccolan, D., M. Kouh, T. Poggio and J. J. DiCarlo (2007). "Trade-off between object selectivity and tolerance in monkey inferotemporal cortex." J *Neurosci* **27**(45): 12292-12307.